

# Spanwise wall forcing can reduce turbulent heat transfer more than drag

Amirreza Rouhi<sup>1</sup>†, Marcus Hultmark<sup>2</sup>, and Alexander J. Smits<sup>2</sup>

<sup>1</sup>Department of Engineering, School of Science and Technology  
Nottingham Trent University, Nottingham NG11 8NS, United Kingdom

<sup>2</sup>Department of Mechanical and Aerospace Engineering, Princeton University,  
Princeton, NJ 08544, USA

(Received xx; revised xx; accepted xx)

Direct numerical simulations are performed of turbulent forced convection in a half channel flow with wall oscillating either as a spanwise plane oscillation or to generate a streamwise travelling wave. The friction Reynolds number is fixed at  $Re_{\tau_0} = 590$ , but the Prandtl number  $Pr$  is varied from 0.71 to 20. For  $Pr > 1$ , the heat transfer is reduced by more than the drag, 40% compared to 30% at  $Pr = 7.5$ . This outcome is related to the different responses of the velocity and thermal fields to the Stokes layer. It is shown that the Stokes layer near the wall attenuates the large-scale energy of the turbulent heat-flux and the turbulent shear-stress, but amplifies their small-scale energy. At higher Prandtl numbers, the thinning of the conductive sublayer means that the energetic scales of the turbulent heat-flux move closer to the wall, where they are exposed to a stronger Stokes layer production, increasing the contribution of the small-scale energy amplification. A predictive model is derived for the Reynolds and Prandtl number dependence of the heat-transfer reduction based on the scaling of the thermal statistics. The model agrees well with the computations for Prandtl numbers up to 20.

**Key words:** turbulence simulation, turbulence control, turbulent convection, Reynolds analogy, Prandtl number

## 1. Introduction

In many industrial applications, controlling heat transfer is as important as controlling drag. Some examples of the kinds of methods to control both drag and heat transfer are given in figure 1. The performance of any given method is commonly based on the changes achieved in the skin-friction coefficient  $C_f$  and the Stanton number  $C_h$ , where

$$C_f \equiv \frac{2\overline{\tau_w}}{\rho U_{\text{ref}}^2}, \quad C_h \equiv \frac{\overline{q_w}}{\rho c_p U_{\text{ref}} (T_w - T_{\text{ref}})}. \quad (1.1)$$

Here  $\overline{\tau_w}$ ,  $\overline{q_w}$ ,  $\rho$ ,  $c_p$  and  $T_w$  are the wall shear-stress, wall heat-flux, fluid density, its specific heat capacity and wall temperature, respectively. The overbar in  $\overline{\tau_w}$  and  $\overline{q_w}$  represents averaging over the homogeneous directions and time. In a boundary layer,  $U_{\text{ref}}$  and  $T_{\text{ref}}$  are the free-stream velocity and temperature (Walsh & Weinstein 1979), and in a channel flow,  $U_{\text{ref}}$  and  $T_{\text{ref}}$  are the bulk velocity and either the bulk temperature (Stalio & Nobile

† Email address for correspondence: amirreza.rouhi@ntu.ac.uk

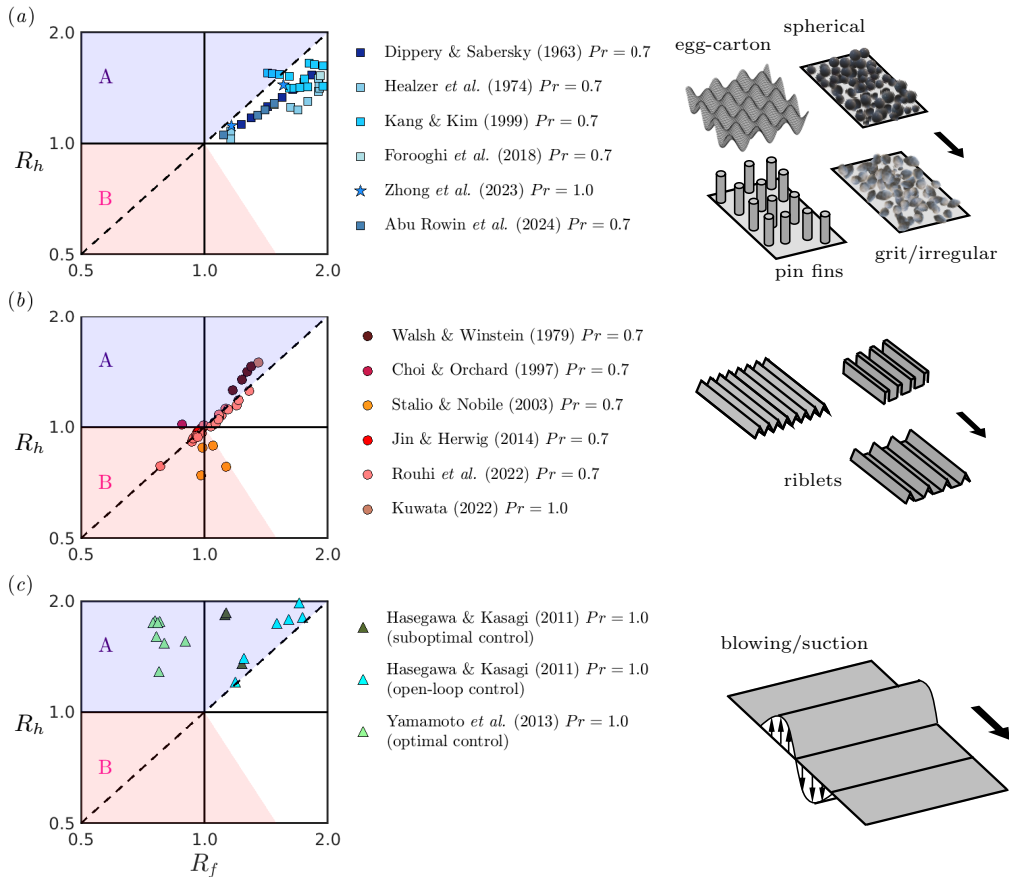


FIGURE 1. Performance plots showing the fractional changes in the skin-friction coefficient  $R_f = C_f/C_{f_0}$  and Stanton number  $R_h = C_h/C_{h_0}$  (log-log scale). The diagonal dashed line represents  $R_h = R_f$ . (a) Grit or irregular roughness (Dipprey & Sabersky 1963; Forooghi *et al.* 2018), spherical roughness (Healzer *et al.* 1974), pin fins (Kang & Kim 1999) and egg-carton roughness (Zhong *et al.* 2023; Rowin *et al.* 2024). (b) Riblets (Walsh & Weinstein 1979; Choi & Orchard 1997; Stalio & Nobile 2003; Jin & Herwig 2014; Rouhi *et al.* 2022; Kuwata 2022). (c) Wall blowing/suction (Hasegawa & Kasagi 2011; Yamamoto *et al.* 2013). All data points are at  $Pr = 0.7 - 1.0$ .

2003) or the mixed-mean temperature (Dipprey & Sabersky 1963; MacDonald *et al.* 2019; Rouhi *et al.* 2022).

Figure 1 also shows the type of performance plot that is often used to measure the efficacy of control methods (Fan *et al.* 2009; Bunker 2013; Huang *et al.* 2017; Rouhi *et al.* 2022). Here  $C_f$  and  $C_h$  are measured in the flow with control (the target case), and  $C_{f_0}$  and  $C_{h_0}$  are measured in the absence of control (the reference case), at matched Reynolds and Prandtl numbers. Some boundary layer studies match Reynolds numbers based on the free-stream velocity and the distance from the inlet (Walsh & Weinstein 1979; Choi & Orchard 1997). Some channel flow studies match Reynolds numbers based on the channel height and the bulk velocity (Stalio & Nobile 2003; Jin & Herwig 2014; Rouhi *et al.* 2022) or the friction velocity (MacDonald *et al.* 2019; Zhong *et al.* 2023). The diagonal dashed-line represents equal fractional change in drag  $R_f (= C_f/C_{f_0})$  and fractional change in heat transfer  $R_h (= C_h/C_{h_0})$ . In type A applications (shaded in

purple), the objective is to maximise the heat transfer between the fluid and the solid surface, while minimising the drag. Examples include air passages in the gas turbine blades (Baek *et al.* 2022; Otto *et al.* 2022) or solar air collectors (Vengadesan & Senthil 2020; Rani & Tripathy 2022). In both applications, the air needs to absorb heat from the surface (turbine blade or absorber tube of the collector), yet the friction loss needs to be minimised through the passages. In type B applications (shaded in pink), the objective is to simultaneously minimise the heat transfer and drag between the fluid and the solid surface. Examples include transportation of crude oil (Yu *et al.* 2010; Han *et al.* 2015; Yuan *et al.* 2023) or transportation of industrial waste heat (Hasegawa *et al.* 1998; Ma *et al.* 2009; Xie & Jiang 2017). In these applications, a heated fluid is transported through pipelines to a long-distance demand site, and requires heat loss and friction loss to be minimised.

From figure 1(a), we see that rough surfaces and pin fins augment the heat transfer ( $R_h > 1$ ), but for most data points the drag increase exceeds the heat-transfer increase ( $R_f > R_h > 1$ ), and so they fall outside the objective space for either type A or B applications. Several phenomena contribute to the imbalance between  $R_f$  and  $R_h$ . The flow recirculations behind the roughness elements trigger pressure drag in  $C_f$ , in addition to the viscous drag. However,  $C_h$  consists of the wall heat-flux only (MacDonald *et al.* 2019), which is the thermal analogue of the viscous stress. Additionally, the recirculation zones break the analogy between the viscous stress and the wall heat-flux (MacDonald *et al.* 2019), and the analogy between the turbulent shear-stress and the turbulent heat-flux (Kuwata 2021). Also, by increasing the roughness size, the conductive sublayer becomes thinner than the viscous sublayer (MacDonald *et al.* 2019; Zhong *et al.* 2023).

In figure 1(b), we show the performance of riblets, as two-dimensional streamwise-aligned surface protrusions which do not induce pressure drag. Most data points are scattered near  $R_h = R_f$ , but a few data points fall into the regions of interest for type A or B applications. Rouhi *et al.* (2022) and Kuwata (2022) relate such behaviour to the formation of Kelvin-Helmholtz rollers and secondary flows by certain riblet designs.

Figure 1(c) shows the data points for wall blowing/suction in a turbulent channel flow. All data points fall into the objective space for type A applications. The data points that noticeably yield  $R_h > R_f$  are from the application of a suboptimal control framework (Lee *et al.* 1998) or an optimal control framework (Bewley *et al.* 2001). Especially, the optimal control application results in simultaneous heat-transfer augmentation and drag reduction ( $R_h > 1 > R_f$ ). Hasegawa & Kasagi (2011) and Yamamoto *et al.* (2013) discovered that both the optimal and suboptimal control inputs exhibit characteristics similar to a travelling wave. When the coherent part of the suboptimal control inputs are applied as an open-loop control framework, the data points fall closer to  $R_h = R_f$ .

In the present study, we focus on wall oscillation either as a spanwise oscillating plane, or a streamwise travelling wave, as described by

$$W_s(x, t) = A \sin(\kappa_x x + \omega t) \quad (1.2)$$

where  $W_s$  is the instantaneous spanwise surface velocity that oscillates with amplitude  $A$  and frequency  $\omega$ . With  $\kappa_x \neq 0$ , the mechanism generates a streamwise travelling wave, and with  $\kappa_x = 0$  the motion is a simple spanwise oscillating plane (as illustrated in figure 2). We denote the former case as travelling wave, and the latter one as plane oscillation. The drag performance of (1.2) has been extensively investigated in the literature (Jung *et al.* 1992; Quadrio & Sibilla 2000; Quadrio *et al.* 2009; Viotti *et al.* 2009; Quadrio & Ricco 2011; Quadrio 2011; Gatti & Quadrio 2013; Hurst *et al.* 2014; Gatti & Quadrio 2016; Marusic *et al.* 2021; Rouhi *et al.* 2023; Chandran *et al.* 2023).

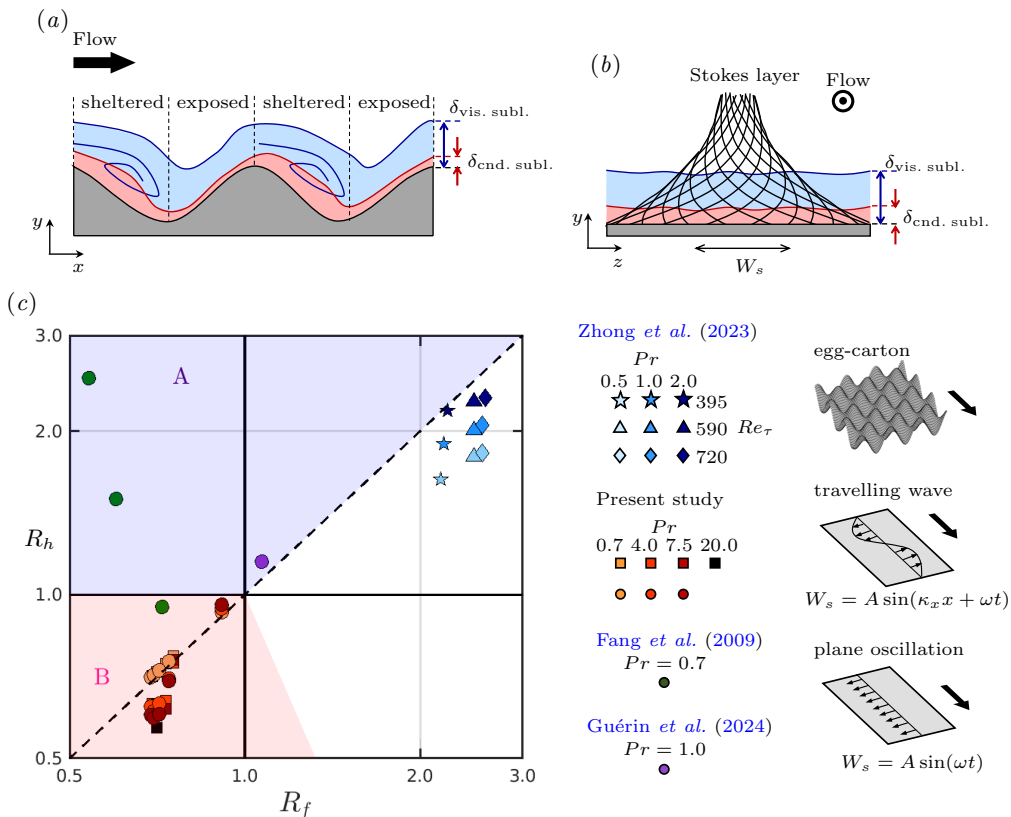


FIGURE 2. Effect of  $Pr$  on the performance of egg-carton roughness by [Zhong et al. \(2023\)](#), plane oscillation and travelling wave from the present study (table 1), and plane oscillation by [Fang et al. \(2009\)](#) and [Guérin et al. \(2024\)](#). Star, triangle and diamond symbols represent egg-carton roughness, square symbols represent streamwise travelling wave ( $\kappa_x \neq 0$  in 1.2), and circle symbols represent plane oscillation ( $\kappa_x = 0$  in 1.2). (a, b) Illustrate the different physics underlying the wall heat-transfer over roughness and wall oscillation for  $Pr > 1$ ;  $\delta_{\text{vis. subl.}}$  and  $\delta_{\text{end. subl.}}$  respectively indicate the viscous sublayer and conductive sublayer thicknesses. (c) compiles all the data points in the performance plot.

Dimensional analysis for the drag yields

$$R_f = C_f/C_{f_0} = f_f(A^+, \kappa_x^+, \omega^+, Re_{\tau_0}) \quad (1.3)$$

([Marusic et al. 2021](#); [Rouhi et al. 2023](#)). The superscript ‘+’ indicates normalisation using the viscous velocity ( $u_{\tau_0} = \sqrt{\tau_{w_0}/\rho}$ ) and length ( $\nu/u_{\tau_0}$ ) scales, where  $\nu$  is the fluid kinematic viscosity. The superscript ‘\*’ indicates viscous scaling based on the actual friction velocity, that is,  $u_\tau$  of the drag-altered flow for the actuated cases. For the heat transfer, we need to include the Prandtl number  $Pr = \nu/\alpha$ , where  $\alpha$  is the fluid thermal diffusivity, and we find

$$R_h = C_h/C_{h_0} = f_h(A^+, \kappa_x^+, \omega^+, Re_{\tau_0}, Pr). \quad (1.4)$$

The drag reduction is given by  $DR = 1 - R_f$ , and the heat-transfer reduction is given by  $HR = 1 - R_h$ . For  $HR$  we have a five-dimensional parameter space (1.4) that is investigated over a limited extent ([Fang et al. 2009, 2010](#); [Guérin et al. 2024](#)), as shown in figure 2. These studies consider spanwise plane oscillation ( $\kappa_x^+ = 0$ ) in a turbulent channel flow at  $Re_{\tau_0} = hu_{\tau_0}/\nu \simeq 180$  and  $Pr \simeq 0.7 - 1.0$ . [Fang et al. \(2009, 2010\)](#)

consider three cases with  $T_{osc}^+ = 2\pi/\omega^+ = 100$  and  $A^+ = 6, 13, 19$ , and Guérin *et al.* (2024) consider one case with  $T_{osc}^+ = 500$  and  $A^+ = 30$ . These cases fall into the objective space for type A applications (except one case with  $R_f < 1, R_h \simeq 1$ ).

Figure 2 highlights that we are at an early stage in terms of our knowledge of  $HR$  for the surface actuation (1.2), and just like the investigations on  $DR$ , we need to explore different parameters of (1.4) as a build up process. Comparing (1.4) with (1.3),  $Pr$  is a key parameter that differentiates  $R_h$  from  $R_f$ , and it leads to their significant disparity (figure 2). Furthermore, the fluids for type B applications have  $Pr \gg 1$  (e.g. crude oil). Therefore, in the present study we focus on  $Pr$  and  $\omega^+$  as our parameters of interest (figure 2 and table 1). We conduct DNSs of turbulent forced convection in a half channel flow with fix  $A^+ = 12$  and  $Re_{\tau_0} = 590$ , and we consider two values for  $\kappa_x^+$  to simulate plane oscillation ( $\kappa_x^+ = 0$ ) and travelling wave ( $\kappa_x^+ = 0.0014, \lambda^+ = 2\pi/\kappa_x^+ \simeq 4500$ ). We consider  $Pr = 0.71$  (air), 4.0, 7.5 (water) and 20 (molten salt). At each  $0.71 \leq Pr \leq 7.5$ , we systematically vary  $\omega^+$  from 0.022 to 0.110, corresponding to the regime where we expect  $DR$  to reach 30% (Gatti & Quadrio 2016; Rouhi *et al.* 2023). Our preference for the present actuation parameters is motivated by an existing surface-actuation test bed (Marusic *et al.* 2021; Chandran *et al.* 2023), that can operate under these conditions. This provides the opportunity to extend the present numerical study through experiment. As the first study that investigates  $Pr$  effects for this problem, we conduct a thorough study of grid resolution requirements for our considered parameter space (Appendix A).

As an overview, we note that all our results give a decrease in drag and heat transfer, with maximum  $DR = 30\%$  and  $HR = 40\%$  (see figure 2). For Prandtl numbers greater than one, however,  $HR$  increases more than  $DR$ . The results fall into the objective space for type B applications, a space that has largely been neglected in the past despite its industrial relevance. The surfaces that we reviewed in figure 1 consider  $Pr = 0.7-1.0$ , however, we anticipate that their performances will change with increasing  $Pr$ . For instance, in figure 2, we overlay the data points of egg-carton roughness at  $Pr = 0.5, 1.0, 2.0$  by Zhong *et al.* (2023). Unlike plane oscillation or travelling wave, the roughness data points approach  $R_h = R_f$  with increasing  $Pr$  because heat transfer over these two surface types is governed by different flow mechanisms that are unique to each surface, leading to different trends with  $Pr$ . Over the rough surface (figure 2a), variation of  $C_h$  with  $Pr$  depends on the area fraction of the sheltered and exposed regions, associated with the recirculation and attached zones that follow different local  $Pr$  scaling (Zhong *et al.* 2023; Rowin *et al.* 2024). Over the surface oscillation (figure 2b), the variation of  $C_h$  with  $Pr$  is an aspect that we investigate in the present study. We discover that by increasing  $Pr$  and thinning of the conductive sublayer, the Stokes layer, formed in response to the wall oscillation, transfers more energy to the near-wall temperature scales than the velocity scales. We also find that  $HR$  yields different  $Pr$  scaling depending on the actuation parameters. In §3.5, we derive a model that predicts that plane oscillation and travelling wave can reduce the heat loss beyond 50% for  $Pr \gtrsim \mathcal{O}(10^2)$ , a regime that is important for crude oil transportation through pipelines. Our model is supported by our DNS data point at  $Pr = 20$  that yields  $HR = 43\%$  (black square in figure 2).

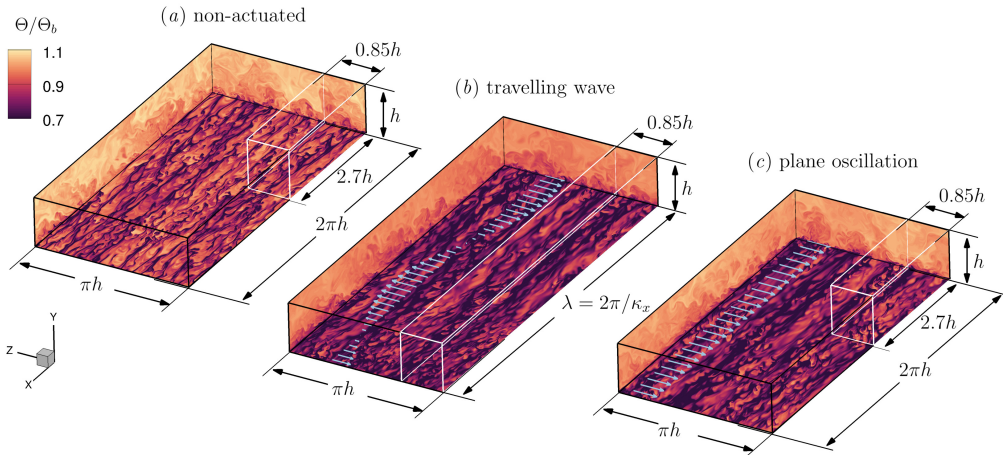


FIGURE 3. Computational configurations in a half channel flow for the present study. (a) Non-actuated case as the reference. (b) Actuated case with the travelling wave with  $A^+ = 12$ ,  $\kappa_x^+ = 0.0014$ ; the domain length encompasses one wavelength  $L_x = 2\pi/\kappa_x \simeq 7.6h$ . (c) Actuated case with spanwise plane oscillation with  $A^+ = 12$ . In (b,c), we overlay the instantaneous wall motion as a vector field. Full domain shown by the large box with black edges; reduced domain shown by the small box with white edges. In (a,b,c), we visualise the instantaneous fields of  $\Theta$  at  $y^+ = 15$ ,  $Re_{\tau_0} = 590$  and  $Pr = 7.5$ , and for  $\omega^+ = 0.088$  in (b,c).

## 2. Numerical flow setup

### 2.1. Governing equations and simulation setup

The governing equations for an incompressible fluid with constant  $\rho, \nu$  and thermal diffusivity  $\alpha$  are solved in a half channel flow (figure 3), where

$$\nabla \cdot \mathbf{U} = 0, \quad (2.1)$$

$$\frac{\partial \mathbf{U}}{\partial t} + \nabla \cdot (\mathbf{U}\mathbf{U}) = -\frac{1}{\rho} \nabla p + \nu \nabla^2 \mathbf{U} - \frac{1}{\rho} \frac{d\bar{P}}{dx} \hat{\mathbf{e}}_x, \quad (2.2)$$

$$\frac{\partial \Theta}{\partial t} + \nabla \cdot (\mathbf{U}\Theta) = \alpha \nabla^2 \Theta - U \frac{dT_w}{dx}, \quad (2.3)$$

and (2.1), (2.2) and (2.3) are the continuity, velocity and temperature transport equations, respectively. We ignore buoyancy, as appropriate for forced convection. In our notation,  $\mathbf{U} = (U, V, W)$  is the velocity vector, and  $x, y$  and  $z$  are the streamwise, wall-normal and spanwise directions, respectively. In (2.2), the total pressure gradient was decomposed into the driving (mean) part  $d\bar{P}/dx$  and the periodic part  $\nabla p$ . Similarly, the total temperature  $T = (dT_w/dx)x + \Theta$  was decomposed into the mean part  $dT_w/dx$  and the periodic part  $\Theta$ . This thermal driving approach imposes a prescribed mean heat flux at the wall, making it a suitable boundary condition for a periodic domain, and it has been widely used for the simulation of forced convection in a channel flow (Kasagi *et al.* 1992; Watanabe & Takahashi 2002; Stalio & Nobile 2003; Jin & Herwig 2014; Alcántara-Ávila & Hoyas 2021; Alcántara-Ávila *et al.* 2021; Rouhi *et al.* 2022). By averaging (2.2) and (2.3) in time and over the entire fluid domain, we obtain

$$-\frac{1}{\rho} \frac{d\bar{P}}{dx} h = \frac{\bar{\tau}_w}{\rho} \equiv u_\tau^2, \quad -U_b \frac{dT_w}{dx} h = \frac{\bar{q}_w}{\rho c_p} \equiv \theta_\tau u_\tau \quad (2.4a,b)$$

where  $\overline{\tau_w}$  and  $\overline{q_w}$  are respectively the  $xz$ -plane and time averaged wall shear-stress and wall heat-flux,  $U_b$  is the bulk velocity,  $h$  is the half channel height,  $u_\tau$  and  $\theta_\tau$  are the friction velocity and friction temperature, and  $c_p$  is the specific heat capacity. We adjust  $d\overline{P}/dx$  based on a target flow rate (namely, a bulk Reynolds number  $Re_b \equiv U_b h/\nu$ ) that is matched between the non-actuated reference case (figure 3a) and the actuated cases (figure 3b,c).

Equations (2.1-2.3) are solved using a fully conservative fourth-order finite difference code, employed by previous DNS studies of thermal convection (Ng *et al.* 2015; Rouhi *et al.* 2021; Zhong *et al.* 2023; Rowin *et al.* 2024). The half channel flow has periodic boundary conditions in the streamwise and spanwise directions (figure 3). The bottom-wall velocity boundary conditions are  $U = V = W = 0$  for the non-actuated case (figure 3a),  $U = V = 0$ ,  $W = A \sin(\kappa_x x + \omega t)$  for the actuated case with the travelling wave (figure 3b), and  $U = V = 0$ ,  $W = A \sin(\omega t)$  for the actuated case with the spanwise plane oscillation (figure 3c). The top boundary conditions for the velocity are the free-slip and impermeable conditions ( $\partial U/\partial y = \partial W/\partial y = V = 0$ ). The boundary conditions for  $\Theta$  at the bottom wall and top boundary are  $\Theta = 0$  and  $\partial \Theta/\partial y = 0$ , respectively. In other words, the total temperature at the bottom wall increases linearly in the  $x$ -direction  $T = (dT_w/dx)x$ , and at the top boundary the boundary condition is adiabatic ( $\partial T/\partial y = 0$ ). Past studies have employed half channel flow to study turbulent flow over complex surfaces (Yuan & Piomelli 2014; MacDonald *et al.* 2017; Rouhi *et al.* 2019). This configuration has a lower computational cost compared to the conventional poiseuille channel flow with no-slip condition at the bottom and top walls. Yet the two configurations have almost identical mean velocity profiles up to the logarithmic region, and similar turbulent stresses (Yao *et al.* 2022). This is also supported in Appendix A, where we obtain very similar mean velocity and turbulent stress profiles between our non-actuated half channel flow and the DNS of poiseuille channel flow by Moser *et al.* (1999) (figure 25a,b), and the values of  $C_{f_0}$  differ by less than 2% (table 2).

Throughout this manuscript, we call  $\Theta$  the temperature. We denote the  $xz$ -plane and time averaged quantities with overbars (e.g.  $\overline{\Theta}$  is the plane and time averaged  $\Theta$ ), the turbulent quantities with lowercase letters (e.g.  $\theta$  is the turbulent temperature). Following this notation,  $\overline{u^2}$  and  $\overline{uv}$  are the turbulent stress components, and  $\overline{\theta^2}$  and  $\overline{\theta v}$  are their analogue for the turbulent temperature fluxes.

## 2.2. Simulation cases

Table 1 summarises the production calculations. All the calculations were performed at a fixed bulk Reynolds number  $Re_b \simeq 11004$ , equivalent to a friction Reynolds number  $Re_{\tau_0} = 590$  for the non-actuated flow. The grid sizes are  $\Delta_x^+ \times \Delta_z^+ \simeq 8 \times 4$ ,  $\Delta_y^+ = 0.28 - 8.5$ , chosen based on extensive validation studies (Appendix A). In comparison, Alcántara-Ávila & Hoyas (2021) used  $\Delta_x^+ \times \Delta_z^+ \simeq 8 \times 4$ ,  $\Delta_y^+ = 0.27 - 5.3$  for turbulent channel flow at  $Re_{\tau_0} = 500$  and  $1 \leq Pr \leq 7$ , and Pirozzoli (2023) used  $\Delta_x^+ \times \Delta_z^+ \simeq 10 \times 4.5$  with 30 points within  $y^+ \leq 40$  for turbulent pipe flow at  $Re_{\tau_0} \simeq 1100$  and  $Pr \leq 16$ . Here, we have 60 points within  $y^+ \leq 40$ . As shown in Appendix A, we obtain less than 2% difference in  $DR$  and  $HR$  when using finer resolutions than our production calculation grids (tables 2 to 4), and find very good agreement in the first and second order velocity and temperature statistics as well as their spectrograms (figures 25 to 27).

To reduce the computational cost, the production calculations were performed in a reduced domain rather than a full-domain conventional channel flow (see figure 3). Because of the domain truncation, the flow is fully resolved up to a fraction of the domain height  $y_{\text{res}} < h$  (figure 4). In the past, the reduced-domain channel flow has been used for accurate calculation of the drag and the near-wall turbulence over various static and

non-actuated		travelling wave $A^+ = 12, \kappa_x^+ = 0.0014$			oscillating plane $A^+ = 12$			
$L_x, L_z = 2.7h, 0.85h$ $\Delta_x^+, \Delta_z^+ = 8.3, 3.9$ $\Delta_y^+ = 0.28 - 8.5$		$L_x, L_z = 7.6h, 0.85h$ $\Delta_x^+, \Delta_z^+ = 8.8, 3.9$ $\Delta_y^+ = 0.28 - 8.5$			$L_x, L_z = 2.7h, 0.85h$ $\Delta_x^+, \Delta_z^+ = 8.3, 3.9$ $\Delta_y^+ = 0.28 - 8.5$			
$C_{f_0} \times 10^{-3}$	$C_{h_0} \times 10^{-4}$	$\omega^+$	$DR\%$	$HR\%$	$\omega^+$	$DR\%$	$HR\%$	
5.71	33.82	0.022	25.2	23.6	0.022	8.6	7.3	$Pr = 0.71$
		0.044	30.6	29.3	0.044	25.9	24.7	
		0.066	30.5	29.1	0.066	31.1	29.6	
		0.088	29.3	27.9	0.088	30.3	28.9	
		0.110	26.8	25.3	0.110	28.7	27.4	
5.71	14.14	0.022	24.5	25.3	0.022	9.5	5.9	$Pr = 4.0$
		0.044	31.0	37.0	0.044	25.9	30.1	
		0.066	30.7	38.4	0.066	30.4	37.8	
		0.088	29.1	37.3	0.088	30.6	39.0	
		0.110	27.6	36.2	0.110	28.2	36.9	
5.72	9.90	0.022	25.6	24.0	0.022	9.7	4.3	$Pr = 7.5$
		0.044	31.8	37.7	0.044	26.5	30.8	
		0.066	30.7	39.8	0.066	31.3	40.0	
		0.088	30.5	40.4	0.088	30.2	40.7	
		0.110	27.5	38.0	0.110	28.7	39.8	
5.71	5.47	0.088	29.5	43.5			$Pr = 20.0$	

TABLE 1. Production calculations at  $Re_{\tau_0} = 590$  (reduced domain  $L_x \geq 2.7h, L_z = 0.85h$ ). Non-actuated cases (left column, figure 3a). Travelling wave cases (middle column, figure 3b). Spanwise plane oscillation cases (right column, figure 3c). Each row represents one simulation case. The domain and grid sizes for each configuration are reported at the top.

deforming surfaces, including egg-carton roughness with  $y_{\text{res}}^+ \lesssim 250$  (MacDonald *et al.* 2017, 2018), riblets with  $y_{\text{res}}^+ \simeq 100$  (Endrikat *et al.* 2021), and travelling waves with  $y_{\text{res}}^+ \lesssim 1000$  (Gatti & Quadrio 2016; Rouhi *et al.* 2023). The reduced-domain channel flow has also been employed for accurate calculation of the wall heat-flux and the near-wall thermal field over rough surfaces with  $y_{\text{res}}^+ \lesssim 600$  (MacDonald *et al.* 2019; Zhong *et al.* 2023; Rowin *et al.* 2024), and riblets with  $y_{\text{res}}^+ \simeq 100$  (Rouhi *et al.* 2022). In our case, as shown in Appendix A, with  $\Delta_x^+ \times \Delta_z^+ \simeq 8 \times 4$  the difference between the reduced and the full domains is less than 1% in terms of  $DR$  and  $HR$  (full coarse and reduced coarse cases in table 3). Furthermore, the results for the two domain sizes agree well in terms of the statistics of velocity and temperature, and their spectrograms (figures 26 and 27). For the reduced domain sizes, we follow the prescriptions by Chung *et al.* (2015) and MacDonald *et al.* (2017), that were extended to the travelling wave actuation case by Rouhi *et al.* (2023). The resolved height  $y_{\text{res}}^+$  needs to fall in the logarithmic region, and the domain width  $L_z^+$  and length  $L_x^+$  are adjusted so that  $L_z^+ \simeq 2.5y_{\text{res}}^+$  and  $L_x^+ \gtrsim \max(3L_z^+, 1000, \lambda^+)$ , where  $\lambda = 2\pi/\kappa_x$  is the travelling wavelength. Here, we chose  $y_{\text{res}}^+ = 200$ , which resolves up to a third of the half channel height. Hence the domain sizes are  $L_x \times L_z \simeq 2.7h \times 0.85h$  for the non-actuated and the plane oscillation cases (figure 3a,c). For the travelling wave cases, however,  $L_x$  cannot be truncated because it is constrained by the travelling wavelength  $\lambda \simeq 7.6h$ , and so we use  $L_x \times L_z \simeq 7.6h \times 0.85h$



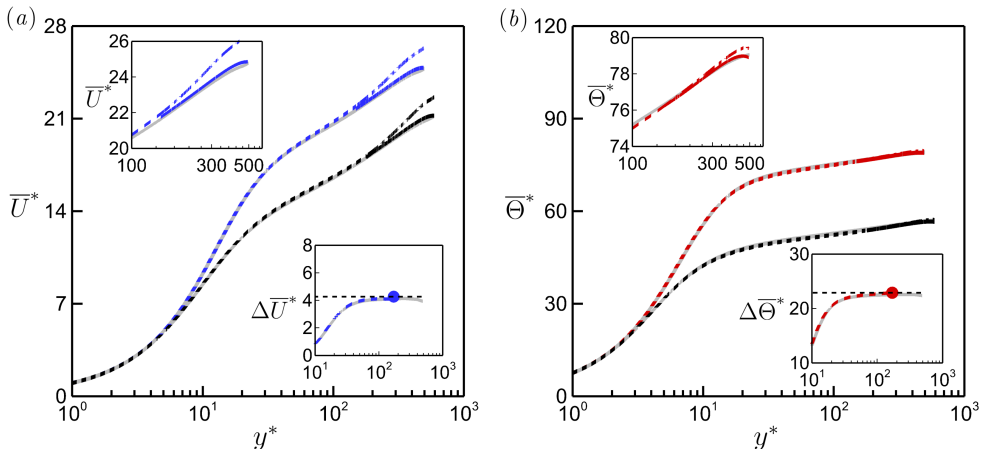


FIGURE 4. Comparison at  $Re_{\tau_0} = 590$  of (a) mean velocity  $\bar{U}^*$ , and (b) mean temperature  $\bar{\Theta}^*$  between the full-domain (grey lines) and the reduced-domain half channel flow (black, blue and red lines). Black lines: non-actuated case at  $Pr = 7.5$ . Blue and red lines: travelling wave case at  $Pr = 7.5$  with  $A^+ = 12$ ,  $\kappa_x^+ = 0.0014$ ,  $\omega^+ = 0.088$ . For the reduced-domain cases, the resolved portion is shown with a dashed line ( $y^* \lesssim 170$ ), and the unresolved portion is shown with a dashed-dotted line ( $y^* \gtrsim 170$ ). The unresolved portion is replaced by the reconstructed profiles (solid lines), as explained in §2.3. The insets plot the velocity and temperature differences  $\Delta \bar{U}^*$  and  $\Delta \bar{\Theta}^*$ ; bullets mark  $y_{\text{res}}^* = 170$ , where we obtain the log-law shifts  $\Delta \bar{U}_{\text{log}}^*$  and  $\Delta \bar{\Theta}_{\text{log}}^*$ .

(figure 3b). For the actuated cases,  $y_{\text{res}}$  scaled by the actuated (drag-reduced) friction velocity is  $170 \lesssim y_{\text{res}}^* \lesssim 190$  (that is, less than 200). Therefore,  $y_{\text{res}}^* = 170$  is taken to be the maximum resolved height for all our cases.

### 2.3. Calculating the skin-friction coefficient and Stanton number

We can write the skin-friction coefficient and Stanton number as  $C_f = 2/U_b^{*2}$  and  $C_h = 1/(U_b^* \Theta_b^*)$ . Although some studies use the mixed-mean temperature to define  $C_h$  (MacDonald *et al.* 2019; Rouhi *et al.* 2022; Zhong *et al.* 2023), we use the bulk temperature  $\Theta_b$  as adopted by Stalio & Nobile (2003) and Kuwata (2022), primarily because it is more straightforward to derive a predictive model for  $HR$  with this definition (Appendix B). For our cases, there is only a maximum 2% difference between  $C_h$  based on  $\Theta_b$  and the one based on the mixed-mean temperature.

For the full-domain half channel flow, the mean velocity  $\bar{U}^*$  and temperature  $\bar{\Theta}^*$  are fully resolved across the entire domain (grey profiles in figure 4), and so  $U_b^*$  and  $\Theta_b^*$  can be obtained by direct integration of  $\bar{U}^*$  and  $\bar{\Theta}^*$ . For the reduced-domain half channel flow, we first need to construct  $\bar{U}^*$  and  $\bar{\Theta}^*$  beyond  $y_{\text{res}}^*$  (Rouhi *et al.* 2022, 2023). In figure 4, we see that the resolved portions of the  $\bar{U}^*$  and  $\bar{\Theta}^*$  profiles up to  $y_{\text{res}}^* \simeq 170$  are in excellent agreement with the full-domain profiles. Beyond  $y_{\text{res}}^*$ , however, the flow is unresolved due to the domain truncation, appearing as a fictitious wake in the  $\bar{U}^*$  and  $\bar{\Theta}^*$  profiles (dashed-dotted lines in figure 4). The fictitious wake is weaker for the  $\bar{\Theta}^*$  profile at  $Pr = 7.5$  than the  $\bar{U}^*$  profile, which could also be regarded as a  $\bar{\Theta}^*$  profile at  $Pr = 1.0$ . In other words, the domain truncation affects  $\bar{\Theta}^*$  to a lesser degree by increasing  $Pr$ . Nevertheless, even for the  $\bar{U}^*$  profile, the fictitious wake is constrained to  $y^* \gtrsim 170$ . We replace these unresolved portions with the composite profiles of  $\bar{U}^*$  and  $\bar{\Theta}^*$  (C1a, C1b in Appendix B). For this, we need the log-law shifts  $\Delta \bar{U}_{\text{log}}^*$  and  $\Delta \bar{\Theta}_{\text{log}}^*$  in (C1a) and (C1b), which we obtain by plotting  $\Delta \bar{U}^* = \bar{U}^* - \bar{U}_0^*$  and  $\Delta \bar{\Theta}^* = \bar{\Theta}^* - \bar{\Theta}_0^*$ ,

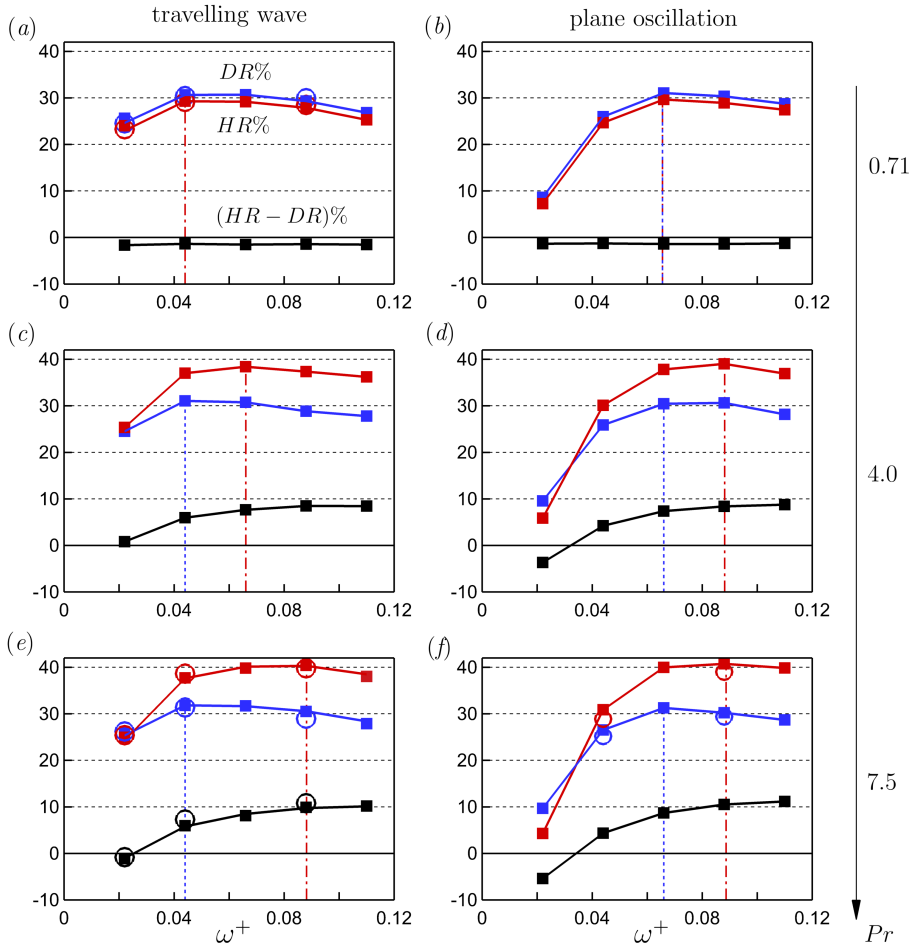


FIGURE 5. Values of  $DR\%$  (blue symbols),  $HR\%$  (red symbols) and their difference (black symbols) for the cases given in table 1. Filled squares: reduced domain simulations; empty circles: full domain simulations. Blue dashed line marks the maximum  $DR$ ; red dashed-dotted line marks the maximum  $HR$ .

the differences between the actuated and the non-actuated cases (see figure 4). Finally, we find  $U_b^*$  and  $\Theta_b^*$  by integrating the resolved portion of the profiles up to  $y_{res}^*$  and the reconstructed portion beyond  $y_{res}^*$ . By applying this profile reconstruction, we obtain less than 1% difference in  $C_f$  and  $C_h$  between the full-domain case and the reduced domain case (table 3 in Appendix A).

### 3. Results

#### 3.1. Overall variations of $DR$ and $HR$

The values of  $HR$ ,  $DR$  and the difference  $HR - DR$  are shown in figure 5. For all cases considered,  $HR$  and  $DR$  initially increase with the frequency of forcing, but for  $\omega^+ \gtrsim 0.04$  they reach a maximum value before slowly decreasing at higher frequencies. The maximum drag reduction is about 30% for all Prandtl numbers, but the maximum heat-transfer reduction increases from 30% to about 40% with increasing Prandtl number,

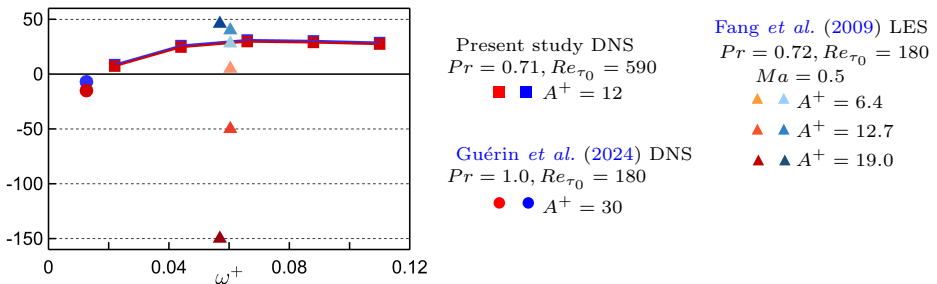


FIGURE 6. Plane oscillation data of  $DR\%$  (blue symbols) and  $HR\%$  (orange/red symbols) at  $Pr = 0.7 - 1.0$  from our present study, Guérin *et al.* (2024), and Fang *et al.* (2009).

marking a significant disparity between  $DR$  and  $HR$ . The increasing disparity towards  $HR > DR$  occurs for  $\omega^+ \geq 0.04$ , however, at  $\omega^+ = 0.022$ ,  $HR \lesssim DR$ . The comparison between the reduced-domain results (filled squares) and the full-domain results (open circles) supports the reliability of the production runs. At  $Pr = 7.5$ , the reduced domain grid is more than twice as coarse as the full domain grid, yet there is less than 2% difference in  $DR$  and  $HR$  (Appendix A gives more details). The trends in  $DR$  seen here have been widely recorded in the previous literature, as the review by Ricco *et al.* (2021) makes clear. However, to the authors' knowledge, the behaviour of  $HR$  has not been reported before. In §3.4, we relate the observed trends between  $HR$  and  $DR$  to the attenuation in the turbulent shear-stress  $\overline{uv}$  and turbulent scalar-flux  $\overline{\theta v}$ , followed by studying their interactions with the Stokes layer (§3.6-3.8).

In figure 6, we plot the plane oscillation data of  $DR$  and  $HR$  at close  $Pr = 0.71 - 1.0$  from our present study (figure 5b), Guérin *et al.* (2024), and Fang *et al.* (2009). Unlike our data, the two cited studies obtain heat-transfer increase ( $HR \lesssim 0$ ). Compared to Guérin *et al.* (2024), our  $A^+$  values differ by 2.5 times, and  $\omega^+$  values differ by 1.7 times. Nevertheless, based on our findings from §3.6-3.8, we speculate that  $HR < DR < 0$  by Guérin *et al.* (2024) is related to the highly protrusive Stokes layer (beyond 50 viscous units) for  $\omega^+ < 0.04$  (figure 22). Compared to Fang *et al.* (2009), we have close values of  $A^+$  and  $\omega^+$ . At  $A^+ \simeq 12.0$  and  $\omega^+ \simeq 0.06$ , the  $DR$  values differ by 9% between Fang *et al.* (2009) ( $DR = 40\%$ ,  $Re_{\tau_0} = 180$ ) and our study ( $DR = 31\%$  at  $Re_{\tau_0} = 590$ ); this is due to the Reynolds number difference, as discussed in the literature (Gatti & Quadrio 2016; Marusic *et al.* 2021; Rouhi *et al.* 2023). However, the values of  $HR$  have opposite signs and are different by 80%,  $HR = 30\%$  from our study versus  $HR = -50\%$  from Fang *et al.* (2009). In addition to  $Re_{\tau_0}$ , we speculate that such difference is related to the different computational setups. We conduct DNS of incompressible turbulent channel flow with  $\Delta_x^+ \times \Delta_z^+ = 8.3 \times 3.9$ , while Fang *et al.* (2009) conduct large-eddy simulation (LES) of compressible turbulent channel flow (Mach number  $Ma = 0.5$ ) with  $\Delta_x^+ \times \Delta_z^+ = 35 \times 12$ .

### 3.2. Optimal actuation frequency

Figure 5 indicates that the optimal actuation frequency for  $DR$  is  $\omega^+ \approx 0.044$  for the travelling wave, and  $\approx 0.066$  for the plane oscillation, regardless of the Prandtl number. For  $HR$ , the optimal frequency coincides with that for  $DR$  at  $Pr = 0.71$ , but it increases to 0.088 for both types of actuation as the Prandtl number increases to 7.5.

Previous studies relate the optimal frequency for drag reduction to the characteristic time-scale of the energetic velocity scales associated with the near-wall cycle of turbulence,  $\mathcal{T}_u^+$  (Quadrio *et al.* 2009; Chandran *et al.* 2023). When the actuation period

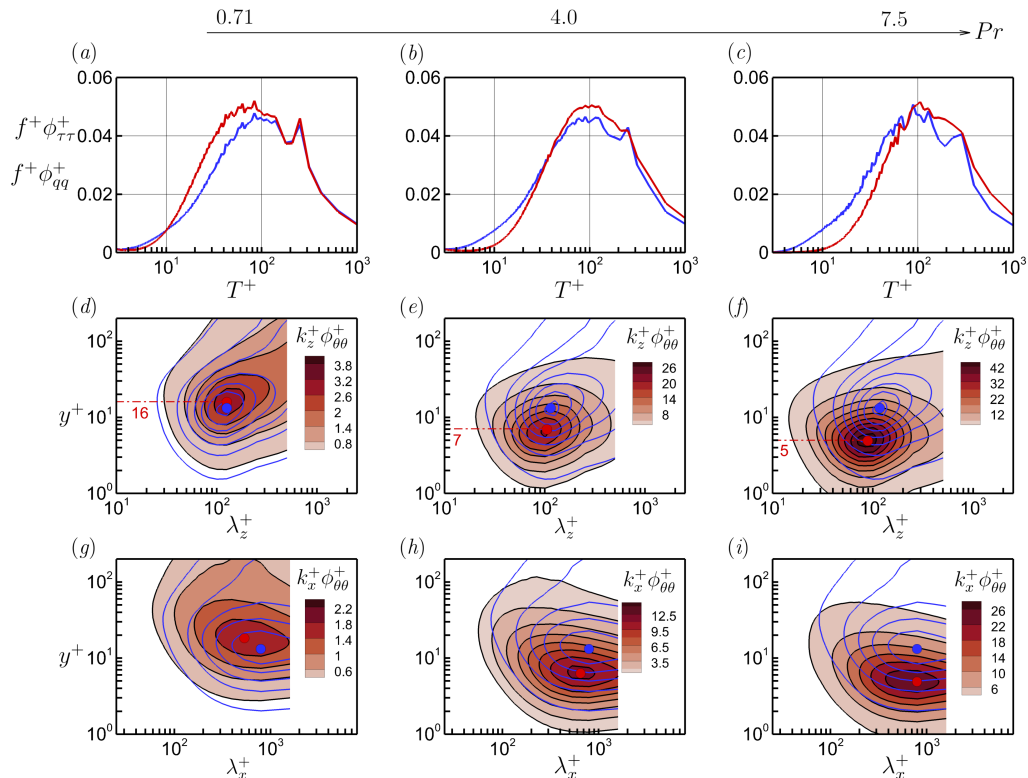


FIGURE 7. Non-actuated half channel flow with increasing Prandtl number. (a,d,g)  $Pr = 0.71$ ; (b,e,h)  $Pr = 4.0$ ; (c,f,i)  $Pr = 7.5$ . (a-c) Pre-multiplied frequency spectra of wall shear-stress  $f^+ \phi_{\tau\tau}^+$  (blue line) and wall heat-flux  $f^+ \phi_{qq}^+$  (red line), where  $T^+ = 1/f^+$ . (d-f) Spectrograms of the streamwise velocity fluctuations (blue contour lines) and temperature fluctuations (filled contour) pre-multiplied by the spanwise wavenumber  $k_z^+$ . (g-i) Same as (d-f), pre-multiplied by the streamwise wavenumber  $k_x^+$ . Contour levels for  $k_z^+ \phi_{uu}^+$  start from 0.2 to 3.8 with an increment of 0.6; contour levels for  $k_x^+ \phi_{uu}^+$  start from 0.2 to 2.2 with an increment of 0.4. The blue and red bullets in (d-f) locate the maximum in  $k_z^+ \phi_{uu}^+$  and  $k_z^+ \phi_{\theta\theta}^+$ , respectively, and in (g-i) locate the maximum in  $k_x^+ \phi_{uu}^+$  and  $k_x^+ \phi_{\theta\theta}^+$ , respectively.

$T_{osc}^+ \equiv 2\pi/\omega^+$  matches this time scale, the wall oscillation becomes more effective in disrupting the near-wall scales, leading to the maximum  $DR$  (Ricco *et al.* 2021). Chandran *et al.* (2023) discuss this interaction using the pre-multiplied spectrum of wall shear-stress  $f^+ \phi_{\tau\tau}^+$ , and the corresponding spectra for our non-actuated case are shown in figure 7(a-c) (blue lines). In agreement with Chandran *et al.* (2023), the peaks in the shear-stress spectra occur at  $\mathcal{T}_u^+ \simeq 100$ , corresponding to  $\omega^+ \simeq 0.063$ , which broadly matches the frequencies of actuation for maximum drag reduction found here.

Figure 7 also shows the corresponding spectra for the fluctuating wall heat-flux,  $f^+ \phi_{qq}^+$  (red lines), as well as the pre-multiplied spectrograms of the fluctuating streamwise velocity and temperature ( $k_z^+ \phi_{uu}^+$ ,  $k_x^+ \phi_{uu}^+$ ,  $k_z^+ \phi_{\theta\theta}^+$ ,  $k_x^+ \phi_{\theta\theta}^+$ ). Figures 7(a,b,c) reveal that while  $f^+ \phi_{qq}^+$  is sensitive to  $Pr$  at small time-scales ( $T^+ \lesssim 70$ ), the time scale of the energetic temperature scales  $\mathcal{T}_\theta^+ \simeq 100$  is insensitive to  $Pr$ , and coincides with  $\mathcal{T}_u^+$ . The streamwise and spanwise lengths of the energetic temperature scales vary somewhat with Prandtl number (see figures 7d-i), but they also remain close to the length-scales

of the energetic velocity scales. However, the peak in  $k_z^+ \phi_{\theta\theta}^+$  drops from  $y^+ = 16$  at  $Pr = 0.71$  to  $y^+ = 5$  at  $Pr = 7.5$ , as the conductive sublayer thins with increasing Prandtl number (Alcántara-Ávila & Hoyas 2021; Kader 1981; Schwertfirm & Manhart 2007). The  $y^+$  location of the peak in  $k_z^+ \phi_{\theta\theta}^+$  scales with  $\sim Pr^{-1/2}$ , which is steeper than the scaling of  $\sim Pr^{-1/3}$  for the conductive sublayer thickness for  $Pr \gtrsim 1$  (Shaw & Hanratty 1977; Kader 1981; Schwertfirm & Manhart 2007; Alcántara-Ávila & Hoyas 2021; Pirozzoli 2023). We also analysed the  $\overline{\theta^2}^+$  profiles of Pirozzoli (2023) for the DNS of turbulent pipe flow at  $Re_{\tau_0} \simeq 1100$  and  $Pr = 0.5, 1, 2, 4, 16$ , and the  $y^+$  locations of their inner peaks scale with  $\sim Pr^{-1/2}$ .

For the plane oscillation, we expect that the maximum  $DR$  and  $HR$  is achieved when the actuation period is close to  $\mathcal{T}_u^+$  and  $\mathcal{T}_\theta^+$ , respectively. For the travelling wave, however, the optimal actuation period cannot be directly compared with  $\mathcal{T}_u^+$  or  $\mathcal{T}_\theta^+$ , owing to the relative streamwise motion between the travelling wave and the advecting near-wall scales. As discussed by Quadrio *et al.* (2009), for maximum  $DR$ ,  $\mathcal{T}_u^+$  must be compared with a relative oscillation period  $2\pi/(\kappa_x^+ \mathcal{U}_u^+ + \omega^+)$  as seen by an observer travelling with the convection speed of the near-wall energetic velocity scales  $\mathcal{U}_u^+$ . Similarly, for maximum  $HR$ ,  $\mathcal{T}_\theta^+$  must be compared with  $2\pi/(\kappa_x^+ \mathcal{U}_\theta^+ + \omega^+)$ , where  $\mathcal{U}_\theta^+$  is the convection speed of the near-wall energetic temperature scales. After some recasting (using  $\mathcal{T}_u^+ \simeq \mathcal{T}_\theta^+ \simeq 100$ ,  $\kappa_x^+ = 0.0014$ ), we estimate the optimum frequencies of actuation for  $DR$  and  $HR$  to be, respectively,

$$\omega_{\text{opt},DR}^+ = \frac{2\pi}{\mathcal{T}_u^+} - \kappa_x^+ \mathcal{U}_u^+ \simeq 0.046, \quad (3.1a)$$

$$\omega_{\text{opt},HR}^+ = \frac{2\pi}{\mathcal{T}_\theta^+} - \kappa_x^+ \mathcal{U}_\theta^+ \simeq 0.063 - 0.0014\mathcal{U}_\theta^+, \quad (3.1b)$$

where we have assumed that  $\mathcal{U}_u^+$  follows a universal curve (Kim & Hussain 1993; Del Álamo & Jiménez 2009; Liu & Gayme 2020), where  $\mathcal{U}_u^+ \simeq 12$  at  $y^+ \simeq 15$  (marked with blue bullets in figures 7*d–i*).

The estimated optimum frequency for  $DR$  is independent of Prandtl number, at about 0.046, consistent with our DNS results for the travelling wave case (figures 5*a,c,e*). However, the optimum frequency for  $HR$  depends on  $Pr$ , since we expect that  $\mathcal{U}_\theta^+$  decreases as the energetic temperature scales move closer to the wall with increasing Prandtl number (red bullets in figure 7*d–i*). Hetsroni *et al.* (2004) computed the profiles of  $\mathcal{U}_\theta^+$  at  $Pr = 1.0, 5.4$  and  $54$  in a configuration similar to that used in the present study, without actuation. Using their results, we estimate that  $\mathcal{U}_\theta^+$  decreases from 12 to 6 as  $Pr$  increases from 0.71 to 7.5, which gives  $\omega_{\text{opt},HR}^+ = 0.046$  at  $Pr = 0.71$  and 0.055 at  $Pr = 7.5$ . The estimated value at  $Pr = 7.5$  is smaller than the value of 0.088 given by the DNS (figure 5*e*), but the trends with Prandtl number are consistent. In §3.6 and 3.7, we conduct a more quantitative justification for the trends in  $\omega_{\text{opt},HR}^+$  by considering the interaction between the Stokes layer and the near-wall thermal field.

### 3.3. Mean profiles and turbulence statistics

We now consider the distributions of the mean velocity  $\overline{U}^*$  ( $= \overline{U}/u_\tau$ ), the mean temperature  $\overline{\Theta}^*$  ( $= \overline{\Theta}/\theta_\tau$ ) (figure 8), and the velocity and temperature statistics (figure 9) as we vary  $\omega^+$  and  $Pr$ . We focus on the travelling wave case, but since the observed trends are consistent with those from the plane oscillation case (figures 28 and 29 in Appendix C), our conclusions are applicable to both types of actuation.

It is well known from the literature that drag reduction by either plane oscillation or travelling wave coincides with the thickening of the viscous sublayer (Choi *et al.*

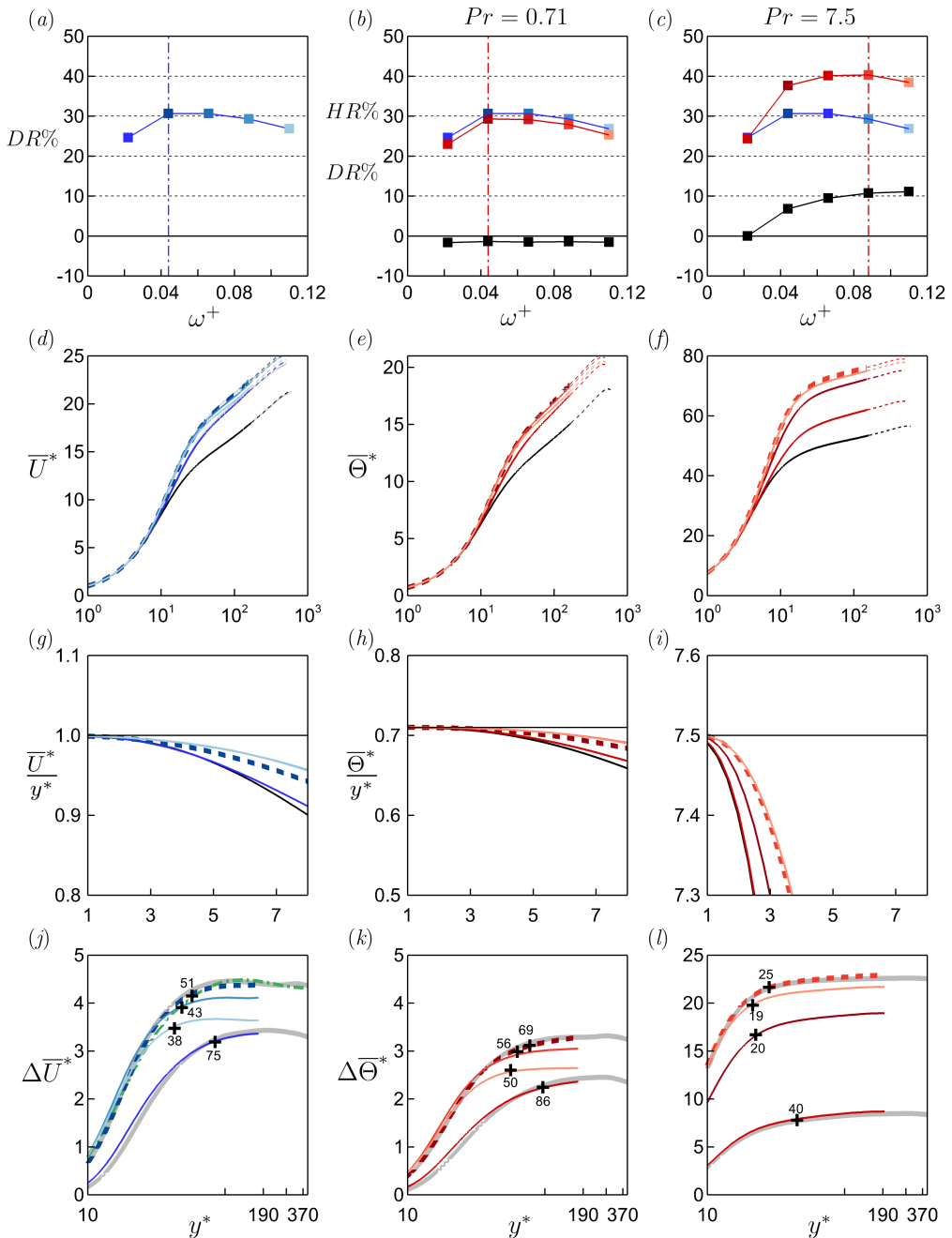


FIGURE 8. Travelling wave actuation with  $A^+ = 12$ ,  $\kappa_x^+ = 0.0014$ . Left column:  $DR\%$  and  $\bar{U}^*$  profiles, where  $\Delta \bar{U}^* = \bar{U}^* - \bar{U}_0^*$  (results independent of  $Pr$ ). Middle and right columns correspond to  $Pr = 0.71$  and  $7.5$ , respectively:  $DR\%$  (blue line),  $HR\%$  (red line), and  $\bar{\Theta}^*$  profiles, where  $\Delta \bar{\Theta}^* = \bar{\Theta}^* - \bar{\Theta}_0^*$ . In the panels (d-i), the black line is the reference (non-actuated) case, the blue lines and the red lines show the effects of increasing  $\omega^+$  on  $\bar{U}^*$  and  $\bar{\Theta}^*$ , respectively, and the thick dashed line corresponds to  $DR_{\max}$  or  $HR_{\max}$ . In (d,e,f), the thin dotted lines for  $y^* \gtrsim 170$  are the reconstructed profiles following § 2.3. In (j,k,l), we plot the reduced-domain profiles (red/blue) up to  $y_{\text{res}}^* \approx 170$ , and the thick grey profiles are from the full-domain cases ( $L_x \times L_z = 7.6h \times \pi h$ ) from Appendix A; the dashed-dotted green profile in (j) is at matched  $A^+ = 12$ ,  $\kappa_x^+ = 0.0014$ ,  $\omega^+ = 0.044$  but at  $Re_{\tau_0} = 950$  from Rouhi *et al.* (2023). The black cross symbols mark the distance  $y^*$  where  $\Delta \bar{U}^* = 0.9 \Delta \bar{U}^*_{170}$  ( $\Delta \bar{\Theta}^* = 0.9 \Delta \bar{\Theta}^*_{170}$ ).

1998; Choi & Clayton 2001; Choi 2002; Di Cicca *et al.* 2002; Touber & Leschziner 2012; Hurst *et al.* 2014; Gatti & Quadrio 2016; Chandran *et al.* 2023; Rouhi *et al.* 2023). This is evident also from our  $\bar{U}^*/y^*$  profiles (figure 8g), where the actuated profiles (blue profiles) depart from unity farther from the wall compared to the non-actuated profile (black profile). The conductive sublayer also thickens with wall oscillation, but it then thins substantially with increasing Prandtl number, so that at  $Pr = 7.5$  the conductive sublayer is substantially thinner than the viscous sublayer (figure 8i).

Viscous sublayer and conductive sublayer thickening due to the wall oscillation shifts the  $\bar{U}^*$  and  $\bar{\Theta}^*$  profiles. This is shown in figure 8(j,k,l) where we plot the differences  $\Delta\bar{U}^* = \bar{U}^* - \bar{U}_0^*$  and  $\Delta\bar{\Theta}^* = \bar{\Theta}^* - \bar{\Theta}_0^*$  between the actuated and the non-actuated cases. The cases with the maximum  $DR$  (or  $HR$ ) have the highest  $\Delta\bar{U}^*$  (or  $\Delta\bar{\Theta}^*$ ), as highlighted by the thick dashed line in the plots. The profiles in colour are from the production runs with the reduced domain (table 1), and are plotted up to  $y_{\text{res}}^* \simeq 170$ . As a reference, the profiles in grey are from the full-domain cases from Appendix A. There is a good agreement between the reduced-domain and the full-domain profiles up to  $y_{\text{res}}^*$ . Furthermore, the variations of  $\Delta\bar{U}^*$  and  $\Delta\bar{\Theta}^*$  beyond  $y_{\text{res}}^*$  are within 3%. Therefore, it is reasonable to consider  $\Delta\bar{U}^*$  and  $\Delta\bar{\Theta}^*$  at  $y_{\text{res}}^* = 170$  ( $\Delta\bar{U}_{170}^*$  and  $\Delta\bar{\Theta}_{170}^*$ ) as their asymptotic values. According to Rouhi *et al.* (2023), the distance  $y^*$  where  $\Delta\bar{U}^*$  reaches a plateau indicates the extent to which the Stokes layer disturbs the  $\bar{U}^*$  profile. In figure 8(j,k,l), therefore, we mark each profile at the  $y^*$  location where  $\Delta\bar{U}^* = 0.9\Delta\bar{U}_{170}^*$  ( $\Delta\bar{\Theta}^* = 0.9\Delta\bar{\Theta}_{170}^*$ ). For the present profiles with fixed  $Re_{\tau_0}, A^+$  and  $\kappa_x^+$ , the distance to reach the plateau in  $\Delta\bar{\Theta}^*$  depends on  $\omega^+$  and  $Pr$  (compare figures 8k,l), where the plateau is reached at a lower  $y^*$  with increasing Prandtl number. We expect that the  $\Delta\bar{\Theta}^*$  profiles and the distances to their plateaus would also depend on  $A^+$  and  $\kappa_x^+$ , but not on  $Re_{\tau_0}$ . Our conjecture is based on the behaviour of its analogue  $\Delta\bar{U}^*$  (figure 8j), that for a fixed set of actuation parameters is almost identical between  $Re_{\tau_0} = 590$  (thick blue dashed line) and  $Re_{\tau_0} = 950$  (green dashed-dotted line). The Reynolds number independence of the plateau in  $\Delta\bar{U}^*$  for the travelling wave is further confirmed by Gatti & Quadrio (2016) and Gatti *et al.* (2024).

In figure 9, we plot the turbulence statistics for the same cases shown in figure 8. Drag reduction and viscous sublayer thickening (figures 8a,d,g) coincide with the near-wall attenuation of  $\overline{u^2}^*$  and the shift in its inner peak (figure 9d), as known from previous work (Quadrio & Sibilla 2000; Ricco & Wu 2004; Quadrio & Ricco 2011; Touber & Leschziner 2012; Ricco *et al.* 2021; Rouhi *et al.* 2023). Similarly, we find that at each  $Pr$ , heat-transfer reduction and conductive sublayer thickening (figures 8b,c,e,f,h,i) coincide with the near-wall attenuation of  $\overline{\theta^2}^*$  and the shift in its inner peak (figures 9e,f). Interestingly,  $DR_{\text{max}}$  occurs when the inner peak in  $\overline{u^2}^*$  is located farthest from the wall, and a similar connection exists between  $HR_{\text{max}}$  and the location of the inner peak in  $\overline{\theta^2}^*$  (compare the listed numbers in figures 9d,e,f).

In addition, the attenuation of the turbulent shear-stress  $\overline{uv}^*$  (figure 9g) and the wall-normal turbulent temperature-flux  $\overline{\theta v}^*$  (figures 9h,i) are directly linked to  $DR$  and  $HR$ , respectively. In figure 9(j,k,l), we plot the differences between the actuated and non-actuated cases  $\Delta\overline{uv}^* = \overline{uv}^* - \overline{uv}_0^*$  and  $\Delta\overline{\theta v}^* = \overline{\theta v}^* - \overline{\theta v}_0^*$ . Most of the attenuation occurs near the wall, with the maxima occurring near  $y^* \simeq 10$ . For  $y^* > 10$ , the attenuation declines, and  $\Delta\overline{uv}^*$  and  $\Delta\overline{\theta v}^*$  reach local minima at points that coincide approximately with the locations of the peaks in  $\overline{uv}^*$  and  $\overline{\theta v}_0^*$ .

By integrating the plane- and time-averaged streamwise momentum (2.2) and temper-

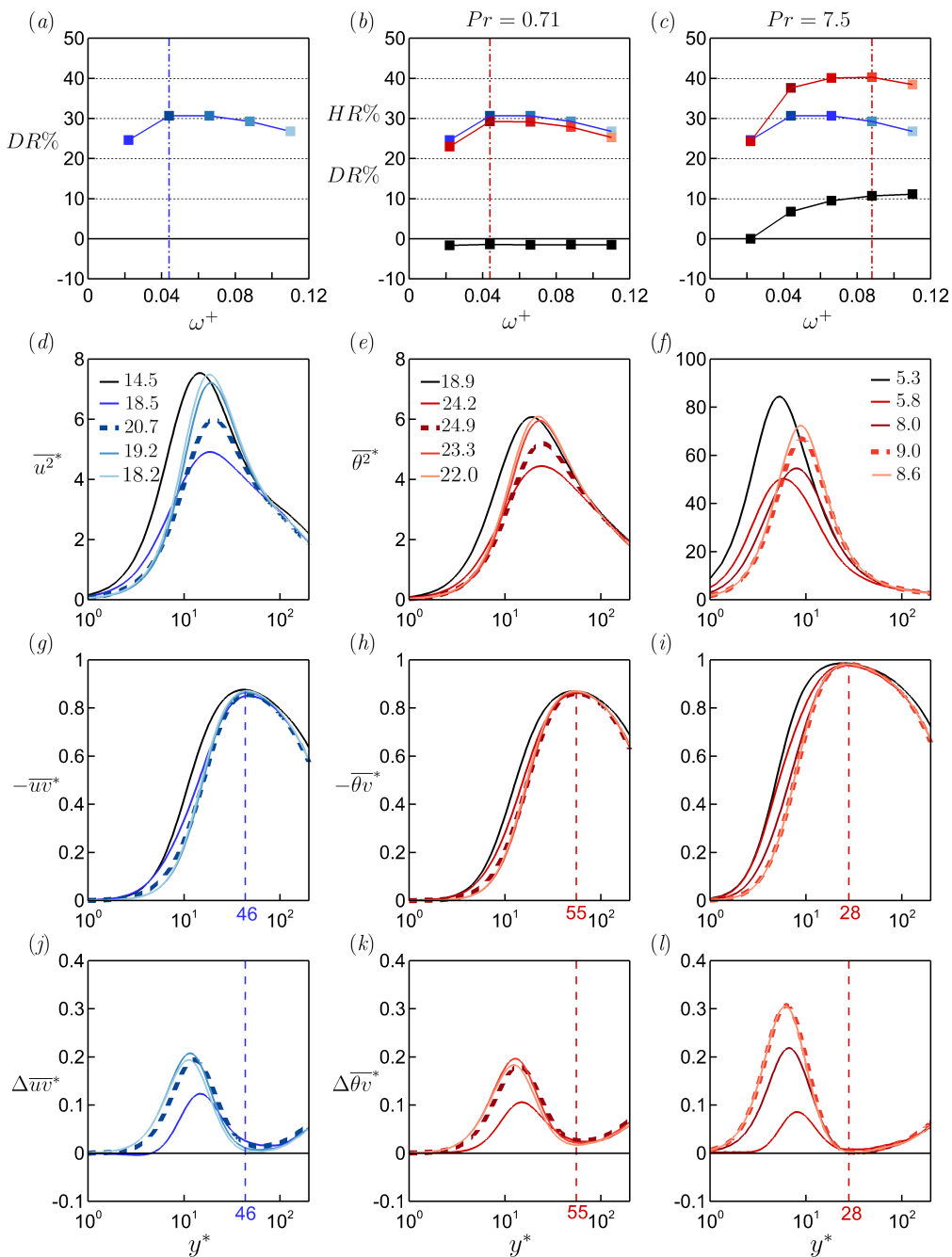


FIGURE 9. Travelling wave actuation with  $A^+ = 12$ ,  $\kappa_x^+ = 0.0014$ . Notation and symbols as in figure 8. Here,  $\Delta\overline{uw}^* = \overline{uw}^* - \overline{uw}_0^*$ , and  $\Delta\overline{\theta v}^* = \overline{\theta v}^* - \overline{\theta v}_0^*$ . In (d,e,f), the numbers give the  $y^*$  location of the inner-peak in the  $\overline{u^2}^*$  and  $\overline{\theta^2}^*$  profiles. In (g-l), the vertical dashed line locates the peak of non-actuated  $\overline{uw}_0^*$  (g,j) and  $\overline{\theta v}_0^*$  (h,i,k,l).



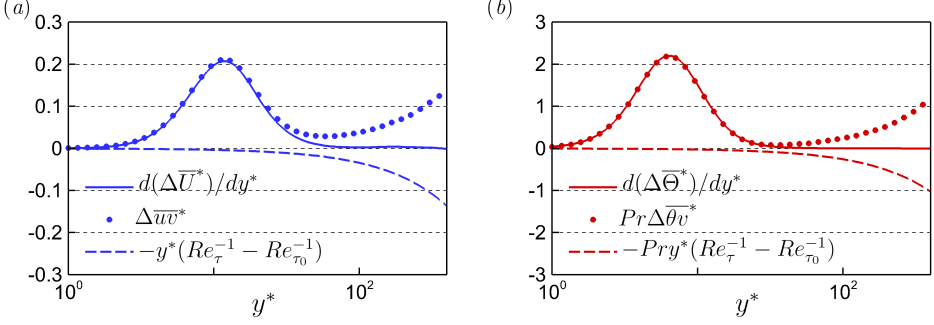


FIGURE 10. Travelling wave actuation with  $A^+ = 12$ ,  $\kappa_x^+ = 0.0014$ ,  $\omega^+ = 0.088$  at  $Pr = 7.5$ . (a) Terms in the averaged streamwise momentum equation (3.3a). (b) Terms in the averaged temperature equation (3.3b).

ature (2.3) equations from zero to  $y^*$ , we obtain

$$\frac{d\bar{U}^*}{dy^*} = \bar{u}\bar{v}^* + (1 - y^* Re_\tau^{-1}), \quad \frac{d\bar{\Theta}^*}{dy^*} = Pr \left[ \bar{\theta}\bar{v}^* + (1 - y^* Re_\tau^{-1}) + Res_\Theta \right], \quad (3.2a,b)$$

where  $Res_\Theta \equiv Re_\tau^{-1} \int_0^{y^*} (1 - \bar{U}^*/U_b^*) dy'$ . Hence,

$$\frac{d(\Delta\bar{U}^*)}{dy^*} = \Delta\bar{u}\bar{v}^* - y^* (Re_\tau^{-1} - Re_{\tau_0}^{-1}), \quad (3.3a)$$

$$\frac{d(\Delta\bar{\Theta}^*)}{dy^*} = Pr \left[ \Delta\bar{\theta}\bar{v}^* - y^* (Re_\tau^{-1} - Re_{\tau_0}^{-1}) + \underbrace{\Delta Res_\Theta}_{\simeq 0} \right]. \quad (3.3b)$$

The difference  $\Delta Res_\Theta$  between the actuated and the non-actuated cases is small and can be neglected. The remaining terms in (3.3a) and (3.3b) are plotted in figure 10 for the travelling wave case at  $Pr = 7.5$  and  $\omega^+ = 0.088$ . We see that the right-hand-side of (3.3a) and (3.3b) are dominated by  $\Delta\bar{u}\bar{v}^*$  and  $\Delta\bar{\theta}\bar{v}^*$ , up to their respective minima, but farther from the wall these terms are cancelled by the term containing the difference in Reynolds numbers ( $Re_\tau^{-1} - Re_{\tau_0}^{-1}$ ). That is, the net contributions to  $\Delta\bar{U}^*$  and  $\Delta\bar{\Theta}^*$ , hence  $DR$  and  $HR$ , come from  $\Delta\bar{u}\bar{v}^*$  and  $\Delta\bar{\theta}\bar{v}^*$ , and then only up to the points where  $\Delta\bar{u}\bar{v}^*$  and  $\Delta\bar{\theta}\bar{v}^*$  reach their minimum values.

#### 3.4. Source of inequality between $HR$ and $DR$

Integrating (3.3a) and (3.3b) once more with respect to  $y^*$  gives

$$\Delta\bar{U}_{y^*}^* = \int_0^{y^*} \Delta_{uv}^* dy', \quad \Delta\bar{\Theta}_{y^*}^* = Pr \int_0^{y^*} \Delta_{\theta v}^* dy', \quad (3.4a,b)$$

where

$$\Delta_{uv}^* \equiv \Delta\bar{u}\bar{v}^* - y^* (Re_\tau^{-1} - Re_{\tau_0}^{-1}), \quad (3.4c)$$

$$\Delta_{\theta v}^* \equiv \Delta\bar{\theta}\bar{v}^* - y^* (Re_\tau^{-1} - Re_{\tau_0}^{-1}). \quad (3.4d)$$

By using (3.4a,b) we can relate  $\Delta_{uv}^*$  and  $\Delta_{\theta v}^*$  to  $\Delta\bar{U}^*$  and  $\Delta\bar{\Theta}^*$ , hence to  $DR$  and  $HR$ , and so establish the connection between the drag and heat-transfer reduction and the turbulence attenuation. For the drag reduction, Gatti & Quadrio (2016) derived the

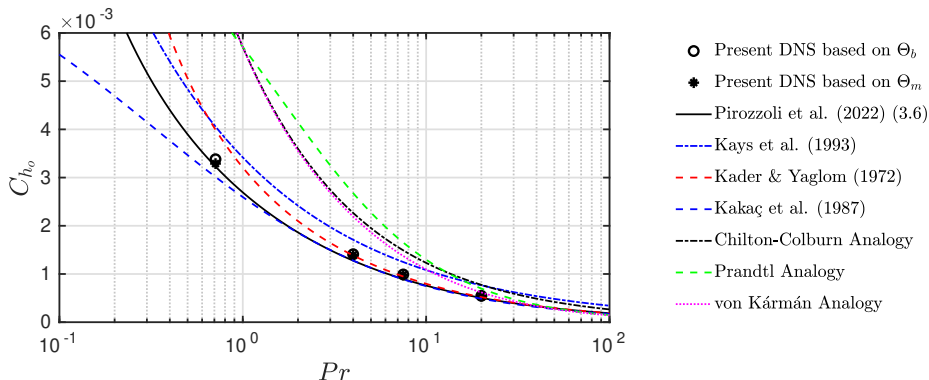


FIGURE 11. Comparison of the non-actuated  $C_{h_0}$  between our DNS cases (left side of table 1) and several empirical relations. For the DNS data,  $C_{h_0}$  is calculated either based on the bulk temperature  $\Theta_b$  (empty symbols) or the mixed-mean temperature  $\Theta_m$  (filled symbols). The empirical relations are by Pirozzoli *et al.* (2022) (3.6), Kays *et al.* (1993), Kader & Yaglom (1972), Kakaç *et al.* (1987), Chilton-Colburn Analogy (Chilton & Colburn 1934; Colburn 1964), Prandtl Analogy (see 11 in Schlünder 1998), and von Kármán Analogy (see 4 in Li & Li 2010).

relation between  $DR (= 1 - R_f)$  and the asymptotic value of  $\Delta\bar{U}^*$  in the log region (3.5a). In Appendix B, we derive a similar relation between  $HR (= 1 - R_h)$  and the asymptotic value of  $\Delta\bar{\Theta}^*$  in the log region (3.5b). That is, we have

$$\Delta\bar{U}_{170}^* = \sqrt{\frac{2}{C_{f_0}}} \left[ \frac{1}{\sqrt{R_f}} - 1 \right] - \frac{1}{2\kappa_u} \ln R_f = \underbrace{\int_0^{170} \Delta_{uv}^* dy'}_{I_{uv}} \quad (3.5a)$$

$$\Delta\bar{\Theta}_{170}^* = \frac{\sqrt{C_{f_0}/2}}{C_{h_0}} \left[ \frac{\sqrt{R_f}}{R_h} - 1 \right] - \frac{1}{2\kappa_\theta} \ln R_f = Pr \underbrace{\int_0^{170} \Delta_{\theta v}^* dy'}_{I_{\theta v}} \quad (3.5b)$$

These derivations assume that the profiles of  $\bar{U}^*$  and  $\bar{\Theta}^*$  have well-defined log regions with slopes that are not affected by the wall oscillation, which is the case for our results (figure 8). The integration was performed up to  $y_{\text{res}}^* = 170$ , where the profiles of  $\Delta\bar{U}^*$  and  $\Delta\bar{\Theta}^*$  reach their asymptotic levels (figures 8j,k,l) and their derivatives are zero (figure 10). On the right-hand-sides of (3.5a) and (3.5b) we have the integrals of attenuation in the turbulent shear-stress ( $I_{uv}$ ) and the turbulent temperature-flux ( $I_{\theta v}$ ). For a fixed set of viscous-scaled actuation parameters,  $I_{uv} = \Delta\bar{U}_{170}^*$  is constant (Gatti & Quadrio 2016; Rouhi *et al.* 2023) (also shown in figure 8j), but  $I_{\theta v} = \Delta\bar{\Theta}_{170}^*/Pr$  depends on  $Pr$  (figures 9k,l).

To predict  $DR$  and  $HR$  from (3.5a) and (3.5b), we only need  $\Delta\bar{U}_{170}^*$  and  $\Delta\bar{\Theta}_{170}^*$  (that is,  $I_{uv}$  and  $I_{\theta v}$ ) as the inputs; the other parameters are associated with the non-actuated channel flow for which semi-empirical relations exist in the literature. We choose  $\kappa_u = 0.4$  and  $\kappa_\theta = 0.46$  (Pirozzoli *et al.* 2016); the suitability of these choices is confirmed in §2.3 and Appendix A. Dean (1978)'s correlation is used for the non-actuated skin-friction coefficient  $C_{f_0} = 0.073(2Re_b)^{-1/4}$ , which could be re-expressed as  $C_{f_0} = 0.037Re_{\tau_0}^{-2/7}$ ; this correlation agrees well with the DNS data (MacDonald *et al.* 2019), and yields less than 2% difference with our DNS result  $C_{f_0} = 0.0057$  at  $Re_{\tau_0} = 590$ . For the non-actuated  $C_{h_0}$ , in figure 11 we compare our DNS data at  $Re_{\tau_0} = 590$  and different  $Pr$  (cases on the left side of table 1) with several empirical relations. These relations define

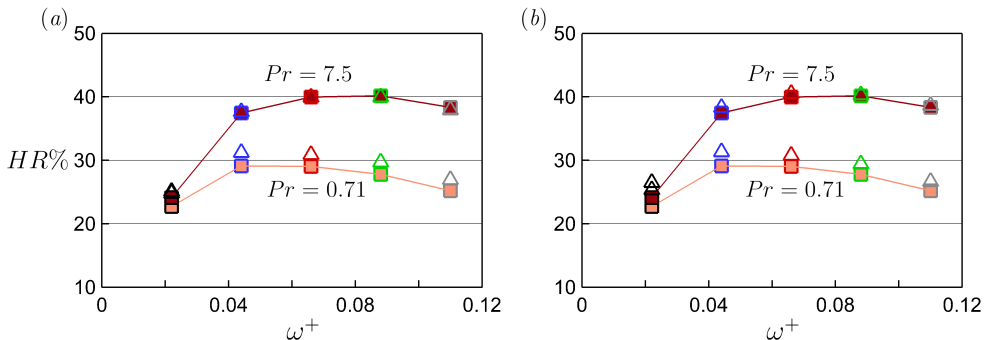


FIGURE 12. Travelling wave actuation with  $A^+ = 12$ ,  $\kappa_x^+ = 0.0014$ . Comparison between the direct  $HR$  from DNS (filled squares) and the predicted  $HR$  (empty triangles) by solving (3.5a) and (3.5b). In (a) for predicting  $HR$  we use  $I_{uv}$  and  $I_{\theta_v}$  directly from DNS. In (b) for predicting  $HR$  we use a power-law estimate for  $I_{\theta_v} = I_{uv}/Pr^\gamma$ , with the values of  $\gamma$  reported in figure 13(b).

$C_{h_0}$  either based on the bulk temperature  $\Theta_b$ , or the mixed-mean temperature  $\Theta_m$ . For our DNS data, there is a negligible difference between the two definitions (empty versus the filled circles). Among the relations, the latest correlation by Pirozzoli *et al.* (2022) agrees well with our DNS data (solid black line). This relation is an improvement to Kader & Yaglom (1972)'s formula, and its accuracy is supported by the recent DNS of Pirozzoli (2023) for  $\mathcal{O}(10^{-2}) \lesssim Pr \lesssim \mathcal{O}(10^1)$ . It is formulated as

$$\frac{1}{C_{h_0}} = \frac{\kappa_u}{\kappa_\theta} \frac{2}{C_{f_0}} + \left( \beta_{CL} - \beta_2 - \frac{\kappa_u}{\kappa_\theta} B \right) \sqrt{\frac{2}{C_{f_0}}} + \beta_3. \quad (3.6)$$

Here  $\beta_{CL}(Pr) = B_\theta(Pr) + 3.504 - 1.5/\kappa_\theta$ ,  $\beta_2 = 4.92$ ,  $\beta_3 = 39.6$ ,  $B = 1.23$ , and  $B_\theta(Pr)$  is the log-law additive constant for  $\bar{\Theta}^*$  (Kader & Yaglom 1972), as introduced in Appendix B.

In figure 12(a), we compare the values of  $HR$  from DNS with those from (3.5a) and (3.5b) using  $I_{uv}$  and  $I_{\theta_v}$  as obtained from DNS. The results support the accuracy of the model for relating  $HR$  to the attenuation of the turbulent flux. In figure 12(b), we also show the agreement between the model and the DNS when we use a power law estimate for  $I_{\theta_v}$  ( $= I_{uv}/Pr^\gamma$ ) where only  $I_{uv}$  (which is independent of  $Pr$ ) is obtained from DNS. We justify the power law as follows.

From (3.5b), we note that the Prandtl number dependence of  $HR$  (hence  $HR - DR$ ) is due to both  $C_{h_0}$  and  $I_{\theta_v}$ . According to the Reynolds analogy, we would expect  $I_{\theta_v} = I_{uv}$  when  $Pr = 1.0$ . Figure 13(a) indicates that, regardless of the actuation frequency  $\omega^+$ ,  $I_{\theta_v} > I_{uv}$  for  $Pr = 0.71$ , and  $I_{\theta_v} < I_{uv}$  for  $Pr > 1$ , with the difference increasing with  $Pr$ . In other words, increasing  $Pr$  beyond unity leads to a lower attenuation of  $\theta v$  compared to  $\bar{u}\bar{v}$ , even though in this regime  $HR > DR$  (figure 5c-f). Figure 13(b) shows how  $I_{\theta_v}$  depends on  $Pr$ , and that  $I_{\theta_v} = I_{uv}/Pr^\gamma$  is a good approximation to the data. For the present data with a fixed  $A^+$  and  $\kappa_x^+$ ,  $\gamma$  depends on  $\omega^+$  but it is independent of  $Pr$ . When we use this power law in (3.5b) and solve for  $HR$  by using  $I_{uv}$  from DNS, figures 13(c,d) show that the model closely matches the data. Furthermore, for  $\gamma < 0.5$  we can achieve  $HR > DR$  for  $Pr > 1$ , and the smaller  $\gamma$  is the higher  $HR$  is compared to  $DR$ . From figures 13(b,d), as  $\omega^+$  increases from 0.022 (black curve) to 0.110 (grey curve),  $\gamma$  decreases from about 0.5 to 0.1, and  $HR - DR$  increases from almost zero to 10%. Therefore, we expect  $HR < DR$  for  $Pr > 1.0$  if  $\gamma > 0.5$ . This occurs for the plane oscillation at  $\omega^+ = 0.022$ , where  $\gamma = 2.43$  and  $HR - DR \simeq -5\%$  (figure 21).

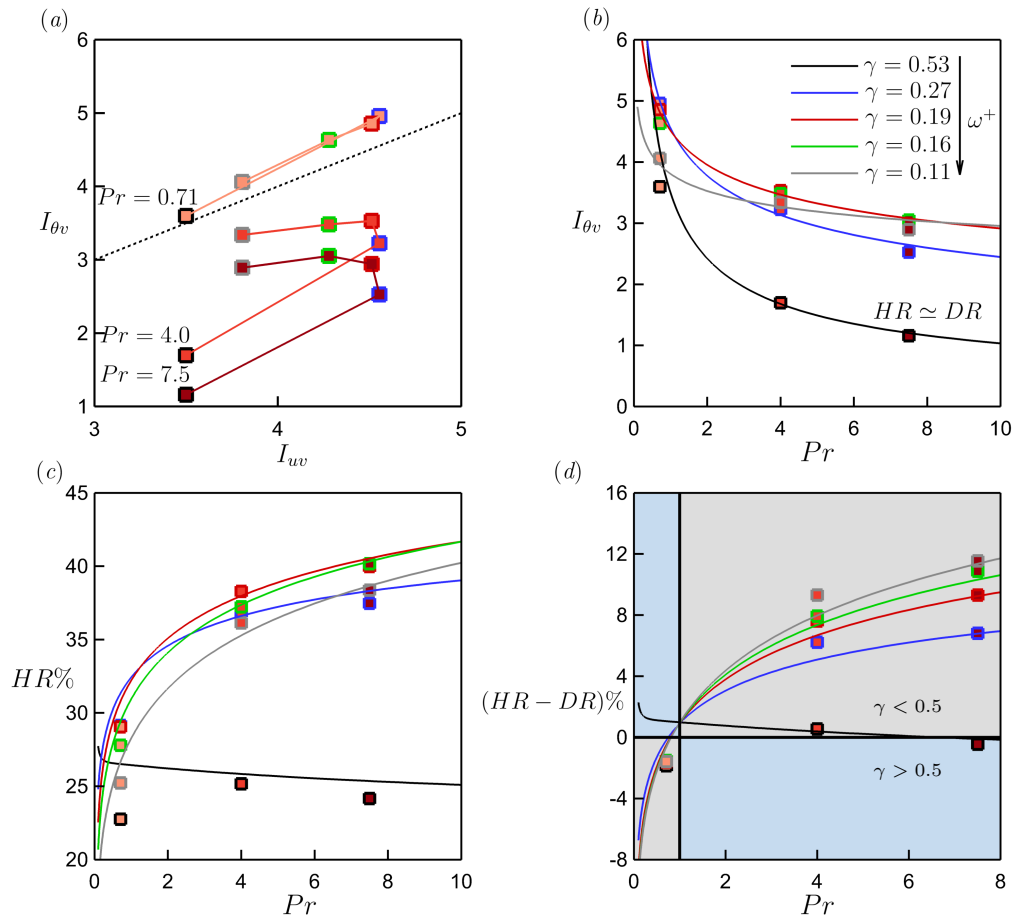


FIGURE 13. Travelling wave at  $Pr = 0.71, 4.0$  and  $7.5$  (same data as in figure 5*a,c,e*). The outline colour of each data point indicates its  $\omega^+$ ;  $\omega^+ = 0.022$  (black),  $0.044$  (blue),  $0.066$  (red),  $0.088$  (green) and  $0.110$  (grey). (a)  $I_{\theta v}$  versus  $I_{uv}$ ; the dotted line is for  $I_{\theta v} = I_{uv}$ . (b)  $I_{\theta v}$  versus  $Pr$ ; the solid curves are the power-law fit  $I_{\theta v} = I_{uv}/Pr^\gamma$ , with  $\gamma$  as shown. (c,d)  $HR$  and  $HR - DR$  versus  $Pr$ ; the solid curves are the prediction of (3.5*b*) using  $I_{\theta v} = I_{uv}/Pr^\gamma$ . In (d) blue zone marks  $\gamma > 0.5$ , grey zone marks  $\gamma < 0.5$ .

### 3.5. Heat transfer reduction at higher Prandtl number and Reynolds number

Gatti & Quadrio (2016) used (3.5*a*) to extrapolate their low Reynolds number  $DR$  data to higher Reynolds numbers, and the accuracy of this extrapolation was corroborated by Rouhi *et al.* (2023) up to  $Re_{\tau_0} = 4000$  using LES, and by Gatti *et al.* (2024) up to  $Re_{\tau_0} = 6000$  using DNS. For a fixed set of actuation parameters ( $A^+$ ,  $\kappa_x^+$ ,  $\omega^+$ ),  $I_{uv}$  is Reynolds and Prandtl number independent, and so the only Reynolds number dependency of  $DR$  is through  $C_{f_0}$ . Hence, Gatti & Quadrio (2016) could solve (3.5*a*) and predict  $DR$  at any Reynolds number. We can now do the same for  $HR$  by using the power law relationship  $I_{\theta v} = I_{uv}/Pr^\gamma$ . By knowing  $I_{uv}$  and  $\gamma$  for a fixed set of actuation parameters, we can then solve (3.5*a*) and (3.5*b*) to map  $HR$  and  $HR - DR$  as functions of  $Pr$  and  $Re_{\tau_0}$ .

In figure 14(*a,b*), we show these predictions for the travelling wave case with  $\omega^+ = 0.088$ , where the DNS gives  $I_{uv} = 4.28$  and  $\gamma = 0.16$  (data points with green outline in figure 13). The predictions agree well with the DNS data points, including the point at

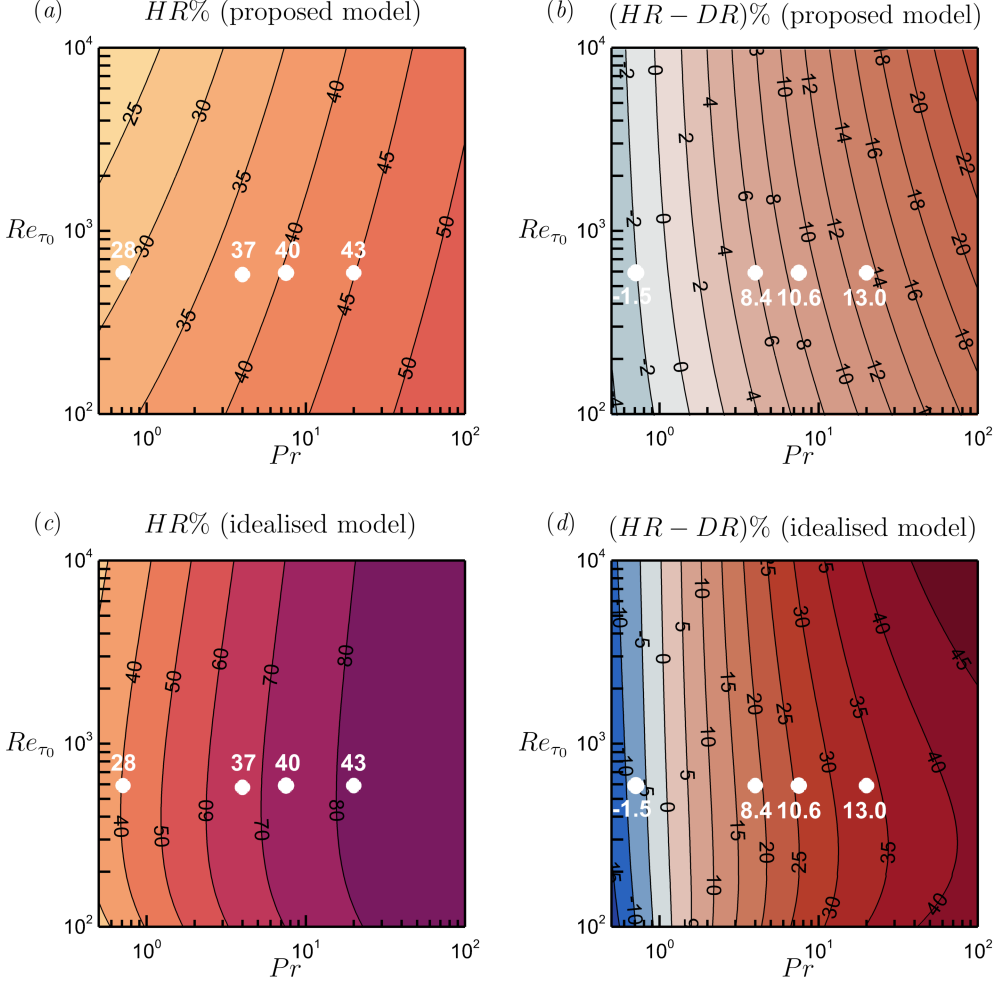


FIGURE 14. Predicted maps of (a,c)  $HR$  and (b,d)  $HR - DR$  for the travelling wave with  $A^+ = 12$ ,  $\kappa_x^+ = 0.0014$  and  $\omega^+ = 0.088$ . (a,b) are obtained from our proposed model  $I_{\theta v} = I_{uv}/Pr^\gamma$  with  $I_{uv} = 4.28$ ,  $\gamma = 0.16$  obtained from DNS, and by solving (3.5a, 3.5b). (c,d) are obtained from the simplified model (3.7a, 3.7b) and by solving (3.5a, 3.5b). The white bullets represent DNS results at  $Re_{\tau_0} = 590$  for  $Pr = 0.71, 4.0, 7.5$  and  $20$ .

$Pr = 20$  ( $HR = 43\%$ ,  $HR - DR = 13\%$ ) (see table 4). At a given Reynolds number,  $HR$  increases almost logarithmically with Prandtl number. For instance, at  $Re_{\tau_0} = 590$   $HR$  increases from 30% to 40% as the Prandtl number increases from 0.71 to 7.5, and  $HR = 50\%$  would be obtained at a Prandtl number of about 75. In addition,  $HR$  decreases very slowly with increasing  $Re_{\tau_0}$ . For instance, at  $Pr = 7.5$   $HR$  decreases from 40% to about 36% as  $Re_{\tau_0}$  increases from 590 to 5900. Such a slow decrease with  $Re_{\tau_0}$  is similarly observed in the predictive model for  $DR$  (3.5a) (Marusic *et al.* 2021; Rouhi *et al.* 2023; Gatti *et al.* 2024).

In figure 14(c,d), we predict  $HR$  and  $HR - DR$  for the same actuated case as in figure 14(a,b), but with a simplified analytical approach, similar to that proposed by Iwamoto *et al.* (2005). The approach assumes that turbulence is completely damped in

the near-wall region, which here we consider that to be up to the Stokes layer protrusion height  $\ell_{0.01}^*$  (figure 15a). Therefore, for  $0 \leq y^* \leq \ell_{0.01}^*$  the profiles are assumed to be laminar  $\overline{U}^* = y^*[1 - y^*/(2Re_\tau)]$ ,  $\overline{\Theta}^* = Pr y^*[1 - y^*/(2Re_\tau)]$ , and for  $y^* > \ell_{0.01}^*$  the profiles follow the turbulent formulations (C1a, C1b). By matching the laminar and turbulent profiles at  $y^* = \ell_{0.01}^*$ , we obtain

$$\Delta \overline{U}_{170}^* = \ell_{0.01}^* \left( 1 - \frac{\ell_{0.01}^*}{2Re_\tau} \right) - \left( \frac{1}{\kappa_u} \ln \ell_{0.01}^* + B_u \right) \quad (3.7a)$$

$$\Delta \overline{\Theta}_{170}^* = Pr \ell_{0.01}^* \left( 1 - \frac{\ell_{0.01}^*}{2Re_\tau} \right) - \left( \frac{1}{\kappa_\theta} \ln \ell_{0.01}^* + B_\theta \right). \quad (3.7b)$$

We substitute for  $\Delta \overline{U}_{170}^*$ ,  $\Delta \overline{\Theta}_{170}^*$  in (3.5a, 3.5b) to predict  $HR$  and  $HR - DR$ . With this approach, the predicted  $HR$  and  $HR - DR$  increase with  $Pr$  (figure 14c,d), consistent with our proposed model and DNS (figure 14a,b). However, quantitatively, this approach over-predicts  $HR$  and  $HR - DR$  by two times compared to the DNS data and our proposed model, which is of no surprise. The Stokes layer does not completely attenuate the near-wall turbulence, even down to  $y^* \sim \mathcal{O}(1)$  (figure 9). The level of attenuation results from the complex interaction between the Stokes layer and the near-wall velocity and thermal fields, as we discuss next.

### 3.6. Stokes layer interaction with the velocity and thermal fields: integral parameters

For  $Re_{\tau_0} \lesssim \mathcal{O}(10^3)$ , the primary source of drag reduction is the protrusion of the Stokes layer due to the wall oscillation that modifies the near-wall velocity field (Choi *et al.* 1998; Choi & Clayton 2001; Choi 2002; Choi *et al.* 2002; Quadrio & Sibilla 2000; Ricco 2004; Quadrio & Ricco 2011; Ricco *et al.* 2021), and we would expect that a similar interaction between the Stokes layer and the near-wall temperature field leads to  $HR$ . As a result, the near-wall  $\overline{u^2}^*$  profiles are modified (figure 9d), consistent with the literature (Jung *et al.* 1992; Baron & Quadrio 1995; Choi *et al.* 1998; Choi & Clayton 2001; Quadrio & Sibilla 2000; Ricco & Wu 2004; Quadrio & Ricco 2011; Toubert & Leschziner 2012; Ricco *et al.* 2012; Rouhi *et al.* 2023), and similar trends are seen in the  $\overline{\theta^2}^*$  profiles (figures 9e,f). To determine how the Stokes layer affects  $I_{uv}$  and  $I_{\theta v}$  as the Prandtl number changes, we first identify the Stokes layer characteristics through the harmonic component of the spanwise velocity  $\overline{\tilde{w}^2}$ , where  $\tilde{w}$  is obtained by applying triple decomposition

$$W(x, y, z, t) = \overline{W}(y) + \tilde{w}(x, y, t) + w(x, y, z, t), \quad (3.8a)$$

$$\tilde{w}(x, y, t) = \frac{1}{N} \underbrace{\sum_{n=0}^{N-1} W(x, y, t + nT_{osc}) - \overline{W}(y)}_{\langle W \rangle(x, y, t)}. \quad (3.8b)$$

Here,  $\overline{W}$  is the plane- and time-averaged component of the spanwise velocity,  $\tilde{w}$  is the harmonic component,  $w$  is the turbulent component, and  $\langle W \rangle$  is the spanwise and phase averaged value of  $W$ . For the streamwise and wall-normal velocities and the temperature field, the harmonic components are negligible compared the turbulent components. Following Rouhi *et al.* (2023), we quantify the Stokes layer protrusion height  $\ell_{0.01}^*$  as the wall distance where  $\overline{\tilde{w}^2}^* = 0.01$ , and we locate the Stokes layer thickness  $\delta_S^*$  where  $\overline{\tilde{w}^2}^* = \frac{1}{2} A^{*2} e^{-2}$ . We also calculate the production due to the Stokes layer according to  $P_{33}^* \equiv -2\langle wv \rangle \partial \tilde{w} / \partial y^* - 2\langle wu \rangle \partial \tilde{w} / \partial x^*$ , where  $P_{33}^*$  is the only external source term due to the Stokes layer that injects energy into the turbulent stress budgets (Toubert & Leschziner 2012; Umair *et al.* 2022).

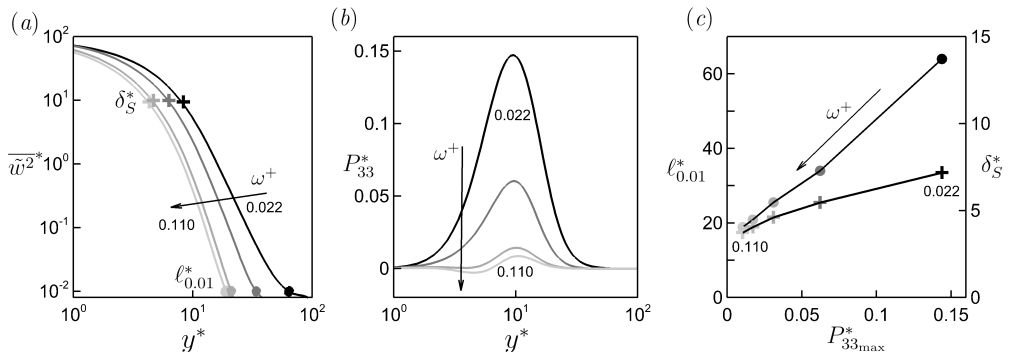


FIGURE 15. Characteristics of the Stokes layer for the travelling wave with  $A^+ = 12$ ,  $\kappa_w^+ = 0.0014$  and  $0.022 \leq \omega^+ \leq 0.110$  (same cases as in figure 5*a,c,e*). Results are independent of Prandtl number. The colour of the profiles and data points change from black at  $\omega^+ = 0.022$  to light grey at  $\omega^+ = 0.110$ . (a) Profiles of  $\overline{w}^{2*}$ . Stokes layer protrusion height  $\ell_{0.01}^*$  (Rouhi *et al.* 2023) marked at  $\overline{w}^{2*} = 0.01$  (filled bullets); laminar Stokes layer thickness  $\delta_S^*$  marked at  $\overline{w}^{2*} = \frac{1}{2}A^{*2}e^{-2}$  (cross symbols). (b) Production due to the Stokes layer  $P_{33}^*$ . (c)  $\ell_{0.01}^*$  (filled bullets) and  $\delta_S^*$  (cross symbols) versus the maximum value of  $\tilde{P}_{33}^*$ .

The behaviour of these Stokes layer parameters is given in figure 15, for the same travelling wave cases shown in figure 5(*a,c,e*). The profiles do not depend on  $Pr$ , that is, at a fixed  $\omega^+$  the Stokes layer structure remains unchanged as the Prandtl number changes. When  $\omega^+$  decreases,  $\ell_{0.01}^*$  and the maximum production increase proportionately (figure 15*c*). In other words, the Stokes layer becomes more protrusive while injecting more energy into the turbulent field. We note that  $\ell_{0.01}^*$  is almost linearly proportional to  $P_{33_{max}}^*$ , but  $\delta_S^*$  is less responsive to the rise in the production. Therefore,  $\ell_{0.01}^*$  better quantifies the Stokes layer protrusion and strength, as sensed by the turbulent field, in agreement with the observations by Rouhi *et al.* (2023).

In figure 16, we assess the relation between the integral quantities  $DR$ ,  $HR$ ,  $I_{\theta v}$ ,  $I_{uv}$ , and the Stokes layer characteristics. Rouhi *et al.* (2023) showed that  $DR$  increases with  $\ell_{0.01}^*$  up to an optimal value for maximum  $DR$ , corresponding to an optimal level of  $P_{33_{max}}^*$ . For our present cases, this optimal point is  $\ell_{0.01}^* = 34$  (figure 16*b*), where protrusion beyond this point causes  $DR$  to decrease. We observe a similar trend in  $HR$  (figure 16*b*), but the corresponding optimal value of  $\ell_{0.01}^*$  for maximum  $HR$  decreases from 34 to 21 as the Prandtl number increases from 0.71 to 7.5. Figures 16(*c,d*) show that the variations of  $I_{uv}$  and  $I_{\theta v}$  with  $\omega^+$  and  $\ell_{0.01}^*$  are consistent with the trends in  $DR$  and  $HR$ . In terms of variations with  $Pr$ , however,  $HR$  increases even as  $I_{\theta v}$  decreases. From  $Pr = 0.71$  to 7.5, the maximum value of  $I_{\theta v}$  shifts to smaller values of  $\ell_{0.01}^*$ , corresponding to a shift in  $\omega^+$  from 0.044 ( $\ell_{0.01}^* = 34$ ) to 0.088 ( $\ell_{0.01}^* = 21$ ). Finally, it appears that the exponent  $\gamma$  in the power law increases almost linearly with  $\ell_{0.01}^*$  and  $P_{33_{max}}^*$  (figure 16*d*).

To summarise, we find that for  $Pr > 1$ , achieving maximum  $HR$  requires a less protrusive Stokes layer than achieving maximum  $DR$ . As the Stokes layer becomes more protrusive (energetic), it loses its efficacy in attenuating  $\theta v^*$  relative to  $\overline{w}^{2*}$ , that is,  $\gamma$  increases as  $\ell_{0.01}^*$  increases.

### 3.7. Stokes layer interaction with the velocity and thermal fields: scale-wise analysis

To better understand our observations on the integral parameters shown in figure 16, we now examine the spectrograms of  $\overline{w}^{2*}$  and  $\theta v^*$  and visualise the distributions of the instantaneous  $uv$  and  $\theta v$  near the wall. We focus on two cases at  $Pr = 7.5$ , Case A at

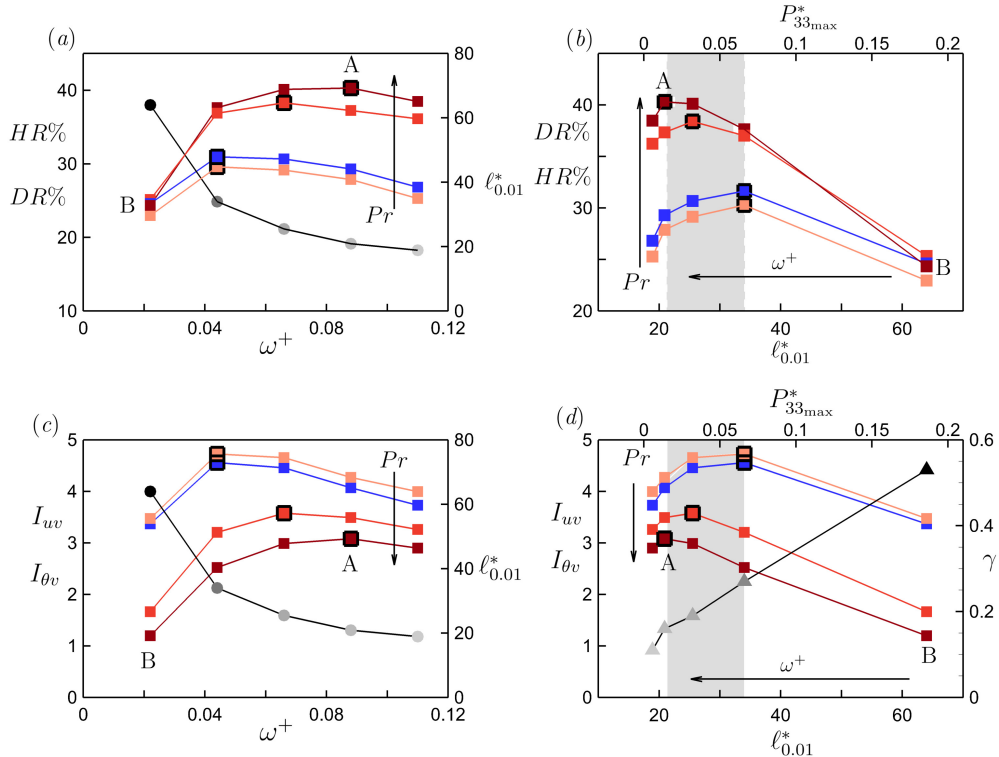


FIGURE 16. Variation of the integral parameters with the Stokes layer characteristics ( $\ell_{0.01}^*$ ,  $P_{33max}^*$ ) for the same travelling wave cases as in figure 15. (a)  $DR$  (blue squares),  $HR$  (light orange to brick red squares),  $\ell_{0.01}^*$  (black to grey bullets) versus  $\omega^+$ . (b) Same data as in (a) versus  $\ell_{0.01}^*$  (bottom axis) and  $P_{33max}^*$  (top axis). (c, d) correspond to (a, b) for  $I_{uv}$  (blue squares) and  $I_{\theta_v}$  (light orange to brick red squares); in (d) we overlay  $\gamma$  (grey to black triangles). In all plots, the colour of  $HR$  and  $I_{\theta_v}$  changes from light orange at  $Pr = 0.71$  to brick red at  $Pr = 7.5$ . The points associated with  $DR_{max}$  and  $HR_{max}$  are highlighted with a larger symbol size and black outline. In (b, d), the grey region shades the range of  $DR_{max}$  and  $HR_{max}$ . In all plots we highlight two cases that we further analyse in figures 17 and 18: Case A at  $\omega^+ = 0.088$  with  $\gamma = 0.16$ , and Case B at  $\omega^+ = 0.022$  with  $\gamma = 0.53$ .

$\omega^+ = 0.088$ , where  $HR$  is maximum and  $DR$  is near maximum ( $\gamma = 0.16$ ), and Case B at  $\omega^+ = 0.022$ , where  $HR$  and  $DR$  drop below their maximum values, owing to a highly protrusive Stokes layer ( $\gamma = 0.53$ ).

Figure 17 displays the various pre-multiplied spectrograms for these two cases, where  $\phi$  is the spectral density,  $k_x$  is the streamwise wavenumber,  $k_z$  is the spanwise wavenumber, and  $f$  is the frequency. The differences between the actuated and the non-actuated cases are denoted by, for example,  $\Delta k_x^* \phi_{uv}^* = k_x^* \phi_{uv}^* - k_x^* \phi_{uv0}^*$ . The extent up to which  $\Delta k_x^* \phi_{uv}^*$  and  $\Delta k_x^* \phi_{\theta_v}^*$  are non-zero (red and blue fields in figures 17e, f, q, r) coincides with the height of the Stokes layer protrusion  $\ell_{0.01}^*$  (horizontal dashed line); this supports the robustness of  $\ell_{0.01}^*$  to measure the extent up to which the Stokes layer modifies the turbulent field. Overall, for both Cases A and B, and  $k_x^* \phi_{uv}^*$  and  $k_x^* \phi_{\theta_v}^*$ , the Stokes layer protrusion (production) leads to two outcomes: (1) large-scale energy attenuation as a favourable outcome (positive  $\Delta k_x^* \phi_{uv}^*$ ,  $\Delta k_x^* \phi_{\theta_v}^*$  for  $\lambda_x^* \gtrsim 350$ , shown as the red fields in figures 17e, f, q, r), and (2) small-scale energy amplification as an unfavourable outcome (negative  $\Delta k_x^* \phi_{uv}^*$ ,  $\Delta k_x^* \phi_{\theta_v}^*$  for  $\lambda_x^* \lesssim 350$ , shown as the blue fields). The large-scale energy



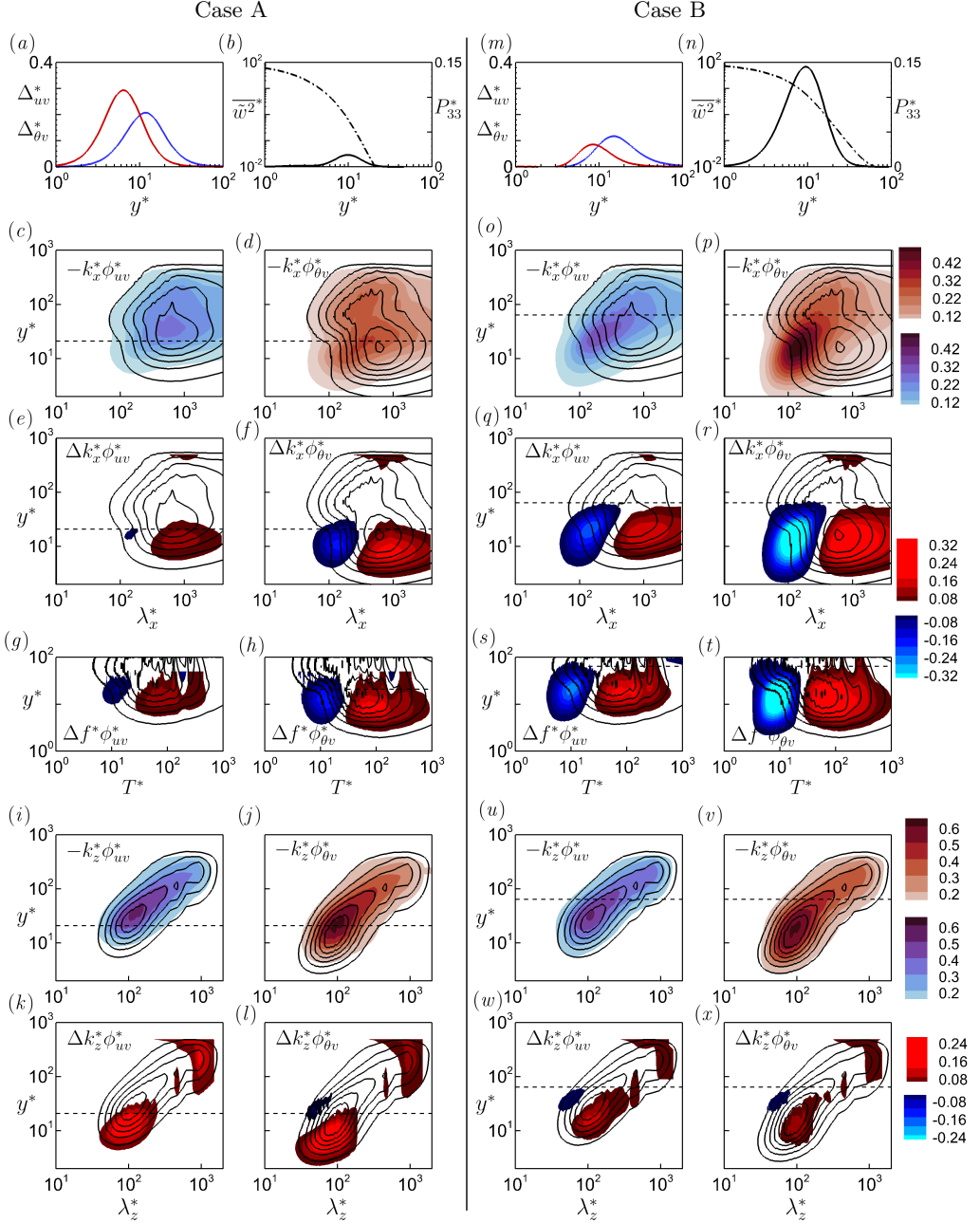


FIGURE 17. Comparisons between Case A (left two columns) and Case B (right two columns). (a,m) Profiles of  $\Delta_{uv}^*$  (blue) and  $\Delta_{\theta v}^*$  (red). (b,n) Profiles of  $\overline{w}^{2*}$  (dashed-dotted line) and  $P_{33}^*$  (solid line). Streamwise spectrograms: (c,o)  $-k_x^* \phi_{uv}^*$ ; (d,p)  $-k_x^* \phi_{\theta v}^*$  (contour lines and contour fields represent non-actuated and actuated cases, respectively). Difference between the actuated and the non-actuated cases for the wavenumber spectra (e,f,q,r), and frequency spectra (g,h,s,t). Spanwise spectrograms: (i,u)  $-k_z^* \phi_{uv}^*$ ; (j,v)  $-k_z^* \phi_{\theta v}^*$ . Difference between the actuated and the non-actuated cases (k,l,w,x). In all the spectrograms, the horizontal dashed line marks  $\ell_{0.01}^*$ .

attenuation corresponds to the attenuation of the near-wall streaks with  $\lambda_x^* \simeq 10^3$  (see the energetic peaks in the non-actuated spectrograms). The small-scale energy amplification corresponds to the emergence of smaller scales with  $\lambda_x^* \simeq 10^2$  (figures 18*j-ac*). The drastic changes in the streamwise spectrograms (figure 17*e,f,g,r*) are echoed in the response of the frequency spectrograms (figures 17*g,h,s,t*). Changing the actuation frequency  $\omega^+$ , hence changing the Stokes layer time-scale, modifies the near-wall turbulence time-scale  $T^*$ , which in turn modifies the streamwise length-scale  $\lambda_x^*$  (of course,  $T^*$  is related to  $\lambda_x^*$  through a convection speed  $\sim \mathcal{O}(10)$  according to Taylor's hypothesis).

Further insight can be gained by comparing the near-wall instantaneous fields of  $uv$  and  $\theta v$ , as shown in figure 18. The response of  $uv$  to the Stokes layer (blue intensity fields) largely follows the trends seen in  $\Delta k_x^* \phi_{uv}^*$  and  $\Delta f^* \phi_{uv}^*$ . For Case A, we see that the large scales associated with the near-wall streaks are attenuated. At the same time, sparse patches of smaller scales with  $\lambda_x^* \simeq 10^2$  ( $T^* \simeq 10$ ) emerge. For Case B, the emerging smaller scales possess a similar structure and size to those in Case A, but with a noticeably larger population; they appear as large and closely spaced patches that cover a significant area of the near-wall region. Consistently, negative regions of  $\Delta k_x^* \phi_{uv}^*$  and  $\Delta f^* \phi_{uv}^*$  are small for Case A (figure 17*e,g*), and large for Case B (figure 17*q,s*). Thus,  $I_{uv}$  and  $DR$  are greater for Case A than for Case B (figure 16). Attenuation of the large scales associated with the near-wall streaks is considered to be a primary source of drag reduction, as extensively reported in the literature (Baron & Quadrio 1995; Di Cicca *et al.* 2002; Karniadakis & Choi 2003; Ricco 2004; Quadrio *et al.* 2009; Touber & Leschziner 2012; Ricco *et al.* 2021; Marusic *et al.* 2021; Rouhi *et al.* 2023). However, amplification of the smaller scales as a source of drag increase, is reported to a lesser extent. Touber & Leschziner (2012) observed such amplification in the frequency spectrograms  $f^* \phi_{uv}^*$ ,  $f^* \phi_{vv}^*$ , and  $f^* \phi_{uw}^*$ . Consistent with our figure 17, they noted that as  $\omega^+$  changes from 0.06 to 0.03, and the Stokes layer production (protrusion) increases, energy accumulates in the scales with  $T^* \simeq 10$ , and  $DR$  decreases. Similarly, energy amplification at  $T^* \simeq 10$  is observed in  $f^* \phi_{\tau\tau}^*$  by Chandran *et al.* (2023), and in the near-wall  $f^* \phi_{uv}^*$  by Deshpande *et al.* (2023).

As to the  $\theta v$  field (brick intensity fields in figure 18), we see that with  $Pr > 1.0$  the Stokes layer modifies the  $\theta v$  field more than the  $uv$  field. In Case A, for example, the scales with  $\lambda_x^* \simeq 10^2$  and  $T^* \simeq 10$  are more frequent and more densely populated in the  $\theta v$  fields (figures 18*l,m,r,s*) than in the  $uv$  fields (figures 18*j,k,p,q*). Consistently,  $\Delta k_x^* \phi_{\theta v}^*$  (figure 17*f*) is more positive than  $\Delta k_x^* \phi_{uv}^*$  (figure 17*e*) for  $\lambda_x^* \gtrsim 350$ , and more negative for  $\lambda_x^* \lesssim 350$ . We can make the same observations with respect to Case B (figures 17*q,r*). As a result, at each  $\omega^+$ ,  $I_{\theta v}$  falls below  $I_{uv}$  when  $Pr > 1$  (figure 16*c,d*).

At a fixed  $\omega^+$ ,  $uv$  and  $\theta v$  are exposed to an identical Stokes layer. However, the larger change in  $\Delta k_x^* \phi_{\theta v}^*$  compared to  $\Delta k_x^* \phi_{uv}^*$  for  $Pr > 1$  implies that the energetic near-wall scales of  $\theta v$  are locally exposed to a stronger Stokes layer production. We establish this connection by evaluating the local Stokes layer production  $P_{33p}^*$  at the negative peaks of  $\Delta k_x^* \phi_{\theta v}^*$  and  $\Delta k_x^* \phi_{uv}^*$ ; these peaks are associated with the energetic small scales with  $\lambda_x^* \simeq 10^2$ , that contribute to the drop in  $I_{uv}$  and  $I_{\theta v}$ . Figure 19*(b)* demonstrates this process for Case B (figure 17*r*), where the negative peak of  $\Delta k_x^* \phi_{\theta v}^*$  is intersected with the  $P_{33}^*$  profile. With increasing  $Pr$ , the conductive sublayer thins, and the negative peak in  $\Delta k_x^* \phi_{\theta v}^*$  falls closer to the wall compared to its counterpart from  $\Delta k_x^* \phi_{uv}^*$ . This means that at each  $\omega^+$ , the energetic small scales of  $\theta v$  are exposed to a larger Stokes layer production, hence have a higher energy. This leads to the drop in  $I_{\theta v}$  compared to  $I_{uv}$ , as demonstrated in figure 19*(a)*. At  $Pr = 0.71$ , the local production  $P_{33p}^*$  is close between  $uv$  and  $\theta v$ , and  $I_{uv}$  and  $I_{\theta v}$  are close to each other. However, at  $Pr = 4.0$  and  $7.5$ ,  $P_{33p}^*$  at each  $\omega^+$  is several times higher for  $\theta v$  than  $uv$ , and  $I_{\theta v}$  drops below  $I_{uv}$ . In addition,

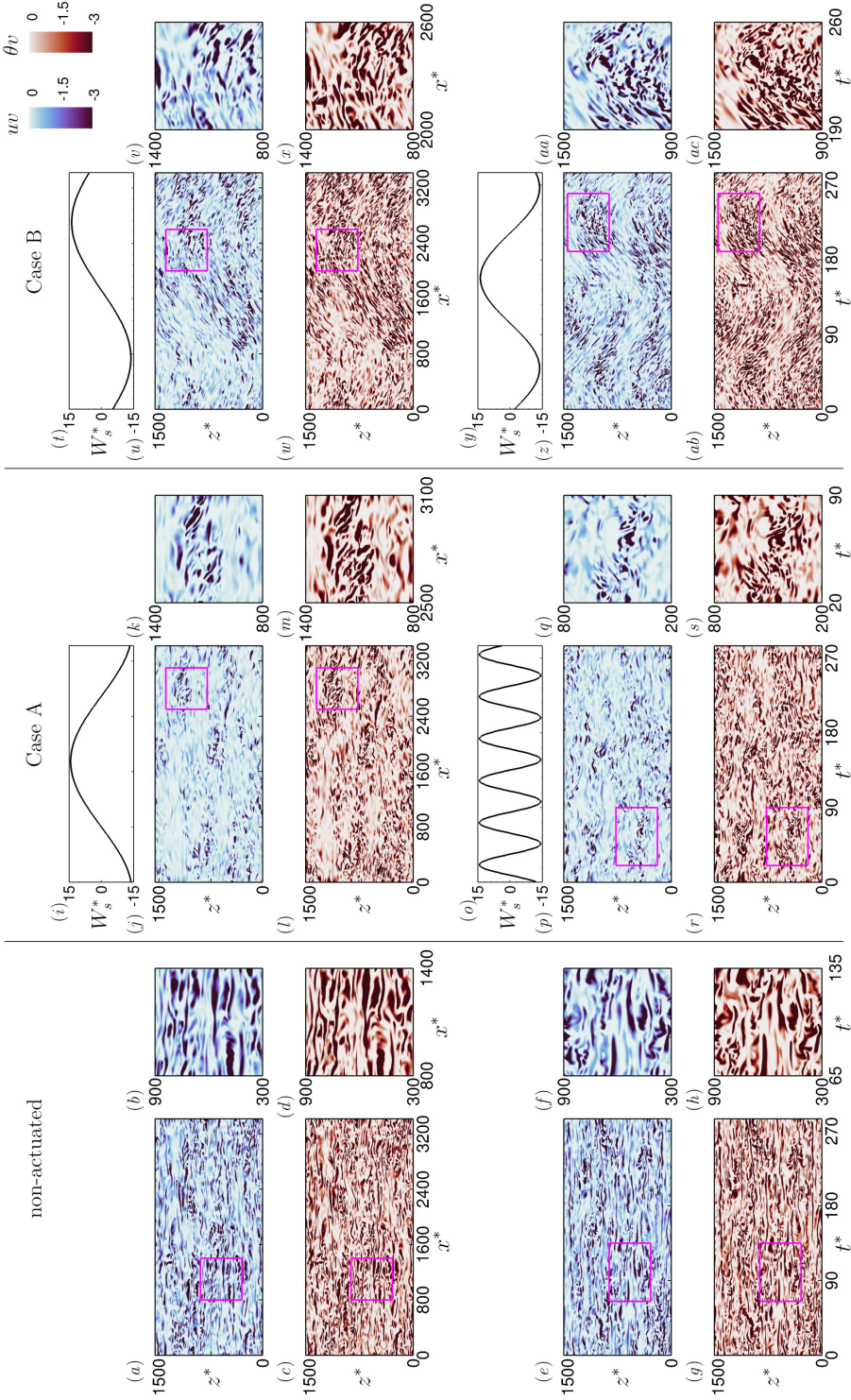


FIGURE 18. Visualisations of the instantaneous fields of  $uv$  (blue intensity fields) and  $\theta v$  (brick intensity fields) at  $y^+ = 14$  for the same cases as in figure 17. Next to each field, we magnify the small square outlined in pink. Left: non-actuated case; middle: actuated Case A; right: actuated Case B. The top two rows visualise  $uv$  and  $\theta v$  at one time over the  $x^*-z^*$  plane.  $(i, j)$  plot the corresponding spanwise wall velocity  $W_s^*$  over  $x^*$  at the same time. The bottom two rows visualise  $uv$  and  $\theta v$  at one  $x^*$ -location over  $z^*$  and time  $t^*$ .  $(o, y)$  plot  $W_s^*$  over  $t^*$  at the same  $x^*$ -location.

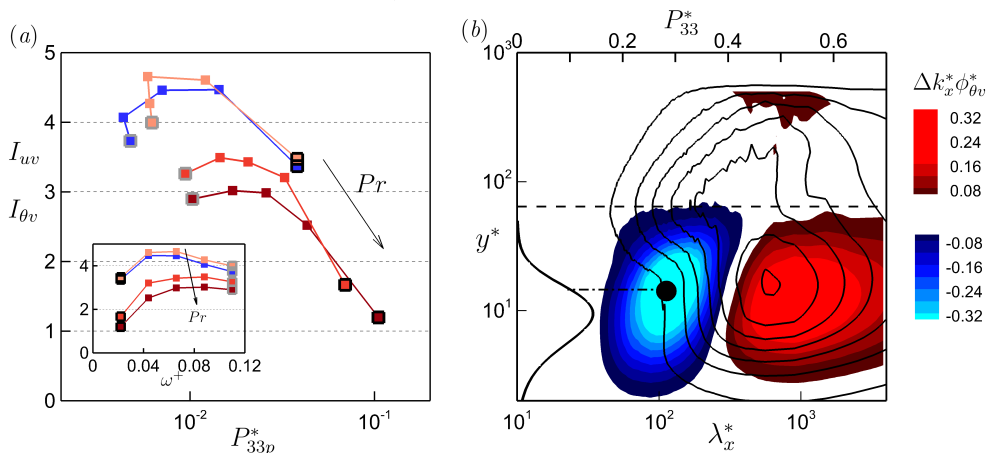


FIGURE 19. Assessment of the relation between  $I_{uv}$  and  $I_{\theta v}$ , and the local Stokes layer production  $P_{33p}^*$  at the negative peaks of  $\Delta k_x^* \phi_{uv}^*$  and  $\Delta k_x^* \phi_{\theta v}^*$ . (a) Same data of  $I_{uv}$  and  $I_{\theta v}$  as in figure 16(c), but versus  $P_{33p}^*$ ; to ease the inspection, the inset shows figure 16(c). The data points at  $\omega^+ = 0.022$  and  $0.110$  have black and grey outlines, respectively. (b) Illustrates obtaining of  $P_{33p}^*$  for Case B (figure 17r), by intersecting the negative peak of  $\Delta k_x^* \phi_{\theta v}^*$  with the  $P_{33}^*$  profile (on the left axis).

at  $\omega^+ = 0.022$ ,  $P_{33p}^*$  increases by almost 3 times from  $Pr = 0.71$  to  $7.5$ , whereas at  $\omega^+ = 0.110$ ,  $P_{33p}^*$  increases by 1.5 times. As a result,  $I_{\theta v}$  has a milder decay rate at  $\omega^+ = 0.110$  ( $\gamma = 0.11$ ) than at  $\omega^+ = 0.022$  ( $\gamma = 0.53$ ).

We have seen how the behaviour of the Stokes layer leads to  $I_{\theta v} < I_{uv}$  by examining the streamwise and frequency spectrograms. This connection is more difficult to find in the spanwise spectrograms  $k_z^* \phi_{uv}^*$  and  $k_z^* \phi_{\theta v}^*$  (figures 17i–l, u–x). The Stokes layer predominantly modifies the time scale  $T^*$ , hence the streamwise length-scale  $\lambda_x^*$ , of the near-wall turbulence. However,  $k_z^* \phi_{uv}^*$  and  $k_z^* \phi_{\theta v}^*$  are integrated over  $T^*$  and  $\lambda_x^*$ , and so the smaller-scale energy amplification is cancelled by the large-scale energy attenuation. Thus, even though the Stokes layer protrusion (production) increases from Case A to Case B, the distributions of  $k_z^* \phi_{uv}^*$  and  $k_z^* \phi_{\theta v}^*$  suggest that the near-wall turbulence is distorted to a lesser extent.

Our observations regarding the large-scale attenuation and small-scale amplification can be extended by applying scale-wise decomposition to  $\Delta_{uv}^*$  and  $\Delta_{\theta v}^*$ . For instance, we can write  $\Delta_{uv}^* = \Delta_{uv+}^* + \Delta_{uv-}^*$ , where

$$\Delta_{uv+}^* = \int_{\lambda_x^* > 350} \Delta \phi_{uv}^*(k_x^*, y^*) dk_x^* - y^* (Re_\tau^{-1} - Re_{\tau_0}^{-1}), \quad (3.9a)$$

$$\Delta_{uv-}^* = \int_{\lambda_x^* \leq 350} \Delta \phi_{uv}^*(k_x^*, y^*) dk_x^*. \quad (3.9b)$$

We set the threshold of  $\lambda_x^* = 350$  for partitioning because the spectrograms for all cases show  $\Delta k_x^* \phi_{uv}^* > 0$  for  $\lambda_x^* \gtrsim 350$ , and  $\Delta k_x^* \phi_{uv}^* < 0$  for  $\lambda_x^* \lesssim 350$  (see figures 17e, q). As noted earlier (figure 10a and 3.3a), we need to subtract the term  $y^* (Re_\tau^{-1} - Re_{\tau_0}^{-1})$  from  $\Delta \bar{uv}^*$  to obtain its net contribution  $\Delta_{uv}^*$ . Considering figure 17(e, q), this contribution appears in the large scales of  $\Delta k_x^* \phi_{uv}^*$  ( $\lambda_x^* > 350$ ), and therefore we subtract  $y^* (Re_\tau^{-1} - Re_{\tau_0}^{-1})$  from the large-scale integration (3.9a). The same reasoning is applied to the partitioning of  $\Delta_{\theta v}^*$ , and we calculate  $\Delta_{\theta v+}^*$  and  $\Delta_{\theta v-}^*$  in a manner that is identical to that expressed by (3.9a) and (3.9b).

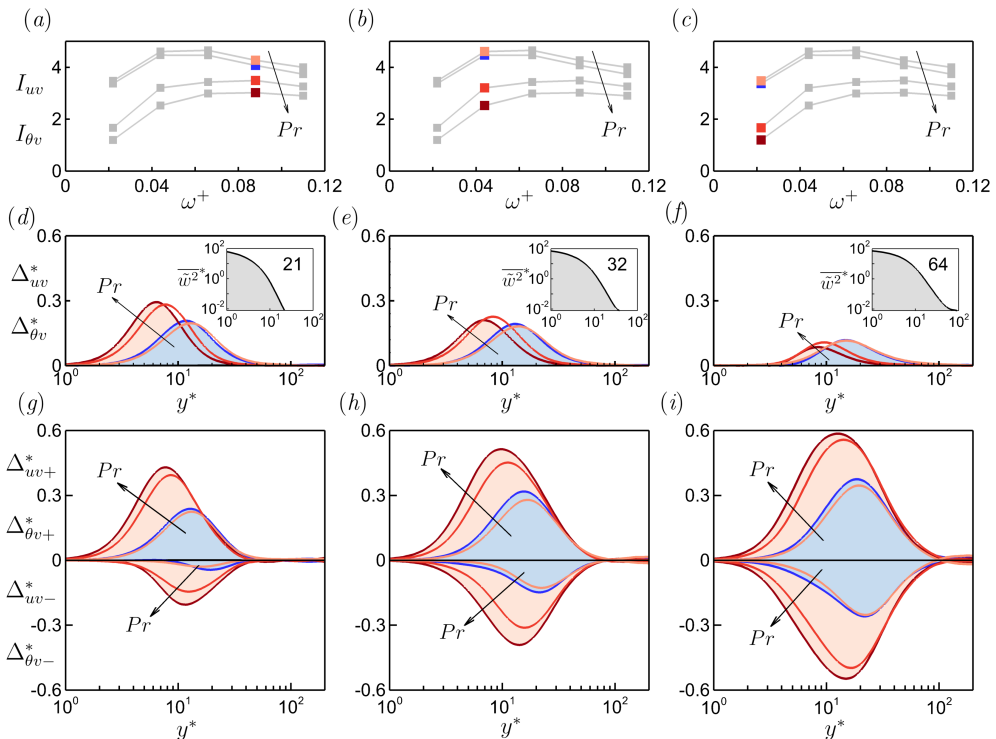


FIGURE 20. Large- and small-scale contributions to  $\Delta_{uv}^*$ ,  $\Delta_{\theta v}^*$  and their integrals  $I_{uv}$ ,  $I_{\theta v}$  for the travelling wave case. Left column  $\omega^+ = 0.088$ ; middle  $\omega^+ = 0.044$ ; right  $\omega^+ = 0.022$ . Blue  $uv$  profiles; for  $\theta v$  profiles light orange  $Pr = 0.71$ , orange 4.0, brick red 7.5. (a, b, c)  $I_{uv}$ ,  $I_{\theta v}$  versus  $\omega^+$ . (d, e, f)  $\Delta_{uv}^*$ ,  $\Delta_{\theta v}^*$  versus  $y^*$ ; the insets plot  $\bar{w}^{2*}$  representing the Stokes layer where the bold number reports  $\ell_{0.01}^*$ . (d, e, f) Total  $\Delta_{uv}^*$ ,  $\Delta_{\theta v}^*$ ; (g, h, i) decomposed  $\Delta_{uv\pm}^*$ ,  $\Delta_{\theta v\pm}^*$ . In (d–i), we shade under the profiles of  $\Delta_{uv}^*$  and  $\Delta_{\theta v}^*$  at  $Pr = 7.5$ , as well as their decomposition.

Figure 20 shows how changing  $\omega^+$  or  $Pr$  modifies the balance between the large-scale attenuation ( $\Delta_{uv+}^*$ ,  $\Delta_{\theta v+}^*$ ) and the small-scale amplification ( $\Delta_{uv-}^*$ ,  $\Delta_{\theta v-}^*$ ). The net attenuations  $\Delta_{uv}^*$  and  $\Delta_{\theta v}^*$  (figure 20d,e,f) depend on the disparity between their decomposed parts (figure 20g,h,i). Decreasing  $\omega^+$  (increasing the Stokes layer protrusion) simultaneously increase  $\Delta_{uv+}^*$ ,  $\Delta_{\theta v+}^*$  and  $\Delta_{uv-}^*$ ,  $\Delta_{\theta v-}^*$ . However, below the optimal  $\omega^+$ ,  $\Delta_{\theta v-}^*$ ,  $\Delta_{uv-}^*$  increase more than  $\Delta_{\theta v+}^*$ ,  $\Delta_{uv+}^*$ , leading to the drop in  $I_{uv}$ ,  $I_{\theta v}$ . We demonstrate this by shading the areas under  $\Delta_{\theta v}^*$  and its decompositions at  $Pr = 7.5$  light orange. From the optimal  $\omega^+ = 0.088$  (figure 20g) to 0.022 (figure 20i),  $\Delta_{\theta v-}^*$  increases more than  $\Delta_{\theta v+}^*$ , and  $I_{\theta v}$  decreases. At each  $\omega^+$ , increasing  $Pr$  increases  $\Delta_{\theta v-}^*$  more than  $\Delta_{\theta v+}^*$ , hence the drop in  $I_{\theta v}$ . This is due to the thinning of the conductive sublayer and the increase in the local Stokes layer production, as discussed with respect to figure 19.

### 3.8. Comparison between the travelling wave and the plane oscillation

All our findings based on the travelling wave motion (§3.3 to §3.7) remain broadly valid for the case of plane oscillation. By comparing figures 21 and 22 with figures 13 and 16, we see that, for example, the power-law relation  $I_{\theta v} = I_{uv}/Pr^\gamma$  fits well with the plane oscillation data (figure 21a), and the division  $HR > DR$  ( $\gamma < 0.5$ ) and  $HR < DR$

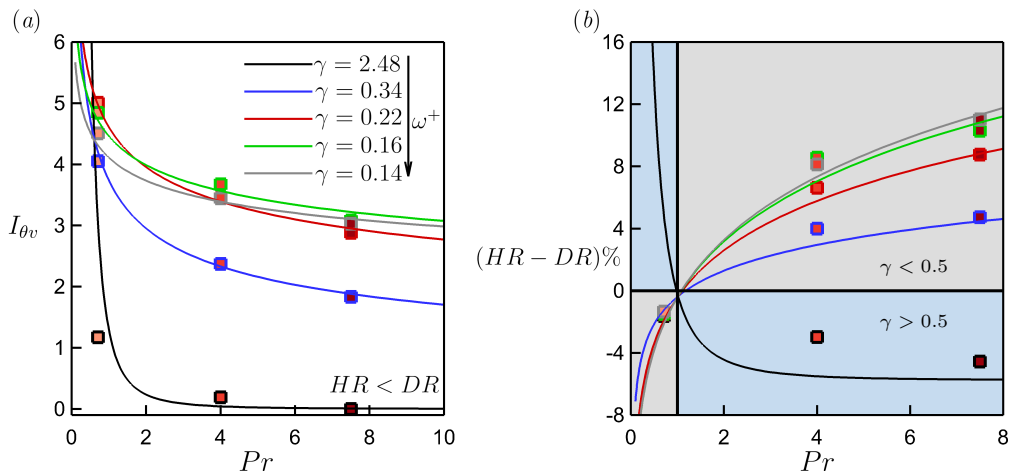


FIGURE 21. Similar plots as in figure 13(b,d), but for the plane oscillation with  $A^+ = 12$  (figure 3c). The outline colour of each data point indicates its  $\omega^+$ ;  $\omega^+ = 0.022$  (black), 0.044 (blue), 0.066 (red), 0.088 (green) and 0.110 (grey).

( $\gamma > 0.5$ ) is also valid (figure 21b). The value of  $\gamma$  at each  $\omega^+$  is close to its counterpart for the travelling wave case, with the exception of  $\omega^+ = 0.022$ , where  $\gamma = 2.48$  for the plane oscillation (black lines in figure 21), almost five times larger the the value of 0.53 found for the travelling wave motion. Such a strong decay rate drops  $I_{\theta v}$  to almost zero by  $Pr = 7.5$  for the plane oscillation, leading to  $HR - DR \simeq -5\%$ . This strong decay is associated with the appearance of a highly protrusive Stokes layer (figures 22a,c), in agreement with the discussion given in §3.7.

Figure 22 shows that for  $0.066 \leq \omega^+ \leq 0.110$ ,  $DR$ ,  $HR$ ,  $I_{uv}$ ,  $I_{\theta v}$ , and  $\ell_{0.01}^*$  for the plane oscillation are close to the values found for the travelling wave. However, as  $\omega^+$  decreases to 0.044 and then to 0.022, significant differences appear. For the plane oscillation, the Stokes layer becomes highly protrusive, reaching up to  $\ell_{0.01}^* \simeq 120$  at  $\omega^+ = 0.022$ . As discussed in §3.7, such a protrusive Stokes layer loses its efficacy in producing a net attenuation of the near-wall turbulence. As a result,  $I_{uv}$  and  $I_{\theta v}$  significantly drop, and  $\gamma$  rises significantly. Rouhi *et al.* (2023) showed that when  $\ell_{0.01}^* \sim \mathcal{O}(10^2)$ , the Stokes layer departs from its laminar-like structure, the mean velocity and temperature profiles become highly disturbed (figure 28j,k,l), and the predictive relations for  $DR$  (3.5a) and  $HR$  (3.5b) begin to fail. Similarly, we observe that at  $\omega^+ = 0.022$  the predictive relation for  $HR$  (3.5b) is much less accurate compared to its performance at higher frequencies (figure 21b).

As a final note, it appears that  $\gamma$ , a  $Pr$ -independent quantity, increases almost linearly with  $\ell_{0.01}^*$  and  $P_{33\max}^*$ , and decreases inversely with increasing  $\omega^+$  following

$$\gamma \simeq 4.2P_{33\max}^* \simeq 0.008\ell_{0.01}^* \simeq 1/(80\omega^+). \quad (3.10)$$

This is supported by the results shown in figure 23, where we compile all our data for the travelling wave and the plane oscillation cases (with the exception of the plane oscillation at  $\omega^+ = 0.022$  where the Stokes layer is particularly protrusive). Our present data are at a fixed  $A^+ = 12$  for a plane oscillation ( $\kappa_x^+ = 0$ ) and a travelling wave ( $\kappa_x^+ = 0.0014$ ). The relation for  $\gamma$  (3.10) is expected to also depend on  $A^+$  and  $\kappa_x^+$ . However, for the upstream travelling wave with  $\omega^+ \gtrsim 0.04$ , we anticipate  $\gamma$  to weakly depend on  $\kappa_x^+$ . Our conjecture is partly based on the validity of (3.10) for  $\kappa_x^+ = 0$  and  $\kappa_x^+ = 0.0014$  for  $\omega^+ \gtrsim 0.04$ . Furthermore,  $\gamma$  relates  $\Delta\bar{\Theta}_{170}^*$  to  $\Delta\bar{U}_{170}^*$ , which  $\Delta\bar{U}_{170}^*$  is seen to weakly depend on  $\kappa_x^+$

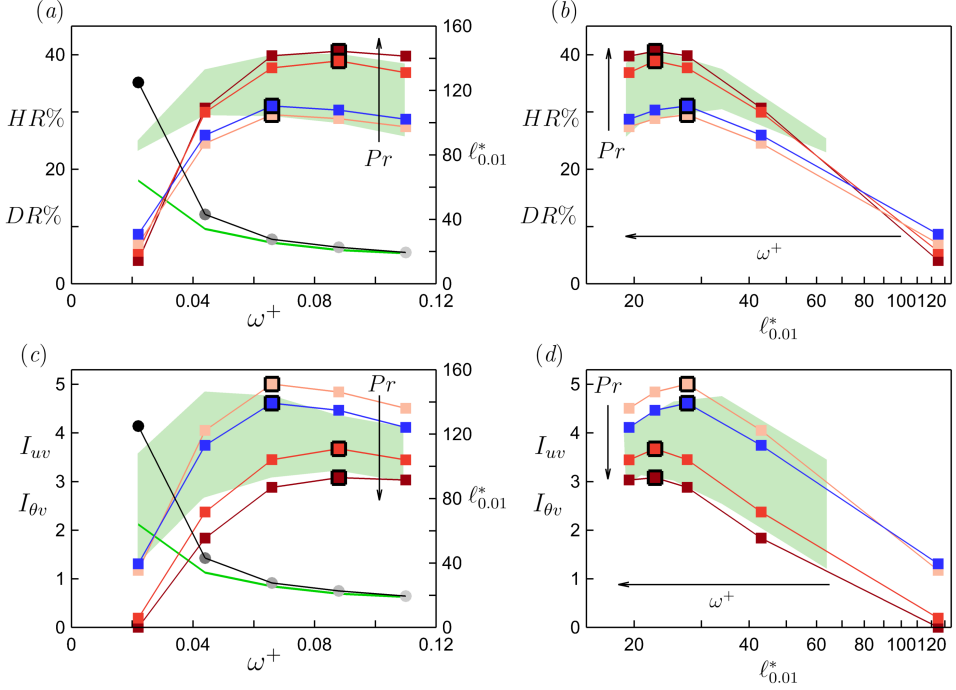


FIGURE 22. Same plots as in figure 16, except the data points (filled squares and circles) are from the plane oscillation with  $A^+ = 12$ . The range of variations in the travelling wave data points are shaded in green. In (a,c), the green lines plot  $\ell_{0.01}^*$  versus  $\omega^+$  for the travelling wave.

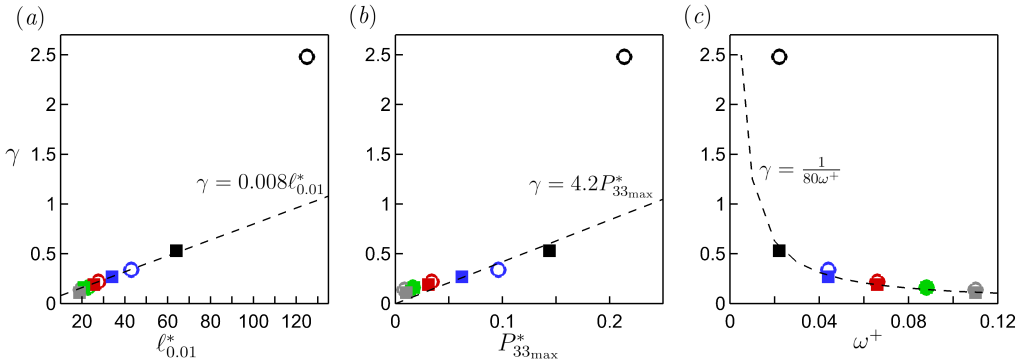


FIGURE 23. Assessment of the relations (3.10) between  $\gamma$ ,  $P_{33\max}^*$ ,  $\ell_{0.01}^*$  and  $\omega^+$  for the travelling wave (filled squares) and the plane oscillation (empty circles);  $\omega^+ = 0.022$  (black), 0.044 (blue), 0.066 (red), 0.088 (green) and 0.110 (grey).

for the upstream travelling wave with  $\omega^+ \gtrsim 0.04$  (figure 13 in Gatti & Quadrio 2016), and we anticipate  $\Delta\overline{\Theta}_{170}^*$  to behave similarly.

#### 4. Conclusions

Direct numerical simulations of turbulent half channel flow with forced convection were performed at a friction Reynolds number of 590 for Prandtl numbers of 0.71 (air), 4.0, 7.5 (water), and 20 (molten salt). Spanwise wall forcing was applied either as a plane

wall oscillation or a streamwise in-plane travelling wave with wavenumber  $\kappa_x^+ = 0.0014$  ( $\lambda^+ \simeq 4500$ ). For both oscillation mechanisms, we fix the amplitude  $A^+ = 12$  and change the frequency from  $\omega^+ = 0.022$  to 0.110 (upstream travelling waves only).

The key finding of the present work is that for  $\omega^+ > 0.022$  and  $Pr > 1$ , we achieve  $HR > DR$ ; especially, for  $\omega^+ \gtrsim 0.066$  and  $Pr \gtrsim 4.0$ , there is a significant disparity between  $HR \simeq 40\%$  and  $DR \simeq 30\%$ . On the other hand, for  $\omega^+ \leq 0.022$  and  $Pr > 1$ ,  $HR \lesssim DR$ . These results apply to the travelling wave motion and the plane oscillation. To help understand these results, we derived explicit relations between  $HR$  and  $DR$  and the integrals of the attenuation in the turbulent shear-stress ( $I_{uv}$ ) and turbulent temperature-flux ( $I_{\theta v}$ ). Figure 24 summarises how  $I_{uv}$  and  $I_{\theta v}$  change with  $Pr$  and  $\omega^+$ , and illustrates the underlying physics. For the cases considered here, we find that  $I_{\theta v} \simeq I_{uv}/Pr^\gamma$ , where  $\gamma \simeq 1/(80\omega^+) \simeq 4.2P_{33\max}^*$  is proportional to the Stokes layer production  $P_{33}^*$ . Therefore, we expect  $I_{\theta v}$  to fall below  $I_{uv}$  for  $Pr > 1$  and for increasing  $\gamma$  (decreasing  $\omega^+$  and increasing  $P_{33}^*$ ). Stokes layer production attenuates the energy of the streak-like scales with  $\lambda_x^+ \simeq 1000$  (hence the rise in  $I_{uv}, I_{\theta v}$ ), but generates small scales with  $\lambda_x^+ \simeq 100$  and amplifies their energy (hence the drop in  $I_{uv}, I_{\theta v}$ ). At a fixed  $\omega^+$  ( $\gamma$ ), increasing  $Pr$  towards  $Pr > 1$ , thins the conductive sublayer, and the energetic small scales of  $\theta v$  travel closer to the wall, and locally are exposed to a larger Stokes layer production compared to those of  $uv$ . Larger Stokes layer production means larger amplification of energy in the small scales of  $\theta v$  compared to  $uv$ , leading to  $I_{\theta v} < I_{uv}$  (figure 24d,f). In other words, for  $Pr > 1$ , the energy attenuation of  $\theta v$  is less than  $uv$ . Nevertheless, by exploiting  $I_{\theta v} \simeq I_{uv}/Pr^\gamma$ , we arrive at  $HR - DR \propto Pr^{(0.5-\gamma)} - 1$ , as  $HR$  depends on  $\Delta\bar{\Theta}^* = PrI_{\theta v} = Pr^{(1-\gamma)}I_{uv}$ , and the non-actuated Stanton number that decays with  $Pr$ . Therefore, we can achieve  $HR - DR > 0$  if  $\gamma \lesssim 0.5$  ( $\omega^+ \gtrsim 0.025$ ). These findings and the relations between  $HR - DR$ ,  $\omega^+$ ,  $\gamma$  and  $P_{33\max}^*$  agree well with our DNS data for both the travelling wave and the plane oscillation.

The time scale of the near-wall energetic temperature scales  $\mathcal{T}_\theta^+$  was found to be almost insensitive to  $Pr$ , and it remains close to its counterpart for the velocity scales  $\mathcal{T}_u^+ \simeq 100$ . As a result, for the plane oscillation, the optimal value of  $\omega^+$  for the maximum  $HR$  is close to the one for the maximum  $DR$ , that is,  $\omega^+ \simeq 2\pi/100 \simeq 0.066$ . However, for the travelling wave, the optimal frequency for  $HR$  changes from 0.044 at  $Pr = 0.71$  to 0.088 at  $Pr = 7.5$  because it depends on the advection speed of the energetic temperature scales. The thinning of the conductive sublayer decreases the advection speed, and so the optimal frequency of actuation increases.

From the Prandtl number scaling of the thermal statistics, we derived a predictive model for  $HR$ . By knowing  $\gamma$  and  $I_{uv}$  for a fixed set of actuation parameters ( $A^+, \kappa_x^+, \omega^+$ ) at a given Reynolds and Prandtl number, the model predicts  $HR$  at other Prandtl and Reynolds numbers. Using this model, we generated a map  $HR(Pr, Re_{\tau_0})$  for the optimal case with  $\omega^+ = 0.088$ , and found good agreement with the computations for Prandtl numbers up to 7.5. To further evaluate the model, we conducted an extra simulation at  $\omega^+ = 0.088$  and  $Pr = 20, Re_{\tau_0} = 590$ . Again, good agreement with the model was found (DNS  $HR = 43\%, HR - DR = 13\%$  compared with the model  $HR = 45\%, HR - DR = 14\%$ ).

As an early systematic work on turbulent heat-transfer control by spanwise wall forcing, we focused on  $Pr$  and  $\omega^+ > 0$ , due to their significant effect on  $HR$ , and  $HR - DR$ . Our findings are encouraging to pursue this work towards investigating the effects of  $A^+, \kappa_x^+, Re_{\tau_0}$  and  $\omega^+ < 0$  (downstream travelling wave). We anticipate that our discoveries could be applied to a wider parameter space. Our conjecture is partly supported by the validity of our findings for both the travelling wave and plane



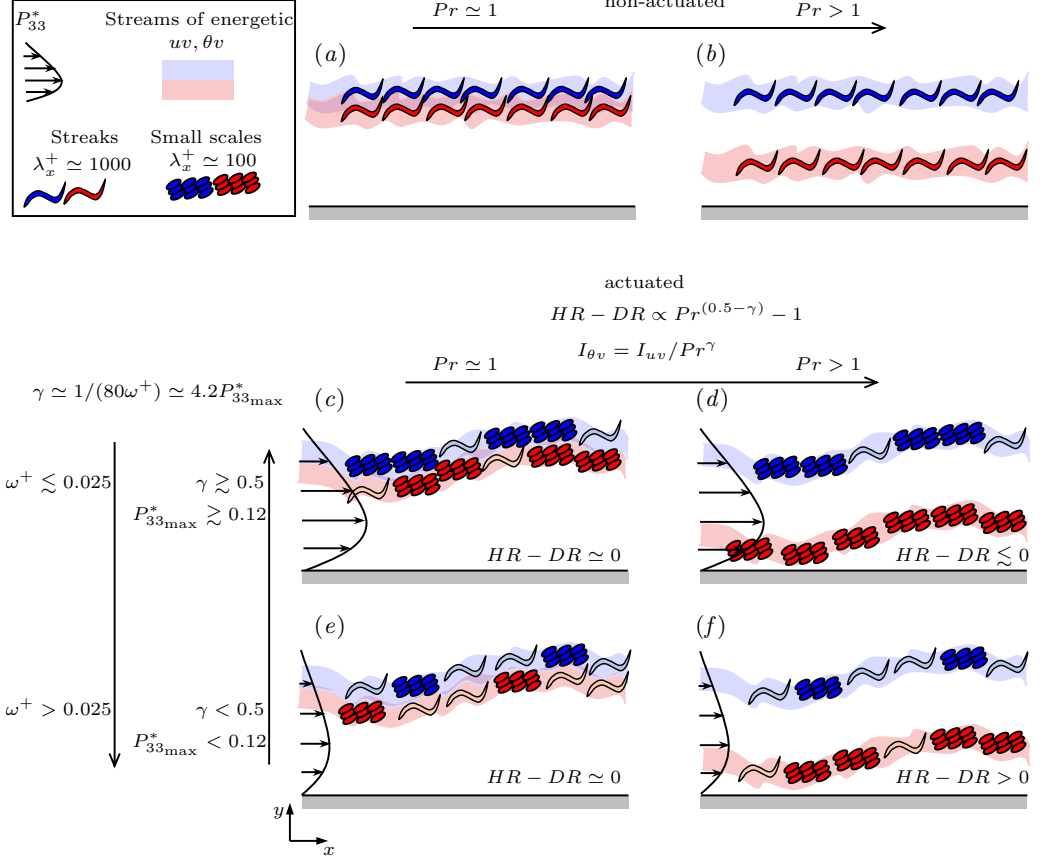


FIGURE 24. Schematic illustration of our findings from §3.4 to §3.8. The meaning of each sketch is written in the top-left framed area. (a–f) Near-wall illustration of the energetic scales of  $uv$  and  $\theta v$  for (a, b) non-actuated cases, and (c–f) actuated cases. (a, c, e) correspond to  $Pr \approx 1$ , and (b, d, f) correspond to  $Pr > 1$ . For the actuated cases, (c, d) represent  $\omega^+ \lesssim 0.025$ , and (e, f) represent  $\omega^+ > 0.025$ . The Stokes layer production profile is drawn for each actuated case.

oscillation in the present study. Also, similar findings for  $DR$  are shown to be applicable to a wide parameter space of  $(A^+, \omega^+, \kappa_x^+, Re_{\tau_0})$ . The prediction model for  $DR$  by Gatti & Quadrio (2016), the analogue of our model for  $HR$ , is shown to agree well with the DNS (Gatti et al. 2024) and LES (Rouhi et al. 2023) data for  $1000 \lesssim Re_{\tau_0} \lesssim 6000$  over the actuation parameter space where  $DR$  significantly changes ( $5 \leq A^+ \leq 12, 0 \leq \kappa_x^+ \leq 0.02, -0.2 \leq \omega^+ \leq 0.2$ ). Also, the findings related to the Stokes layer protrusion and  $DR$  are found to be valid over the range of  $\kappa_x^+$  considered so far. For instance, up to the Stokes layer thickness  $\delta_S^* \simeq 6$  (protrusion height  $\ell_{0.01}^* \simeq 25$ ), there is a linear relation between  $DR, \ell_{0.01}^*$  and  $\delta_S^*$ , regardless of the value of  $\kappa_x^+$  (Quadrio & Ricco 2011; Rouhi et al. 2023). This is because the modification of the velocity scales by the Stokes layer is similar between the plane oscillation (Touber & Leschziner 2012) and the travelling wave at different values of  $\kappa_x^+$  (Rouhi et al. 2023).

### Acknowledgements

The research was funded through the Deep Science Fund of Intellectual Ventures (IV). We acknowledge Dr. Daniel Chung for providing his DNS solver. We thank EPSRC

setup	$Re_{\tau_0}$	$Pr$	$L_x, L_z$	$\Delta_x^+, \Delta_z^+$	$\Delta_y^+$	$C_{f_0}$	$Nu_0$	Legend
full fine	590	7.5	$2\pi h, \pi h$	3.6, 1.8	0.12 – 3.8	0.0058	162	—
reduced coarse	590	7.5	$2.7h, 0.85h$	8.3, 3.9	0.28 – 8.5	0.0057	162	---
MKM99	590	-	$2\pi h, \pi h$	9.7, 4.8	0.09 – 7.2	0.0057	-	■
AH21	500	7.0	$2\pi h, \pi h$	8.2, 4.1	0.27 – 3.9	-	132	○

TABLE 2. Validation simulations for the reduced coarse setup. Non-actuated half channel flow at  $Pr = 7.5$ . Statistics for these cases are shown in figure 25. The reference cases are MKM99 (Moser *et al.* 1999) and AH21 (Alcántara-Ávila & Hoyas 2021).

for the computational time made available on ARCHER2 via the UK Turbulence Consortium (EP/R029326/1), and IV for providing additional computational time on ARCHER2.

**Declaration of interests.** The authors report no conflict of interest.

## Appendix A. Validation of the grid and the domain size

The production runs were performed in a reduced-domain half channel flow ( $L_x \gtrsim 2.7h, L_z \simeq 0.85h$ ) with grid resolution  $\Delta_x^+ \times \Delta_z^+ \simeq 8 \times 4$ ; we call this setup “reduced coarse”. To check that this setup gives accurate  $DR, HR$  and statistics of interest over our parameter space, calculations with a finer grid resolution of  $\Delta_x^+ \times \Delta_z^+ \simeq 4 \times 2$  were conducted in a full domain ( $L_x \gtrsim 2\pi h, L_z \simeq \pi h$ ); we call this setup “full fine”. Two additional setups are also used, called “full coarse” ( $L_x \gtrsim 7.6h, L_z \simeq \pi h, \Delta_x^+ \times \Delta_z^+ \simeq 8 \times 4$ ) and “full intermediate” ( $L_x \gtrsim 7.6h, L_z \simeq \pi h, \Delta_x^+ \times \Delta_z^+ \simeq 6 \times 3$ ). For all simulations,  $Re_{\tau_0} = 590$  and  $A^+ = 12$ . For all the reduced domain cases, we reconstruct the  $\bar{U}^*$  and  $\bar{\Theta}^*$  profiles beyond  $y_{res}^* = 170$ , and calculate  $DR$  and  $HR$  following our approach in §2.3.

For the non-actuated half channel flow at  $Pr = 7.5$ , table 2 shows that for the full fine and reduced coarse setups, the Nusselt numbers  $Nu_0$  are identical, and the skin-friction coefficients  $C_{f_0}$  differ by less than 2%. The profiles of  $\bar{U}^+, \bar{\Theta}^+$ , turbulent stresses  $\bar{u}^{2+}, \bar{v}^{2+}, \bar{w}^{2+}$ , and mean square of turbulent temperature  $\bar{\theta}^{2+}$  are also in excellent agreement (figure 25). Compared to the reference data, our obtained  $C_{f_0}$  from the reduced coarse case is identical to the one from Moser *et al.* (1999) (table 2); similarly, our velocity statistics up to  $y_{res}^+ \simeq 200$  are in excellent agreement (figure 25). In terms of the temperature statistics  $\bar{\Theta}^+, \bar{\theta}^{2+}$ , the small differences between our results and those from Alcántara-Ávila & Hoyas (2021) are most likely due to the differences in  $Re_{\tau_0}$  and  $Pr$  (590 compared to 500, and 7.5 compared to 7).

For the actuated half channel flow cases at  $Pr = 0.71$  and  $7.5$ , table 3 lists three sets of validation cases. For Set 1, we compare the “reduced coarse” setup with the “full coarse” setup because the grid resolution of  $\Delta_x^+ \times \Delta_z^+ \simeq 8 \times 4$  is fine enough at this  $Pr$  (Pirozzoli *et al.* 2016; Alcántara-Ávila *et al.* 2018, 2021; Alcántara-Ávila & Hoyas 2021). Sets 1 and 2 are travelling wave cases, and Set 3 is for the plane oscillation case. For each set, we see that reducing the domain size and coarsening the grid from the full fine setup to the reduced coarse setup changes  $DR$  and  $HR$  by a maximum of 1.5% and 1.9%, respectively.

Set 2 contains the most challenging cases over the range  $0.71 \leq Pr \leq 7.5$  in terms of their grid resolution requirement. In figure 26, we compare the mean velocity  $\bar{U}^*$  and the mean temperature  $\bar{\Theta}^*$  profiles for  $Pr = 7.5$ . In terms of the  $\bar{U}^*$  profiles, the reduced

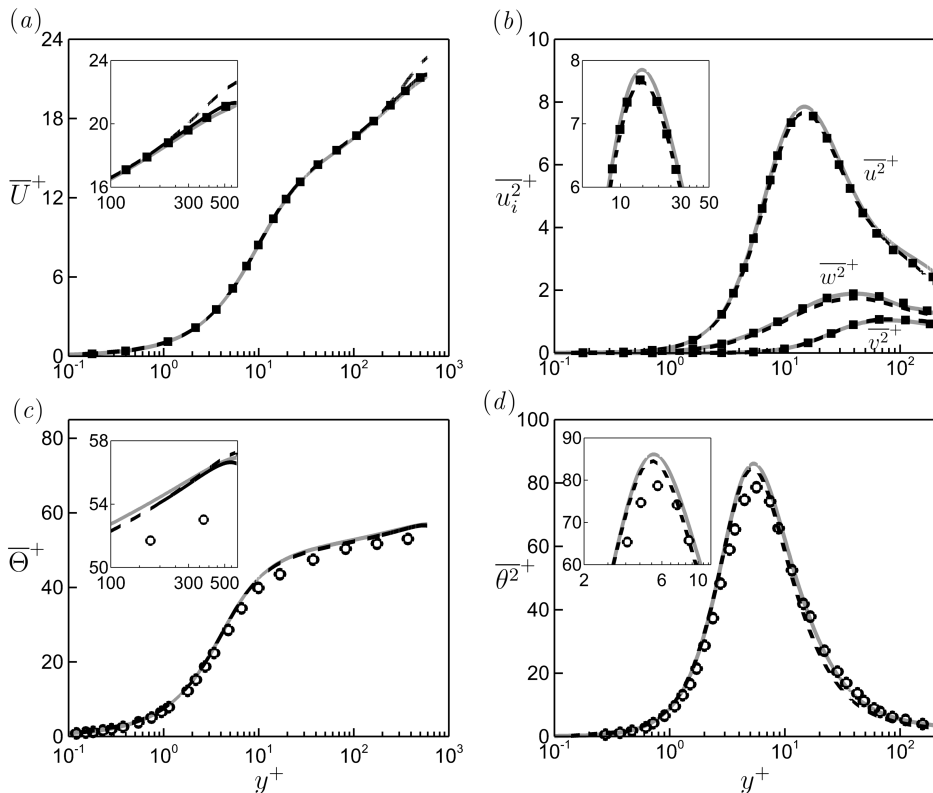


FIGURE 25. Comparing the results for the three setups given in table 2. (a) Mean velocity profiles  $\overline{U}^+$ . (b) Turbulent stresses  $\overline{u^2}^+$ ,  $\overline{v^2}^+$ ,  $\overline{w^2}^+$ . (c) Mean temperature profiles  $\overline{\Theta}^+$ . (d) Mean square of turbulent temperature  $\overline{\theta^2}^+$ . Solid grey line, “full fine” setup. Dashed line: “reduced coarse” setup. Solid black line in (a, c), reconstructed profile for  $y^+ \geq 200$  as in § 2.3. Square symbols: DNS of Moser *et al.* (1999). Circle symbols: DNS of Alcántara-Ávila & Hoyas (2021).

coarse setup is almost identical to the full fine setup up to  $y_{\text{res}}^* \simeq 170$ . Beyond  $y_{\text{res}}^*$ , the reconstructed  $\overline{U}^*$  profiles for the reduced coarse setup agree well with the full fine setup. In terms of the  $\overline{\Theta}^*$  profiles, excellent agreement is obtained between the full fine setup and the reduced coarse setup at  $\omega^+ = 0.022$  and  $0.088$  (figures 26a, c). At  $\omega^+ = 0.044$ , there is some sensitivity to the grid, where at  $y^* = 200$ ,  $\overline{\Theta}^* = 74.3$  for the full fine setup, and  $73.0$  for the reduced coarse setup. This difference (1.3 units) is small relative to the temperature difference  $\Delta\overline{\Theta}_{200}^* \simeq 19.0$  between the actuated and the non-actuated profiles. In figure 27, we assess the accuracy of the reduced coarse setup in resolving  $\overline{u^2}^*$  and  $\overline{\theta^2}^*$ , as well as their pre-multiplied spectrograms  $k_x^* \phi_{uu}^*$ ,  $k_z^* \phi_{uu}^*$ ,  $k_x^* \phi_{\theta\theta}^*$ ,  $k_z^* \phi_{\theta\theta}^*$  at  $\omega^+ = 0.044$ . The reduced coarse setup results agree well with the full fine setup results, especially in matching the energetic peaks in the spectrograms in terms of magnitude, location  $y^*$ , and length scales  $\lambda_x^*$ ,  $\lambda_z^*$ .

Table 4 summarises our validation study at  $Pr = 20.0$  (table 1). For the non-actuated case (table 4),  $C_{f_0}$  and  $C_{h_0}$  from the coarse grid results differ from the intermediate grid results by a maximum of 0.5%, and for the travelling wave case,  $DR$  and  $HR$  differ by < 1%.

Based on these results, we conclude that  $DR$ ,  $HR$  and the statistics of interest can be accurately computed using the reduced coarse setup with the grid resolution of  $\Delta_x^+ \times$

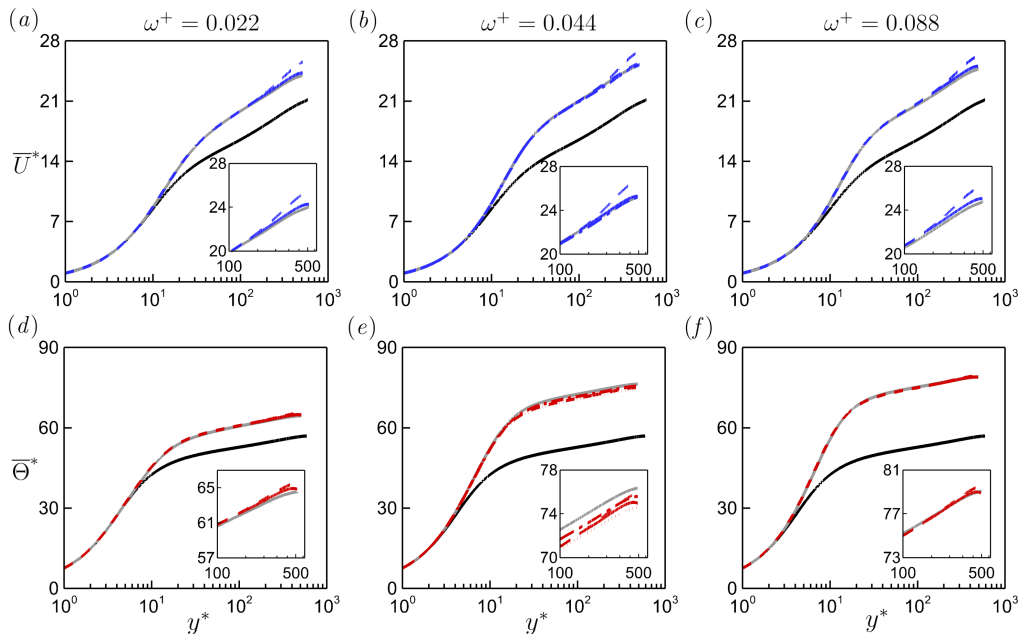


FIGURE 26. Comparison of the mean velocity (*a,b,c*) and the mean temperature (*d,e,f*) profiles for the travelling wave at  $Pr = 7.5$  (Set 2, table 3). (*a,d*)  $\omega^+ = 0.022$ , (*b,e*)  $\omega^+ = 0.044$  and (*c,f*)  $\omega^+ = 0.088$ . Solid grey line: “full fine” case. Dashed-dotted line: “full inter.” case. Dotted line: full coarse case. Dashed line: “reduc. coarse” case. Solid blue and red lines, reconstructed profiles for  $y^* \geq 170$  as in § 2.3. Solid black line: non-actuated “full fine” case.

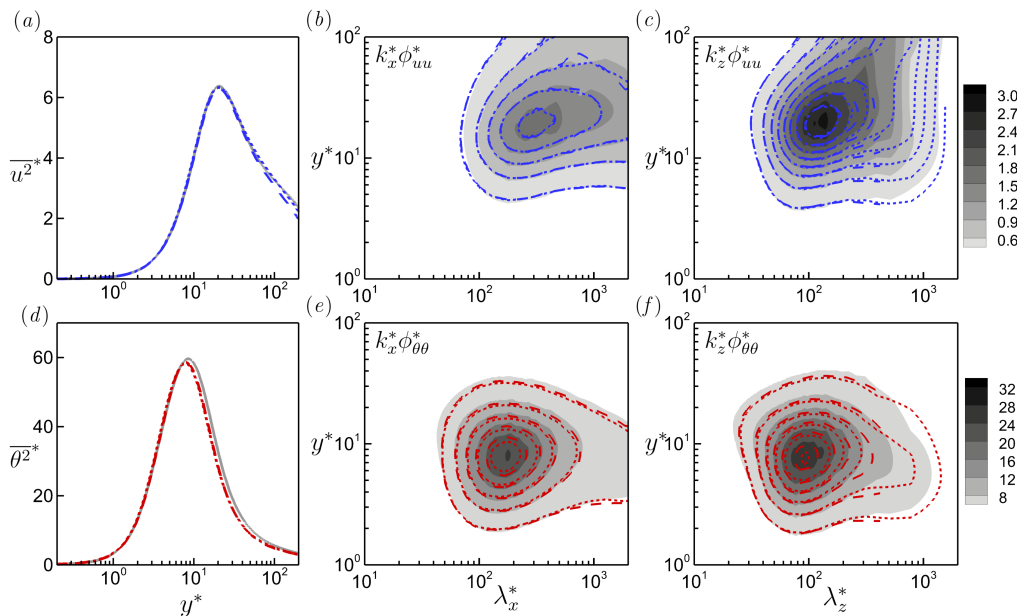


FIGURE 27. Comparison of (*a*) streamwise turbulent stress  $\overline{u^2^*}$  and (*d*) mean square of turbulent temperature  $\overline{\theta^2^*}$ , as well as their pre-multiplied spectrograms  $k_x^*\phi_{uu}^*$ ,  $k_z^*\phi_{uu}^*$ ,  $k_x^*\phi_{\theta\theta}^*$ ,  $k_z^*\phi_{\theta\theta}^*$  (*b,c,e,f*) for the travelling wave at  $Pr = 7.5$ ,  $\omega^+ = 0.044$  (Set 2, table 3). Solid grey line and grey-scale contour field: “full fine” case. Dotted line and dotted contour lines: “full coarse” case. Dashed line and dashed contour lines: “reduc. coarse” case.

case	$\omega^+$	$L_x, L_z$	$\Delta_x^+, \Delta_z^+$	$\Delta_y^+$	DR%	HR%		
full coarse	0.022	$7.6h, \pi h$	7.4, 3.9	0.20 – 6.0	24.5	23.3		Set 1 $Pr = 0.71$ $\kappa_x^+ = 0.0014$ $\epsilon_{DR_{\max}}, \epsilon_{HR_{\max}}$ 0.7%, 0.6%
reduc. coarse	0.022	$7.6h, 0.85h$	8.8, 3.9	0.28 – 8.5	25.2	23.6		
full coarse	0.044	$7.6h, \pi h$	7.4, 3.9	0.20 – 6.0	30.4	29.1		
reduc. coarse	0.044	$7.6h, 0.85h$	8.8, 3.9	0.28 – 8.5	30.6	29.3		
full coarse	0.088	$7.6h, \pi h$	7.4, 3.9	0.20 – 6.0	29.9	28.5		
reduc. coarse	0.088	$7.6h, 0.85h$	8.8, 3.9	0.28 – 8.5	29.3	27.9		
							Line	
full fine	0.022	$7.6h, \pi h$	3.9, 1.8	0.12 – 3.8	26.2	25.4	—	Set 2 $Pr = 7.5$ $\kappa_x^+ = 0.0014$
reduc. coarse	0.022	$7.6h, 0.85h$	8.8, 3.9	0.28 – 8.5	25.6	24.0	---	
full fine	0.044	$7.6h, \pi h$	3.9, 1.8	0.12 – 3.8	31.4	38.6	—	$\epsilon_{DR_{\max}}, \epsilon_{HR_{\max}}$ 1.5%, 1.6%
full inter.	0.044	$7.6h, \pi h$	5.8, 2.7	0.18 – 5.7	30.9	37.7	-·-	
full coarse	0.044	$7.6h, \pi h$	8.8, 4.0	0.28 – 8.5	31.0	37.0	·····	
reduc. coarse	0.044	$7.6h, 0.85h$	8.8, 3.9	0.28 – 8.5	31.8	37.7	---	
full fine	0.088	$7.6h, \pi h$	3.9, 1.8	0.12 – 3.8	29.0	39.8	—	
reduc. coarse	0.088	$7.6h, 0.85h$	8.8, 3.9	0.28 – 8.5	30.5	40.4	---	
full fine	0.044	$2\pi h, \pi h$	3.6, 1.8	0.12 – 3.8	25.2	28.9		Set 3 $Pr = 7.5$ $\kappa_x^+ = 0$
reduc. coarse	0.044	$2.7h, 0.85h$	8.3, 3.9	0.28 – 8.5	26.5	30.8		
full fine	0.088	$2\pi h, \pi h$	3.6, 1.8	0.12 – 3.8	29.4	39.0		$\epsilon_{DR_{\max}}, \epsilon_{HR_{\max}}$ 1.4%, 1.9%
reduc. coarse	0.088	$2.7h, 0.85h$	8.3, 3.9	0.28 – 8.5	30.8	40.7		

TABLE 3. Validation simulations for grid and domain size.

case	$\kappa_x^+$	$\omega^+$	$L_x, L_z$	$\Delta_x^+, \Delta_z^+$	$\Delta_y^+$	$C_{f_0}$	$C_{h_0}$	DR%	HR%
reduc. coarse	-	-	$2.7h, 0.85h$	8.3, 3.9	0.28 – 8.4	0.0057	$5.47 \times 10^{-4}$	-	-
reduc. inter.	-	-	$2.7h, 0.85h$	6.2, 2.6	0.18 – 5.6	0.0057	$5.44 \times 10^{-4}$	-	-
reduc. coarse	0.0014	0.088	$7.6h, 0.85h$	8.8, 3.9	0.28 – 8.4	-	-	29.5	43.5
reduc. inter.	0.0014	0.088	$7.6h, 0.85h$	5.8, 2.6	0.18 – 5.6	-	-	28.6	43.1

TABLE 4. Validation cases at  $Re_{\tau_0} = 590$  and  $Pr = 20.0$ .

$\Delta_z^+ \simeq 8 \times 4$ , and the domain size of  $L_x \times L_z \simeq 7.6h \times 0.85h$  for the travelling wave case ( $\kappa_x^+ = 0.0014$ ), and the domain size of  $L_x \times L_z \simeq 2.7h \times 0.85h$  for the plane oscillation case ( $\kappa_x^+ = 0$ ). These grid and domain size prescriptions were used for our production calculations (table 1).

## Appendix B. Relation between heat-transfer reduction and temperature difference

The mean velocity  $\bar{U}^*$  and temperature  $\bar{\Theta}^*$  profiles in the log region and beyond can be expressed based on the following semi-empirical wall-wake relations (Rouhi *et al.* 2022)

$$\bar{U}^* = \frac{1}{\kappa_u} \ln(y^*) + B_u + \frac{2\Pi_u}{\kappa_u} \mathcal{W}_u(y/h) + \Delta\bar{U}_{\log}^*, \quad (\text{C1a})$$

$$\bar{\Theta}^* = \frac{1}{\kappa_\theta} \ln(y^*) + B_\theta + \frac{2\Pi_\theta}{\kappa_\theta} \mathcal{W}_\theta(y/h) + \Delta\bar{\Theta}_{\log}^*, \quad (\text{C1b})$$

where  $\kappa_u, \kappa_\theta$  and  $B_u$  are constants, but the offset  $B_\theta$  depends on  $Pr$  (Kader & Yaglom 1972; Kader 1981). The wake profiles  $(2\Pi_u/\kappa_u)\mathcal{W}_u(y/h)$  and  $(2\Pi_\theta/\kappa_\theta)\mathcal{W}_\theta(y/h)$  depend on the flow configuration, e.g. channel, pipe or boundary layer (Pope 2000; Nagib & Chauhan 2008). The log-law shifts,  $\Delta\bar{U}_{\log}^*$  and  $\Delta\bar{\Theta}_{\log}^*$ , are non-zero for the actuated cases. These log-law shifts are evaluated at  $y^* = 170$ , where  $\Delta\bar{U}^*$  and  $\Delta\bar{\Theta}^*$  approximately reach their asymptotic values (figures 4 and 8). For fixed operating parameters ( $A^+, \kappa_x^+, \omega^+$ ),  $\Delta\bar{U}_{\log}^*$  is constant for the upstream travelling wave (Hurst *et al.* 2014; Gatti & Quadrio 2016; Rouhi *et al.* 2023). However,  $\Delta\bar{\Theta}_{\log}^*$  strongly depends on  $Pr$  (figures 8*k,l*). We set the constants  $\kappa_u = 0.4$ ,  $\kappa_\theta = 0.46$  and  $B_u = 5.2$  following Pirozzoli *et al.* (2016) and Rouhi *et al.* (2022), and obtain the offset  $B_\theta(Pr) = 12.5Pr^{2/3} + 2.12 \ln Pr - 5.3$  following Kader & Yaglom (1972), which is reported to be accurate for  $Pr \gtrsim 0.7$ . The suitability of these choices is confirmed in §2.3 and Appendix A.

The bulk velocity  $U_b^*$  and bulk temperature  $\Theta_b^*$  are found by integrating (C1a) and (C1b), so that

$$U_b^* = \frac{1}{\kappa_u} \ln(Re_\tau) - \frac{1}{\kappa_u} + B_u + \frac{2\Pi_u}{\kappa_u} \int_0^h \mathcal{W}_u(y/h) dy + \Delta\bar{U}_{\log}^*, \quad (\text{C2a})$$

$$\Theta_b^* = \frac{1}{\kappa_\theta} \ln(Re_\tau) - \frac{1}{\kappa_\theta} + B_\theta + \frac{2\Pi_\theta}{\kappa_\theta} \int_0^h \mathcal{W}_\theta(y/h) dy + \Delta\bar{\Theta}_{\log}^*. \quad (\text{C2b})$$

By subtracting the non-actuated  $U_{b_0}^*$  and  $\Theta_{b_0}^*$  from their actuated counterparts  $U_b^*$  and  $\Theta_b^*$ , and by assuming that the wake profiles are not influenced by the wall oscillation, we obtain

$$U_b^* - U_{b_0}^* = \frac{1}{\kappa_u} \ln \left( \frac{Re_\tau}{Re_{\tau_0}} \right) + \Delta\bar{U}_{\log}^*, \quad \Theta_b^* - \Theta_{b_0}^* = \frac{1}{\kappa_\theta} \ln \left( \frac{Re_\tau}{Re_{\tau_0}} \right) + \Delta\bar{\Theta}_{\log}^*. \quad (\text{C3a,b})$$

When  $Re_\tau$  is matched between the actuated and the non-actuated cases ( $Re_\tau = Re_{\tau_0}$ ), the first term on the right-hand-side of (C3a,b) disappears. However, when the bulk Reynolds number  $Re_b$  is matched, as in our work, this term is retained because  $Re_\tau \neq Re_{\tau_0}$ . By using (C3a,b) and the relations  $C_f = 2/U_b^{*2}$ ,  $C_h = 1/(U_b^* \Theta_b^*)$ ,  $C_f/C_{f_0} = R_f = 1 - DR$ , and  $C_h/C_{h_0} = R_h = 1 - HR$ , we can relate  $\Delta\bar{U}_{\log}^*$  and  $\Delta\bar{\Theta}_{\log}^*$  to  $R_f$  and  $R_h$  according to

$$\Delta\bar{U}_{\log}^* = \sqrt{\frac{2}{C_{f_0}}} \left[ \frac{1}{\sqrt{R_f}} - 1 \right] - \frac{1}{2\kappa_u} \ln R_f, \quad (\text{C4a})$$

$$\Delta\bar{\Theta}_{\log}^* = \frac{\sqrt{C_{f_0}/2}}{C_{h_0}} \left[ \frac{\sqrt{R_f}}{R_h} - 1 \right] - \frac{1}{2\kappa_\theta} \ln R_f. \quad (\text{C4b})$$

Equation (C4a) was first derived by Gatti & Quadrio (2016) (their equation 4.7). Equation (C4b) is new.

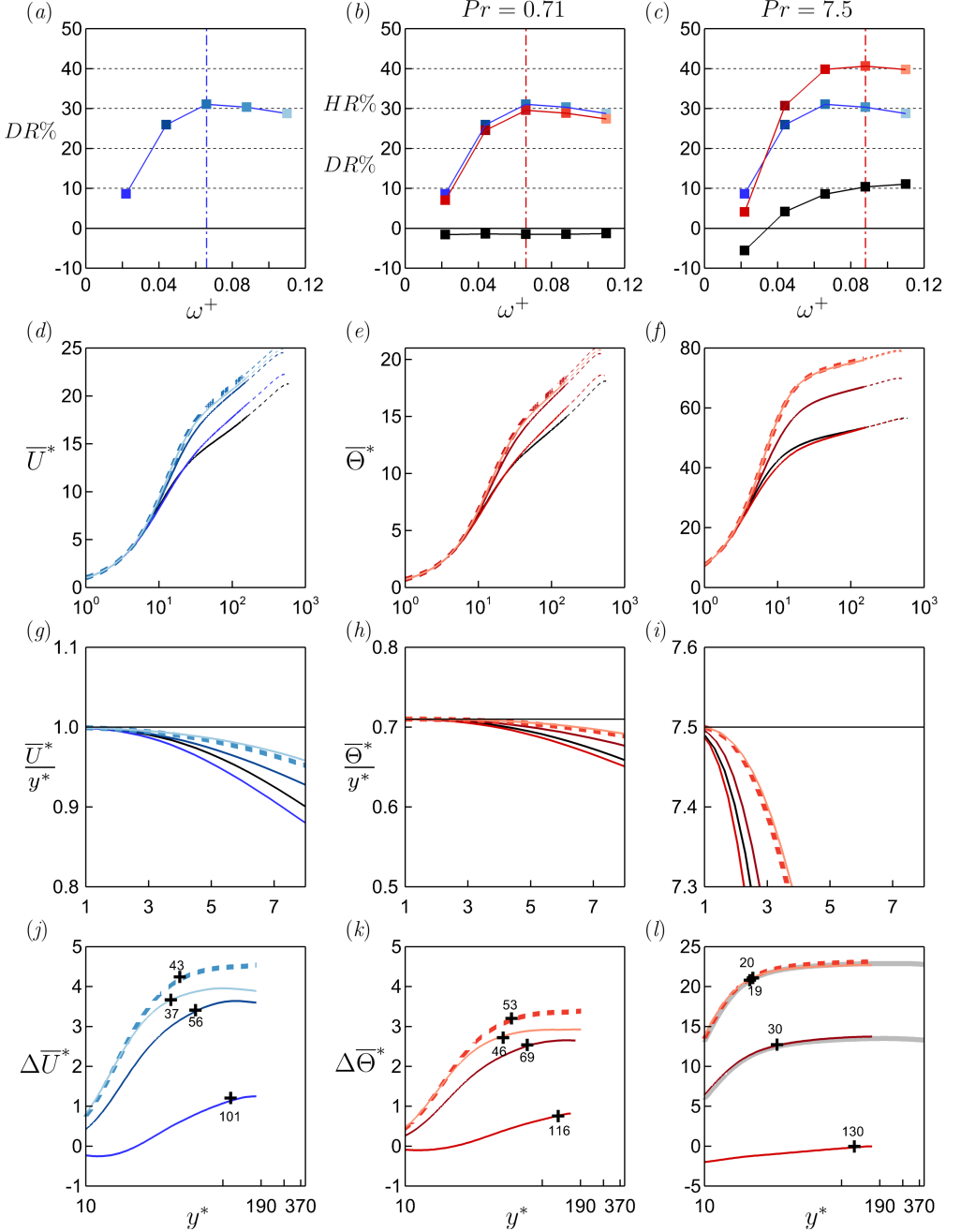


FIGURE 28. Same plots as in figure 8, but for the plane oscillation case with  $A^+ = 12$ .

## Appendix C. Statistics for the plane oscillation

See figures 28 and 29.

## REFERENCES

ALCÁNTARA-ÁVILA, F. & HOYAS, S. 2021 Direct numerical simulation of thermal channel flow

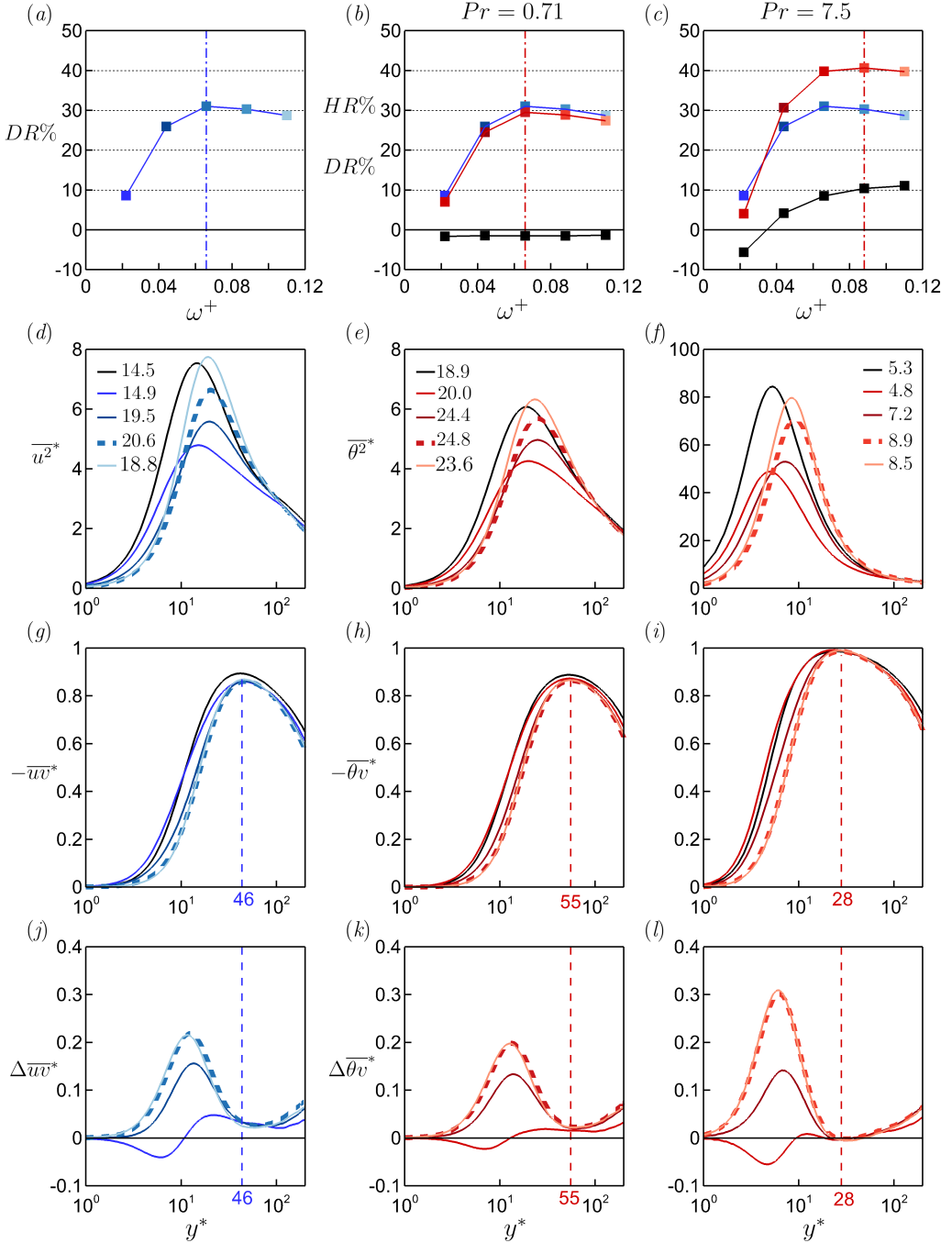


FIGURE 29. Same plots as in figure 9, but for the plane oscillation case with  $A^+ = 12$ .

for medium–high Prandtl numbers up to  $Re_\tau = 2000$ . *Int. J. Heat Mass Transf.* **176**, 121412.

ALCÁNTARA-ÁVILA, F., HOYAS, S. & PÉREZ-QUILES, M. J. 2018 DNS of thermal channel flow up to  $Re_\tau = 2000$  for medium to low Prandtl numbers. *Int. J. Heat Mass Transf.* **127**, 349–361.



- ALCÁNTARA-ÁVILA, F., HOYAS, S. & PÉREZ-QUILES, M. J. 2021 Direct numerical simulation of thermal channel flow for  $Re_\tau = 5000$  and  $Pr = 0.71$ . *J. Fluid Mech.* **916**, A29.
- BAEK, S., RYU, J., BANG, M. & HWANG, W. 2022 Flow non-uniformity and secondary flow characteristics within a serpentine cooling channel of a realistic gas turbine blade. *J. Turbomach.* **144**, 091002.
- BARON, A. & QUADRIO, M. 1995 Turbulent drag reduction by spanwise wall oscillations. *Appl. Sci. Res.* **55**, 311–326.
- BEWLEY, T. R., MOIN, P. & TEMAM, R. 2001 DNS-based predictive control of turbulence: an optimal benchmark for feedback algorithms. *J. Fluid Mech.* **447**, 179–225.
- BUNKER, R. S. 2013 Gas turbine cooling: moving from macro to micro cooling. In *ASME Turbo Expo*, p. V03CT14A002.
- CHANDRAN, D., ZAMPIRON, A., ROUHI, A., FU, M. K., WINE, D., HOLLOWAY, B., SMITS, A. J. & M., I. 2023 Turbulent drag reduction by spanwise wall forcing. Part 2: High-Reynolds-number experiments. *J. Fluid Mech.* **968**, A7.
- CHILTON, T. H. & COLBURN, A. P. 1934 Mass transfer (absorption) coefficients prediction from data on heat transfer and fluid friction. *Ind. Eng. Chem.* **26**, 1183–1187.
- CHOI, J. I., XU, C. X. & SUNG, H. J. 2002 Drag reduction by spanwise wall oscillation in wall-bounded turbulent flows. *AIAA J.* **40**, 842–850.
- CHOI, K. S. 2002 Near-wall structure of turbulent boundary layer with spanwise-wall oscillation. *Phys. Fluids* **14**, 2530–2542.
- CHOI, K. S. & CLAYTON, B. R. 2001 The mechanism of turbulent drag reduction with wall oscillation. *Int. J. Heat Fluid Flow* **22**, 1–9.
- CHOI, K. S., DEBISSCHOP, J. R. & CLAYTON, B. R. 1998 Turbulent boundary-layer control by means of spanwise-wall oscillation. *AIAA J.* **36**, 1157–1163.
- CHOI, K. S. & ORCHARD, D. M. 1997 Turbulence management using riblets for heat and momentum transfer. *Exp. Therm Fluid Sci.* **15**, 109–124.
- CHUNG, D., CHAN, L., MACDONALD, M., HUTCHINS, N. & OOI, A. 2015 A fast direct numerical simulation method for characterising hydraulic roughness. *J. Fluid Mech.* **773**, 418–431.
- COLBURN, A. P. 1964 A method of correlating forced convection heat-transfer data and a comparison with fluid friction. *Int. J. Heat Mass Transf.* **7**, 1359–1384.
- DEAN, R. B. 1978 Reynolds number dependence of skin friction and other bulk flow variables in two-dimensional rectangular duct flow. *J. Fluids Eng.* **100**, 215–223.
- DEL ÁLAMO, J. C. & JIMÉNEZ, J. 2009 Estimation of turbulent convection velocities and corrections to Taylor’s approximation. *J. Fluid Mech.* **640**, 5–26.
- DESHPANDE, R., CHANDRAN, D., SMITS, A. J. & MARUSIC, I. 2023 On the relationship between manipulated inter-scale phase and energy-efficient turbulent drag reduction. *J. Fluid Mech.* **972**, A12.
- DI CICCA, G. M., IUSO, G., SPAZZINI, P. G. & ONORATO, M. 2002 Particle image velocimetry investigation of a turbulent boundary layer manipulated by spanwise wall oscillations. *J. Fluid Mech.* **467**, 41–56.
- DIPPREY, D. F. & SABERSKY, R. H. 1963 Heat and momentum transfer in smooth and rough tubes at various Prandtl numbers. *Int. J. Heat Mass Transf.* **6**, 329–353.
- ENDRIKAT, S., MODESTI, D., MACDONALD, M., GARCÍA-MAYORAL, R., HUTCHINS, N. & CHUNG, D. 2021 Direct numerical simulations of turbulent flow over various riblet shapes in minimal-span channels. *Flow Turbul. Combust.* **107**, 1–29.
- FAN, J. F., DING, W. K., ZHANG, J. F., HE, Y. L. & TAO, W. Q. 2009 A performance evaluation plot of enhanced heat transfer techniques oriented for energy-saving. *Int. J. Heat Mass Transfer* **52**, 33–44.
- FANG, J., LU, L. & SHAO, L. 2009 Large eddy simulation of compressible turbulent channel flow with spanwise wall oscillation. *Sci. China Ser. E: Phys., Mech. Astron.* **52**, 1233–1243.
- FANG, J., LU, L. P. & SHAO, L. 2010 Heat transport mechanisms of low Mach number turbulent channel flow with spanwise wall oscillation. *Acta Mech. Sin.* **26**, 391–399.
- FOROOGHI, P., WEIDENLENER, A., MAGAGNATO, F., BÖHM, B., KUBACH, H., KOCH, T. & FROHNAPFEL, B. 2018 DNS of momentum and heat transfer over rough surfaces based on realistic combustion chamber deposit geometries. *Int. J. Heat Fluid Flow* **69**, 83–94.
- GATTI, D. & QUADRIO, M. 2013 Performance losses of drag-reducing spanwise forcing at moderate values of the Reynolds number. *Phys. Fluids* **25**, 125109.

- GATTI, D. & QUADRIO, M. 2016 Reynolds-number dependence of turbulent skin-friction drag reduction induced by spanwise forcing. *J. Fluid Mech.* **802**, 553–582.
- GATTI, D., QUADRIO, M., CHIARINI, A., GATTERE, F. & PIROZZOLI, S. 2024 Turbulent skin-friction drag reduction via spanwise forcing at high Reynolds number. *arXiv preprint arXiv:2409.07230* .
- GUÉRIN, L., FLAGEUL, C., CORDIER, L., GRIEU, S. & AGOSTINI, L. 2024 Preferential enhancement of convective heat transfer over drag via near-wall turbulence manipulation using spanwise wall oscillations. *Int. J. Heat Fluid Flow* **110**, 109564.
- HAN, D., YU, B., WANG, Y., ZHAO, Y. & YU, G. 2015 Fast thermal simulation of a heated crude oil pipeline with a BFC-Based POD reduced-order model. *Appl. Therm. Eng.* **88**, 217–229.
- HASEGAWA, H., ISHITANI, H., MATSUHASHI, R. & YOSHIOKA, M. 1998 Analysis on waste-heat transportation systems with different heat-energy carriers. *Appl. energy* **61**, 1–12.
- HASEGAWA, Y. & KASAGI, N. 2011 Dissimilar control of momentum and heat transfer in a fully developed turbulent channel flow. *J. Fluid Mech.* **683**, 57–93.
- HEALZER, J. M., MOFFAT, R. J. & KAYS, W. M. 1974 The turbulent boundary layer on a porous, rough plate: experimental heat transfer with uniform blowing. In *Proc. Thermophys. Heat Transf. Conf.*, p. 680.
- HETSRONI, G., TISELJ, I., BERGANT, R., MOSYAK, A. & POGREBNIYAK, E 2004 Convection velocity of temperature fluctuations in a turbulent flume. *ASME J. Heat Transfer* **126**, 843–848.
- HUANG, Z., LI, Z. Y., YU, G. L. & TAO, W. Q. 2017 Numerical investigations on fully-developed mixed turbulent convection in dimpled parabolic trough receiver tubes. *Appl. Therm. Eng.* **114**, 1287–1299.
- HURST, E., YANG, Q. & CHUNG, Y. M. 2014 The effect of Reynolds number on turbulent drag reduction by streamwise travelling waves. *J. Fluid Mech* **759**, 11.
- IWAMOTO, K., FUKAGATA, K., KASAGI, N. & SUZUKI, Y. 2005 Friction drag reduction achievable by near-wall turbulence manipulation at high Reynolds numbers. *Phys. Fluids* **17**, 011702–011702.
- JIN, Y. & HERWIG, H. 2014 Turbulent flow and heat transfer in channels with shark skin surfaces: entropy generation and its physical significance. *Int. J. Heat Mass Transf.* **70**, 10–22.
- JUNG, W. J., MANGIAVACCHI, N. & AKHAVAN, R. 1992 Suppression of turbulence in wall-bounded flows by high-frequency spanwise oscillations. *Phys. Fluids* **4**, 1605–1607.
- KADER, B. A. 1981 Temperature and concentration profiles in fully turbulent boundary layers. *Int. J. Heat Mass Transf.* **24**, 1541–1544.
- KADER, B. A. & YAGLOM, A. M. 1972 Heat and mass transfer laws for fully turbulent wall flows. *Int. J. Heat Mass Transf.* **15**, 2329–2351.
- KAKAÇ, S., SHAH, R. K. & AUNG, W. 1987 *Handbook of single-phase convective heat transfer*. Wiley, New York.
- KANG, H. C. & KIM, M. H. 1999 Effect of strip location on the air-side pressure drop and heat transfer in strip fin-and-tube heat exchanger. *Int. J. Refrig.* **22**, 302–312.
- KARNIADAKIS, G. E. & CHOI, K. S. 2003 Mechanisms on transverse motions in turbulent wall flows. *Annu. Rev. Fluid Mech.* **35**, 45–62.
- KASAGI, N., TOMITA, Y. & KURODA, A. 1992 Direct numerical simulation of passive scalar field in a turbulent channel flow. *J. Heat Transfer* **114**, 598–606.
- KAYS, W.M., CRAWFORD, M.E. & WEIGAND, B. 1993 *Convective Heat and Mass Transfer*. McGraw-Hill.
- KIM, J. & HUSSAIN, F. 1993 Propagation velocity of perturbations in turbulent channel flow. *Phys. Fluids* **5**, 695–706.
- KUWATA, Y. 2021 Direct numerical simulation of turbulent heat transfer on the Reynolds analogy over irregular rough surfaces. *Int. J. Heat Fluid Flow* **92**, 108859.
- KUWATA, Y. 2022 Dissimilar turbulent heat transfer enhancement by Kelvin–Helmholtz rollers over high-aspect-ratio longitudinal ribs. *J. Fluid Mech.* **952**, A21.
- LEE, C., KIM, J. & CHOI, H. 1998 Suboptimal control of turbulent channel flow for drag reduction. *J. Fluid Mech.* **358**, 245–258.

- LI, W. & LI, G. 2010 Modeling cooling tower fouling in helical-rib tubes based on von Kármán analogy. *Int. J. Heat Mass Transf.* **53**, 2715–2721.
- LIU, C. & GAYME, D. F. 2020 An input–output based analysis of convective velocity in turbulent channels. *J. Fluid Mech.* **888**, A32.
- MA, Q., LUO, L., WANG, R. Z. & SAUCE, G. 2009 A review on transportation of heat energy over long distance: Exploratory development. *Renewable Sustainable Energy Rev.* **13**, 1532–1540.
- MACDONALD, M., CHUNG, D., HUTCHINS, N., CHAN, L., OOI, A. & GARCÍA-MAYORAL, R. 2017 The minimal-span channel for rough-wall turbulent flows. *J. Fluid Mech.* **816**, 5–42.
- MACDONALD, M., HUTCHINS, N. & CHUNG, D. 2019 Roughness effects in turbulent forced convection. *J. Fluid Mech.* **861**, 138–162.
- MACDONALD, M., OOI, A., GARCÍA-MAYORAL, R., HUTCHINS, N. & CHUNG, D. 2018 Direct numerical simulation of high aspect ratio spanwise-aligned bars. *J. Fluid Mech.* **843**, 126–155.
- MARUSIC, I., CHANDRAN, D., ROUHI, A., FU, M. K., WINE, D., HOLLOWAY, B., CHUNG, D. & SMITS, A. J. 2021 An energy-efficient pathway to turbulent drag reduction. *Nat. Commun.* **12**, 1–8.
- MOSER, R. D., KIM, J. & MANSOUR, N. N. 1999 Direct numerical simulation of turbulent channel flow up to  $Re_\tau = 590$ . *Phys. Fluids* **11**, 943–945.
- NAGIB, H. M. & CHAUHAN, K. A. 2008 Variations of von Kármán coefficient in canonical flows. *Phys. Fluids* **20**, 101518.
- NG, C. S., OOI, A., LOHSE, D. & CHUNG, D. 2015 Vertical natural convection: application of the unifying theory of thermal convection. *J. Fluid Mech.* **764**, 349–361.
- OTTO, M., KAPAT, J., RICKLICK, M. & MHETRAS, S. 2022 Heat transfer in a rib turbulated pin fin array for trailing edge cooling. *J. Therm. Sci. Eng. Appl.* **14**.
- PIROZZOLI, S. 2023 Prandtl number effects on passive scalars in turbulent pipe flow. *J. Fluid Mech.* **965**, A7.
- PIROZZOLI, S., BERNARDINI, M. & ORLANDI, P. 2016 Passive scalars in turbulent channel flow at high Reynolds number. *J. Fluid Mech.* **788**, 614–639.
- PIROZZOLI, S., ROMERO, J., FATICA, M., VERZICCO, R. & ORLANDI, P. 2022 DNS of passive scalars in turbulent pipe flow. *J. Fluid Mech.* **940**, A45.
- POPE, S.B. 2000 *Turbulent Flows*. Cambridge University Press.
- QUADRIO, M. 2011 Drag reduction in turbulent boundary layers by in-plane wall motion. *Phil. Trans. R. Soc. A* **369**, 1428–1442.
- QUADRIO, M. & RICCO, P. 2011 The laminar generalized Stokes layer and turbulent drag reduction. *J. Fluid Mech.* **667**, 135–157.
- QUADRIO, M., RICCO, P. & VIOTTI, C. 2009 Streamwise-travelling waves of spanwise wall velocity for turbulent drag reduction. *J. Fluid Mech.* **627**, 161–178.
- QUADRIO, M. & SIBILLA, S. 2000 Numerical simulation of turbulent flow in a pipe oscillating around its axis. *J. Fluid Mech.* **424**, 217–241.
- RANI, P. & TRIPATHY, P. P. 2022 Experimental investigation on heat transfer performance of solar collector with baffles and semicircular loops fins under varied air mass flow rates. *Int. J. Therm. Sci.* **178**, 107597.
- RICCO, P. 2004 Modification of near-wall turbulence due to spanwise wall oscillations. *J. Turbul.* **5**, 024.
- RICCO, P., OTTONELLI, C., HASEGAWA, Y. & QUADRIO, M. 2012 Changes in turbulent dissipation in a channel flow with oscillating walls. *J. Fluid Mech.* **700**, 77–104.
- RICCO, P., SKOTE, M. & LESCHZINER, M. A. 2021 A review of turbulent skin-friction drag reduction by near-wall transverse forcing. *Prog. Aerosp. Sci.* **123**, 100713.
- RICCO, P. & WU, S. 2004 On the effects of lateral wall oscillations on a turbulent boundary layer. *Exp. Therm Fluid Sci.* **29**, 41–52.
- ROUHI, A., CHUNG, D. & HUTCHINS, N. 2019 Direct numerical simulation of open-channel flow over smooth-to-rough and rough-to-smooth step changes. *J. Fluid Mech.* **866**, 450–486.
- ROUHI, A., ENDRIKAT, S., MODESTI, D., SANDBERG, R. D., ODA, T., TANIMOTO, K., HUTCHINS, N. & CHUNG, D. 2022 Riblet-generated flow mechanisms that lead to local breaking of Reynolds analogy. *J. Fluid Mech.* **951**, A45.
- ROUHI, A., FU, M. K., CHANDRAN, D., ZAMPIRON, A., SMITS, A. J. & MARUSIC, I. 2023

- Turbulent drag reduction by spanwise wall forcing. Part 1: Large-eddy simulations. *J. Fluid Mech.* **968**, A6.
- ROUHI, A., LOHSE, D., MARUSIC, I., SUN, C. & CHUNG, D. 2021 Coriolis effect on centrifugal buoyancy-driven convection in a thin cylindrical shell. *J. Fluid Mech.* **910**, A32.
- ROWIN, W. A., ZHONG, K., SAURAV, T., JELLY, T., HUTCHINS, N. & CHUNG, D. 2024 Modelling the effect of roughness density on turbulent forced convection. *J. Fluid Mech.* **979**, A22.
- SCHLÜNDER, E. U. 1998 Analogy between heat and momentum transfer. *Chem. Eng. Process. Process Intensif.* **37**, 103–107.
- SCHWERTFIRM, F. & MANHART, M. 2007 DNS of passive scalar transport in turbulent channel flow at high Schmidt numbers. *Int. J. Heat Fluid Flow* **28**, 1204–1214.
- SHAW, D. A. & HANRATTY, T. J. 1977 Turbulent mass transfer rates to a wall for large Schmidt numbers. *AIChE J.* **23**, 28–37.
- STALIO, E. & NOBILE, E. 2003 Direct numerical simulation of heat transfer over riblets. *Int. J. Heat Fluid Flow* **24**, 356–371.
- TOUBER, E. & LESCHZNER, M. A. 2012 Near-wall streak modification by spanwise oscillatory wall motion and drag-reduction mechanisms. *J. Fluid Mech.* **693**, 150–200.
- UMAIR, M., TARDU, S. & DOCHE, O. 2022 Reynolds stresses transport in a turbulent channel flow subjected to streamwise traveling waves. *Phys. Rev. Fluids* **7**, 054601.
- VENGADESAN, E. & SENTHIL, R. 2020 A review on recent developments in thermal performance enhancement methods of flat plate solar air collector. *Renewable Sustainable Energy Rev.* **134**, 110315.
- VIOTTI, C., QUADRIO, M. & LUCHINI, P. 2009 Streamwise oscillation of spanwise velocity at the wall of a channel for turbulent drag reduction. *Phys. Fluids* **21**, 115109.
- WALSH, M. J. & WEINSTEIN, L. M. 1979 Drag and heat-transfer characteristics of small longitudinally ribbed surfaces. *AIAA J.* **17**, 770–771.
- WATANABE, K. & TAKAHASHI, T. 2002 LES simulation and experimental measurement of fully developed ribbed channel flow and heat transfer. In *ASME Turbo Expo*, , vol. 36088, pp. 411–417.
- XIE, X. & JIANG, Y. 2017 Absorption heat exchangers for long-distance heat transportation. *Energy* **141**, 2242–2250.
- YAMAMOTO, A., HASEGAWA, Y. & KASAGI, N. 2013 Optimal control of dissimilar heat and momentum transfer in a fully developed turbulent channel flow. *J. Fluid Mech.* **733**, 189–220.
- YAO, J., CHEN, X. & HUSSAIN, F. 2022 Direct numerical simulation of turbulent open channel flows at moderately high Reynolds numbers. *J. Fluid Mech.* **953**, A19.
- YU, B., LI, C., ZHANG, Z., LIU, X., ZHANG, J., WEI, J., SUN, S. & HUANG, J. 2010 Numerical simulation of a buried hot crude oil pipeline under normal operation. *Appl. Therm. Eng.* **30**, 2670–2679.
- YUAN, J. & PIOMELLI, U. 2014 Estimation and prediction of the roughness function on realistic surfaces. *J. Turbul.* **15**, 350–365.
- YUAN, Q., LUO, Y., SHI, T., GAO, Y., WEI, J., YU, B. & CHEN, Y. 2023 Investigation into the heat transfer models for the hot crude oil transportation in a long-buried pipeline. *Energy Sci. Eng.* **11**, 2169–2184.
- ZHONG, K., HUTCHINS, N. & CHUNG, D. 2023 Heat-transfer scaling at moderate Prandtl numbers in the fully rough regime. *J. Fluid Mech.* **959**, A8.